

2020

Insulator To Metal Transition Dynamics Of Vanadium Dioxide Thin Films

Scott Madaras

William & Mary - Arts & Sciences, scottmadaras@gmail.com

Follow this and additional works at: <https://scholarworks.wm.edu/etd>



Part of the [Condensed Matter Physics Commons](#)

Recommended Citation

Madaras, Scott, "Insulator To Metal Transition Dynamics Of Vanadium Dioxide Thin Films" (2020).
Dissertations, Theses, and Masters Projects. Paper 1616444322.
<http://dx.doi.org/10.21220/s2-0gby-x326>

This Dissertation is brought to you for free and open access by the Theses, Dissertations, & Master Projects at W&M ScholarWorks. It has been accepted for inclusion in Dissertations, Theses, and Masters Projects by an authorized administrator of W&M ScholarWorks. For more information, please contact scholarworks@wm.edu.

Insulator to Metal Transition Dynamics of Vanadium Dioxide Thin Films

Scott Eric Madaras

Yorktown, Virginia

Master of Science, William & Mary, 2016

Bachelor of Science, University of Denver, 2011

A Dissertation presented to the Graduate Faculty of The College of William &
Mary in Candidacy for the Degree of
Doctor of Philosophy

Department of Physics

College of William & Mary
August 2020

APPROVAL PAGE

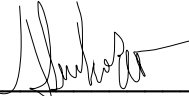
This Dissertation is submitted in partial fulfillment of
the requirements for the degree of

Doctor of Philosophy



Scott E. Madaras

Approved by the Committee June 2020



Co-Chair

Rosa Alejandra Lukaszew, Professor Emerita, Physics
NSF Program Director/College of William & Mary



Co-Chair

Irina Novikova, Professor, Physics
College of William & Mary



Dennis Manos, CSX Professor, Physics and Applied Science
College of William & Mary



Enrico Rossi, Associate Professor, Physics
College of William & Mary



Dr. Gwyn Williams, Deputy Division Head, Retired, Free Electron Laser Div.
Thomas Jefferson National Accelerator Facility

ABSTRACT

Vanadium Dioxide (VO_2) is a strongly correlated material which has been studied for many decades. VO_2 has been proposed for uses in technologies such as optical modulators, IR modulators, optical switches and Mott memory devices. These technologies are taking advantage of VO_2 's insulator to metal transition (IMT) and the corresponding changes to the optical and material properties. The insulator to metal transition in VO_2 can be accessed by thermal heating, applied electric field, or ultra-fast photo induced processes. Recently, thin films of VO_2 grown on Titanium Dioxide doped with Niobium ($\text{TiO}_2\text{:Nb}$), have shown promise as a possible UV photo detector with high quantum efficiency which utilizes a heterostructure between these two materials. In this work, the dynamics of the IMT on thin films of VO_2 is explored. We show that surface plasmons generated in an Au thin film can induce the insulator to metal transition in a thin film of VO_2 due to the enhanced electric field as well as help detect the IMT via changes in its resonance condition. Time resolved pump probe studies were also done on thin films of VO_2 grown on TiO_2 and $\text{TiO}_2\text{:Nb}$, using UV photon energy of 3.1 eV (400nm wavelength). The fluence threshold of the IMT at 3.1 eV was significantly lower than published values for the 1.55 eV pump fluence. The time response of the IMT shows uncommon reflectivity dynamics in these samples. The response was partially attributed to internal interference of the reflected probe beam from the inhomogeneous layers formed inside the film by different phases of VO_2 , and can be elucidated by a diffusion model with respect to its optical properties. Finally, the photocurrent generation time constants for the sample with highest quantum efficiency are given and compared to its ultrafast photo induced IMT time constants.

TABLE OF CONTENTS

Acknowledgements	v
Dedications	vi
List of Tables	vii
List of Figures	viii
CHAPTER 1. Introduction	1
1.1 Vanadium Dioxide and Its Insulator to Metal Transition.	1
1.2 Motivation, Goals and Objectives	3
1.3 Outline	5
CHAPTER 2: Theories and Background for VO ₂	7
2.1 Conductivity in Solids	7
2.2 Strongly Correlated Material	9
2.3 VO ₂ Crystal Structure	13
2.4 Energy Band Structure in VO ₂	15
2.5. VO ₂ Optical Properties	17
2.6 Insulator to Metallic Transition Theories	18
2.6.1 Thermally Induced IMT in VO ₂	18
2.6.2 Electric Field Induced IMT	20
2.6.3 The Ultra-Fast Photo Induced IMT	22
2.6.3.1 Pump probe physics	22

2.6.3.2 Ultra-Fast IMT models for VO ₂	24
CHAPTER 3: Experimental Arrangements	30
3.1 Surface Plasmon Resonance System	30
3.1.1 Surface plasmon polaritons	30
3.1.2 SPP Field Enhancement	34
3.1.3 Experimental SPR Set Up	35
3.2 Ultrafast Laser System / Pump-Probe System	39
3.2.1 Ultrafast Laser System	39
3.2.2 Nonlinear Generation of 3.1 eV Light	44
3.2.3 Pump Probe Experimental Set-up	45
3.2.4 Pump Probe Signal Analysis	47
3.3 Photocurrent Speed Measurement	51
3.4 Ellipsometry	51
CHAPTER 4: Samples and Sample Characterization	53
4.1 Characterization Methods	53
4.2 Samples for Pump Probe Ultrafast and Photocurrent Tests	54
4.2.1 Sample manufacturing background	55
4.2.2 Crystal characterization	55
4.2.3 Surface Morphology Characterization	56
4.2.4 Ellipsometry on the VO ₂ on TiO ₂	56

4.2.5	Thermal IMT of the VO ₂ on TiO ₂ sample	60
4.3	Au-VO ₂ sample for SPR experiments	61
4.3.1	SPR Sample Design and Manufacture	61
4.3.2	SPR Sample Characterization	62
CHAPTER 5: Insulator to Metal Transition Induced by Surface Plasmon Polariton in VO ₂ /Au Thin Films		64
5.1	Introduction	64
5.2	Surface Plasmon Resonance IMT Studies in VO ₂	65
5.2.1	SPR Modelling Response	65
5.2.2	SPR VO ₂ IMT Results	67
5.2.3	E-Field Model Comparison with Data	73
5.3	Hunt for Hysteretical Response in VO ₂	77
5.4	Conclusion	82
CHAPTER 6: Ultrafast Photo induced IMT in VO ₂		84
6.1	Introduction	84
6.2	Photo Induced IMT in VO ₂ on TiO ₂ or TiO ₂ :Nb	85
6.3	Optical Response Diffusion Model	87
6.4	The Effects of Nb Doping of the TiO ₂ Substrate on the Photoinduced VO ₂ IMT Dynamics	93
6.5	Photo Induced IMT in VO ₂ TiO ₂ :Nb for Different VO ₂ Layer Thickness	98
6.5.1	15nm Thick Sample	98

6.5.2	22nm Sample	101
6.5.3	50nm Sample	102
6.5.4	Time Constants	105
6.6	Effects of the Pump Photon Energy on the IMT of VO ₂ on TiO ₂ :Nb	109
6.7	Conclusion	112
CHAPTER 7 VO ₂ TiO ₂ :Nb Photocurrent Generation Dynamics		114
7.1	Measurement of Photocurrent Switching Speed with Blue Light	115
CHAPTER 8 Conclusion and Outlook		123
8.1	Conclusion	123
8.2	Outlook	124
Appendix A Ellipsometry		126
Appendix B Computational methods		129
B.1	Finite difference time domain (FDTD)	124
B.2.	4×4 optical matrix method	131
Bibliography		137

ACKNOWLEDGEMENTS

I would like to thank my advisors Ale Lukaszew and Irina Novikova for their guidance and support over the years making this work possible. I have had the pleasure of working with an amazing research group of people, both past and present. Thank you Doug Beringer, Matt Burton, Jason Creeden, Savannah Cuzzo, Mike Klopf, Zhaozhu Li, Eugeny Mikhailov, Nikunj Kumar Prajapati, and Lei Wang. You have all helped me immensely. Much thanks to Aiden Harbick for doing the thermal IMT measurements. I would also like to thank David Lahneman and Mumtaz Qazilbash for their help and knowledge on the ellipsometry of the VO_2 samples. I need to thank Joseph Zalameda along with Buzz Wincheski at NASA LaRC for loaning the FLIR system and help with Raman measurements that made some of this work possible. Also thanks to Salinporn Kittiwatanakul and Jiwei Lu for making the VO_2/Au samples. I would be remiss if I did not thank Jlab's old FEL division because those scientists showed me the ropes to some very exciting physics that got me started on this path.

To my friends both in and out of physics, thanks for the friendship and support over the years.

Finally I would like to thank my family. Your love and unwavering support for my endeavors over the years is something I will always cherish. I will never be able to pay it back in full.

This research was made possible by financial support from the Defense Threat Reduction Agency (DTRA) (HDTRA 1-16-1-0056). NASA LaRC loan agreement O160035

For my family.

LIST OF TABLES

4.1	Optical properties of VO ₂ on TiO ₂	59
6.1	15nm Sample Time Constants	108
6.2	22nm Sample Time Constants	108
6.3	30nm Sample Time Constants	109
6.4	50nm Sample Time Constants	109

LIST OF FIGURES

- 2.1. The band structure of various materials types. The vertical axis is the energy of the band. The dotted line is the fermi level. As you go from left to right you will see the band valence and conduction band separate. The black color represents electron fill level in the material. Greyed levels represent the case where electrons are partially occupying levels according to Fermi Statistics. 10
- 2.2. Shows simple graphic of a 1D periodic potential. The top line is a 1D periodic potential with equal spacing with the introduction of a perturbation of δ . This creates a distorted 1D periodic potential with a period of $2a$, with alternating potential positions dimerization offset by δ . 12
- 2.3. Insulating lattice structure of VO_2 with the dotted line shows the unit cell, and the red lines represent the dimers that form from the V ions. Red spheres indicate the V atoms and blue spheres indicate the oxygen atom. 14
- 2.4. Metallic crystal structure of VO_2 . The solid line represents the unit cell of the VO_2 in metallic state. The dotted line represents the cell for the insulator state. 15
- 2.5. Band representation of the insulating case of VO_2 and the orbitals being used to form the bands. 16
- 2.6. Representation of the metallic case of VO_2 with orbitals used to form the bands. 16
- 2.7. (a) Real and (b) imaginary component of VO_2 refractive index as a function of the photon energy. Measurements are for a 30nm thick VO_2 film on c-plane sapphire. 17
- 2.8. The normalized reflectance of a 30nm thick sample on TiO_2 when illuminated with 700nm light as the sample is thermal transitioned. The sample had a T_c of approximately 50 ± 5 °C and shows a hysteresis between heating and cooling of the sample. 19

- 2.9 A graphic of two types of photon excitation processes in semiconductors: interband direct absorption seen in (a) and interband indirect absorption seen in (b). 23
- 2.10 Shows the potential that the V atom that make up the V dimerization in VO₂ experience under the photo induced IMT. The x axis and coordinate are generalized to the displacement that describes the V dimer in VO₂. With the x=1.05 being full dimerization (insulating case) x=-0.36 represents no dimerization. The curve is the potential that takes into account the occupation of electrons in the bands, n_{||} in the valence band and n_π in the conduction band. The dashed grey line is the total electronic and potential energy of the system that covers both insulating and metallic case for the generalized coordinates. The solid black line is the potential for the case for the insulating state. The solid blue line is the case for just after photo excitation has happened (meaning number of electrons, n_π, are in the Π band). The dash blue line is 40fs after excitation and the dashed red line is 80fs after the start. Finally, the solid red line is the final state which is metallic. The black dots represent the V atom position at each of those time locations. Figure reproduced from [75]with permission from Phys. Rev. B. 26
- 2.11 Left panel is the density of states of the d_{||} band progressing through time in the vertical direction with the splitting being shown through the density of states (dashed-gray lines), the electron occupation is the red lines and the electron density is the blue lines. Right panel is density of states of the Π band seen with the same line colors. As the system is photo induced the changes in the band structure show the progression of the n_π electron density shifting and collapsing into the n_{||} electron density into a signal band. Reproduced from [75] with permission from Phys. Rev. B. 27
- 3.1 Shows the SPP at the interface of a metal to dielectric surface. The SPP is propagating in the x direction and the generated E field is in the z direction. The H_y field is pointing out of the page. The orientation of the wavevector are shown to the right. 31
- 3.2 Shows the SPP at a metal to dielectric surface interface. This is an example of the Kretschmann method for generating SPP. The

angle θ_0 is angle where the light k_x wavevector component equals the plasmon k_x wavevector. In our experimental apparatus, the metal is gold and dielectric is VO ₂ .	33
3.3. SPR simulated response of the reflectance of p polarized light at 1064nm on 31nm Au with 5nm of VO ₂ .	34
3.4. Diagram of the experimental setup. The lock-in-amplifier is set up to perform a differential measurement from the sample signal and the pick off.	36
3.5. Diagram of the experimental setup used for variable intensity measurements.	38
3.6. A simple example of pulse chirp amplification with seed pulse and stretcher and compress stages along with the gain media. The seed pulse goes into the stretcher. Increasing the pulse duration will lower the peak power of the pulse which is represented as the lower amplitude rainbow gaussian. This lower peak power pulse will interact with the gain media to increase the amplitude and has low enough starting amplitude to not damage the amplifier's gain media. After amplification the stretched light pulse goes into the compressor stage which decreases the pulse width while the peak power will be increased. Reproduced from [85].	42
3.7. Simple graphic of the pump probe experimental set up.	46
3.8. Simple graphic of the timing sequence of the pump probe measurement system, where the time delay of the probe pulse is generated by a variable spatial delay line. The inset shows the $\Delta R/R$ data that was generated in a typical VO ₂ thin film sample.	48
3.9. Vertical beam radius and location measurements from knife edge. Black line is the radius of the beam at the sample location and red is the beam center location of the probe.	49
4.1. Shows a simple Bragg reflection off a periodic lattice represented by the blue circles with a lattice spacing of d and the source beam at an incident angle θ . The path difference between the	

incident and reflected rays off adjacent lattice planes will be $2d \sin \theta$. Reproduced from [39].	54
4.2. XRD of the 30nm VO ₂ on TiO ₂ from [78] showing the presence of VO ₂ and TiO ₂ and their respective crystal orientations.	55
4.3. XRD of the 30nm VO ₂ on TiO ₂ :Nb from [79] showing the presence of VO ₂ and TiO ₂ and their respective crystal orientations.	56
4.4. AFM scans of the two-sample used for this experiment. Left are 30nm VO ₂ on TiO ₂ with 18.8nm RMS roughness. Right is 30nm VO ₂ on TiO ₂ :Nb with 15.5nm RMS roughness. Top images are 3D and bottom are 2D. From [79,94].	57
4.5. Dielectric function ϵ of 30nm VO ₂ on TiO ₂ . Graph (a) is the real component of ϵ and graph (b) is the imaginary component of ϵ . The blue line represents the insulating state and the red line represents the metallic state. The dashed blue lines are the components of the Tauc-Lorentz oscillators that make up the real and imaginary component of ϵ in the insulating state.	58
4.6. Characterization of the thermally induced IMT of the VO ₂ on TiO ₂ film using the reflectivity of (a) 400nm and (b) 700nm incoherent light. The red dots indicate the measurements taken while heating the sample, while the blue dots correspond to the cooling.	61
4.7. AFM image done at UVA for 5nm of VO ₂ over 31nm Au. The RMS roughness was 2.4nm.	63
4.8. XRD of the 5nm of VO ₂ over 31nm Au done by UVA the Au and VO ₂ peaks are labeled on a 2-theta axis.	63
5.1. (a) The reflection of the P polarized light (R _{pp}) from two different simulations methods; the (dotted) FDTD method the (solid) 4×4 optical matrix method. The blue lines are for the case when the VO ₂ is in the insulating state and the red lines are for case of metallic VO ₂ . (b) close-up view of the nadir region of the SPR curve showing the nadir shift produced by the SPP-induced IMT in the VO ₂ .	66

- 5.2. SPR data for two power levels. The vertical axis is normalized R_{pp} . The horizontal axis is the incident angle in degrees. The blue curve is for 10 μ W power level scan. The red curve is for a 5.4mW scan. The dashed box highlights the region where the IMT differences are detectable between the two power levels. 68
- 5.3. The SPR response curve of two different laser power scans on the sample. The blue diamonds show the data points for the 90 μ W power scan with uncertainty. The red squares show the data points for the 5.5mW power scan with uncertainty. The dashed blue line is the corresponding weighted polynomial for the 90 μ W scan. The dashed red line is the corresponding weighted polynomial for the 5.5mW scan. The dotted vertical blue and red lines are visual guides for the respective nadir locations for the polynomial fit. 69
- 5.4 Shows the SPR nadir locations versus the laser light power level. The dashed lines represent the simulation values for 100% insulating VO₂, 50% metallic/50% insulating VO₂, and 100% metallic VO₂. The red line is a visual guide for the transition behavior. The insert displays the SPR nadir locations for the bare 31nm-thick film of Au. For small scans in the vicinity of the resonant points, the data was fitted with a polynomial function. The weighted polynomial was a 3rd order polynomial and the minimum of the polynomial determined the nadir location for that power level scan. The uncertainty in amplitude of the fit at the nadir location was used to determine the uncertainty in the angular location. 71
- 5.5. FLIR image of the back of the sample with the SPR being a its nadir location for the metallic case of VO₂ the color gradient bar on the right is the temperature in °C. Panel (a) is the laser power on (12.4mW) and the red circle shows the approximate location of the beam on the sample. Panel (b) is the case where there is no laser power incident on the sample. Panel (c) is the difference between the two panels (a)-(b) measurement and again the red circle is the approximate location where the energy was deposited. 73
- 5.6. FDTD simulations for $|H_y|^2$ field in the sample for the case of Insulating VO₂ state (blue line) and metallic VO₂ (red line).

- $|H_y|^2$ is the density of the relative electromagnetic energy in the sample and shows the field enhancement caused by surface plasmons at the resonant point. 74
- 5.7. FDTD simulations for E field amplitude in the sample for the case of Insulating VO₂ state (blue line) and metallic VO₂ (red line) at the nadir location. The green line is the field amplitude at the angle location the where the deviation from Fig 4 starts at the power full IMT power threshold. 76
- 5.8. (a) A simulation of a triangle wave that represents the normalized reflectance versus time. By putting the laser signal through the optical modular, the amplitude of the laser light can be varied over a power range that crosses VO₂'s IMT threshold. At the power level where the IMT is initiated, a jump in the reflectance (a loss in R) should occur. If there is hysteresis, the reflectance jump with a rising laser power will not follow the reflectance jump with a falling laser power, which would show separate paths in the rising power vs. falling power. (b) An implementation of the concept using a laser's output that is modulated with an OAM to control the power level between 1.8mW to 6.4mW of laser light power, which is crossing the IMT threshold. The black line is the raw signal from the SPR monitor that comes from the balanced photodiode which is monitoring changes in the SPR reflectance output from the sample. The red line represents the laser's output. 79
- 5.9. Hysteresis study. Red lines are the measurements made at the nadir location over a power range that should cause the IMT to occur. The blue lines are made 1 degree off the nadir location where SP will not be generated, and the power is from above and below the IMT threshold. 80
- 6.1. 30nm VO₂ on TiO₂ time response for various fluences from 0 to 4000ps. The insert at top right shows times from 0 to 40ps which corresponds to the first 1% of the data and the area of the insert is represented by the small box seen at t=0. The vertical scale of the insert directly aligns with the corresponding main $\Delta R/R$ scale. 85

- 6.2. Simulation of diffusion of the insulating VO₂ into metallic VO₂ layers. Red layers are metallic VO₂. Blue layers are insulating. The colors between represent intermixed values of the optical properties of the VO₂ layers. The black line shows the values of the real component of the index of the reflection. The two graphs (a) and (b) are for 10ps and then 200ps in time. steps for the diffusion of the system. 91
- 6.3. Optical model response of 30nm VO₂ TiO₂ for various relative fluence of light using a 4×4 optical matrix method and the ellipsometry values with a hybrid layer of VO₂ between the insulating and metallic states. The relative fluence at level 1 represents the power to fully transition the film in 200ps with blue light. 92
- 6.4. 30nm VO₂ on TiO₂:Nb time response for various fluences from 0 to 4000ps. The insert at top right shows times from 0 to 40ps which corresponds to 1% of the total data and is represented by the small box seen at t=0 in the main graph. The vertical scale of the insert is equivalent to the main $\Delta R/R$ scale. 94
- 6.5. Time constants for the slow growth and recovery periods of the $\Delta R/R$ for the for the two VO₂ samples. The blue line is for VO₂ on TiO₂ and the red line is for VO₂ on TiO₂:Nb. The insert is the graph of $\Delta R/R$ response of the 30nm VO₂ on TiO₂ at 30 $\mu\text{J}/\text{cm}^2$ (green line) and 30nm VO₂ on TiO₂:Nb at 28 $\mu\text{J}/\text{cm}^2$ (purple line). The time constant fits for both samples are shown as orange for the slow growth fit and black for the recovery fit. 96
- 6.6. 15nm VO₂ on TiO₂:Nb time response for various fluences from 0 to 4000ps. The insert at top right shows times from 0 to 40ps which corresponds to 1% of the total data and is represented by the small box seen at t=0 in the main graph. The vertical scale of the insert is equivalent to the main $\Delta R/R$ scale. 99
- 6.7. Optical model response of 15nm VO₂ TiO₂ for various relative fluences of light, using a 4×4 optical matrix method and the ellipsometry values with a hybrid layer of VO₂ between the insulating and metallic states. The relative fluence at level 1 represents the power to fully transition the film in 200ps with blue light. 100

- 6.8. 22nm VO₂ on TiO₂:Nb time response for various fluences from 0 to 4000ps. The insert at top right shows times from 0 to 40ps corresponding to 1% of the total data and is represented by the small box seen at t=0 in the main graph. The vertical scale of the insert is equivalent to the main $\Delta R/R$ scale. 102
- 6.9. 50nm VO₂ on TiO₂:Nb time response for various fluences from 0 to 4000ps. The insert at top right shows times from 0 to 40ps which corresponds to 1% of the total data and is represented by the small box seen at t=0 in the main graph. The vertical scale of the insert is equivalent to the main $\Delta R/R$ scale.. 103
- 6.10. Optical model response of 50nm VO₂ TiO₂ for various relative fluences of light, using a 4x4 optical matrix method and the ellipsometry values with a hybrid layer of VO₂ between the insulating and metallic states. The relative fluence at level 1 represents the power to fully transition the film in 200ps with blue light. 104
- 6.11. The log log plot of the 30nm VO₂ on TiO₂:Nb at 28 μ J/cm². (From Figure 6.4) The slow growth region is within the light tan colored box. The beginning of the recovery is shown in the pink box. This follows Radue et al. [104]. 105
- 6.12. Time constants for the slow growth of the $\Delta R/R$ for the for the VO₂ samples of various thickness on TiO₂:Nb. The insert is the graph of $\Delta R/R$ response. The time constant fits for samples are shown as red for the slow growth fit and black for the recovery fit. It should be noted that the 50nm only show a single exponential slow growth fit and does not need the second time constant. 106
- 6.13. 1.55eV pump and probe on the 30nm VO₂ sample on TiO₂:Nb for low fluences. Time responses for various fluences from 0 to 4000ps are shown. The insert at top right shows times from 0 to 40ps which corresponds to the first 1% of the data and the area of the insert is represented by the small box seen at t=0. The vertical scale of the insert directly aligns with the corresponding main $\Delta R/R$ scale. 111
- 7.1. From [79] shows the modified band structure at the heterostructure region of the VO₂ on TiO₂:Nb. The generation of

- photocurrent process is also depicted. The Δ^* is the heterojunction region of the sample, E_f is the fermi energy of the system, E_c is the conduction band of the TiO_2 . and E_v is the valence band of the TiO_2 . The red spheres represent holes and the yellow are carriers. 115
- 7.2. From [79] External quantum efficiency on the left vertical axis and the responsivity of the right (responsivity is defined as the current generated per of input light power)which is the gain of the system . The samples are 22nm (blue), 15nm (red), and 10nm on $\text{TiO}_2\text{:Nb}$. The orange line is VO_2 on plan TiO_2 . The green line is Si photodiode response. 116
- 7.3. Simple figure of the modified photocurrent generation set up used to obtain the time constants. The setup is based on what Creeden used in the photocurrent efficiency measurements. 118
- 7.4. The photocurrent response of the 22nm VO_2 on $\text{TiO}_2\text{:Nb}$ sample using the pin location of 1.3mm. The blue line is the VO_2 photocurrent signal the dashed red lines are the single exp. fits of the photocurrent turn-on and recovery responses. The orange line is the Si photodetector pick off response and its axis is on the right. 119
- 7.5. The time constant from the fitting applied to the VO_2 photocurrent response of the 22nm VO_2 on $\text{TiO}_2\text{:Nb}$ sample for the different pin spacing. The blue line turn on response and the red line is the recovery time constant. 120
- B.1. The Yee Cell Figure shows field geometries that are calculated cell by cell through the mesh that represents the structure under study. This cell type lends itself to efficient finite difference computations of the Maxwell equations. 129

CHAPTER 1

Introduction

1.1 Vanadium Dioxide and Its Insulator to Metal Transition.

VO₂ is a transition-metal oxide that is a strongly correlated system. VO₂ is a member of a long list of vanadium oxides VO, V₂O₃, V₂O₅, V₃O₅, V₄O₇, V₅O₉, V₆O₁₁, V₇O₁₃, and V₈O₁₅ [1, 2]. VO₂ has been studied for the past 60 years. It is a quintessential strongly correlated material that undergoes a first order phase transition between a monoclinic crystalline lattice at room temperature to a rutile crystalline lattice at a temperature a little higher than room temperature [3]. In the monoclinic crystalline lattice, VO₂ is an insulating material, while in the rutile crystalline state VO₂ is a metallic state [1]. This transition can show several orders of magnitude change in the conductivity of the VO₂. It is also associated with large changes in the VO₂ optical properties in the IR spectral range [4]. VO₂ stands out from the list of other vanadium oxides in that its transition temperature is located just above room temperature. The relative ease of accessibility to the transition temperature of VO₂ makes it advantageous to study and have led to a large body of work studying VO₂ [3].

There are many ways to induce the insulator to metal transition (IMT) in VO₂, in addition to heating . These include, application of electrical current and or electric fields, shown by Stefanovich and others [5-9]. Pressure is another way of accessing the IMT [10-13]. Finally, strain in thin films can affect the IMT, modifying the critical temperature (T_c) of the transition in VO₂ [10-13].

Interaction with strong optical fields is another process for causing the IMT, which was first seen using a Q-switched ruby laser with a 1.78 eV photon energy and a pulse width of 20 ns [14]. Becker, etc. [15] first showed that the IMT in VO₂ happened on the order of picoseconds. Cavalleri gave insight into structural effects occurring at the fs level [16-18]. Wegkamp explored the photo induced instantaneous band gap collapse of VO₂ [19, 20]. More recent work by Wall used an advanced accelerator based light source to monitor the femtosecond time scales and investigated the fast disordering of VO₂ dimers [21].

Thin films are a useful engineered system that have the potential to create new technologies in the modern world. Thin films are defined to have thicknesses from a few nm to μm [22, 23]. Due to the thickness of these films the material properties can be different from the bulk properties of the material. The differences come from the effect that the substrate properties impart on the film [24]. Thin films of VO₂ have the possibility to be optimized and tailored to specific requirements for new technologies and applications. These technologies often utilize

the IMT in thin films of VO₂ [25-30]. These implementations of the IMT in VO₂, coupled with the fact that VO₂ properties can be tailored, make VO₂ an attractive candidate for use in various metamaterial and optical technologies, such as IR, optical, or plasmonic switches, VO₂ plasmonic modulators, and for infrared camouflage, thermal regulation, and detectors, as well as infrared tagging and labeling [8, 31-35].

1.2 Motivation, Goals and Objectives

The development of better UV and blue light detectors that would be simpler, lighter, and more compact than currently used photomultiplier tubes in γ -ray and neutron detectors motivated these studies of the insulator to metal transition in VO₂.

Surface plasmon polariton (SPP) mediated IMT studies in VO₂ explore the possibility of inducing the IMT in VO₂ with fast simple optical systems. SPP studies are sensitive to optical properties changes such as occur with the IMT in VO₂. These properties can potentially be used for the development of a VO₂ UV/blue light optical detector. Previous work showed SPP could monitor the surface plasmonic resonance (SPR) response behavior of VO₂ during thermal transition of VO₂ with a Au grating sample [36]. It is also possible that SPP could induce the IMT in VO₂ [37]. Hence, the application of SPP could both drive the IMT and detect the transition.

The objective of the SPP part of the thesis was to determine if it was possible to induce the IMT in thin films of VO₂ along with tracking the changes that the IMT of VO₂ causes. A 5nm thick VO₂ sample with an Au layer, used to generate SPP, underwent an IMT at a threshold of 2mW and became fully converted at 5mW of laser power. The IMT changed the SPR nadir (minimum) location of 0.07 degrees. This process was not thermal in nature as shown with the use of thermal imaging.

A further objective was to study the optical temporal response of VO₂ using ultrafast photo induced IMT with 3.1 eV UV light. Studies of the ultrafast photo induced process were implemented on VO₂ on Titanium Dioxide doped with Niobium (TiO₂:Nb). Previous studies showed that TiO₂:Nb substrates could modify the VO₂ IMT transition temperature and could affect the generation of photocurrent when illuminated with blue and UV light [38]. Measurements were made on samples designed for efficient photocurrent generation to determine the effects on the sample's reflectivity by photo inducing the IMT in the 3.1 eV photon range. Those results were compared to VO₂ on undoped TiO₂ substrates. Measurements of the IMT and its time evolution response in VO₂ on TiO₂:Nb showed more sensitivity to transition fluence than VO₂ on undoped TiO₂. The time constant of the samples' slow growth values showed a relationship to the pump fluence. The measurements also showed the sensitivity of the IMT to fluence

in those samples as well as the effects of the 3.1 eV light on different thicknesses of VO₂ and determined that when using 3.1eV light there was an apparent stratification of the IMT effect within the layer.

An important aspect of a photodetector is its rise time and recovery time of detected radiation. Rise time and recovery time constants were measured for photocurrent generation on a 22 nm thick VO₂ on TiO₂:Nb sample using modulated blue (3.06 eV) light and the results were compared to the ultrafast time response of the sample. Photocurrent generation shows several orders of magnitude slower response in both the rise and recovery time constants when compared to the photo induced IMT response.

1.3 Outline

Chapter 2 provides a theory review of the material properties of VO₂ including the crystal structure and energy band structure along with the optical properties; the physics of IMT via heating, electronic processes, and photoinduced process are highlighted. The experimental system for the surface plasmon resonance setup are discussed in Chapter 3 with background for the surface plasmon polariton and the field enhancement, the ultrafast laser system used for pump probe experiment, and the ellipsometry used to determine the optical properties of VO₂ thin film on TiO₂. Chapter 4 describes the samples and their characterization. Results of the VO₂ surface plasmon resonance induced insulator to metallic transition are presented in

Chapter 5. Chapter 6 is devoted to the time resolved pump probe insulator to metallic transition in VO₂ on TiO₂ and TiO₂:Nb. Discussion of the photocurrent generation time constants of 22nm VO₂ on TiO₂:Nb. is covered in Chapter 7 and Chapter 8 draws final conclusions.

CHAPTER 2

Theories and Background for VO₂

2.1 Conductivity in Solids

The advent of modern solid state physics began with the development of quantum mechanics in the early 20th century. The understanding of material electronic and optical properties were greatly improved with the development of electronic band theory.

Bloch proposed that the electron properties inside the periodic lattice can be described by a single electron Hamiltonian with a periodic potential that reflected the lattice:

$$H\psi = \left(-\frac{\hbar^2}{2m}\nabla^2 + U(r) \right) \psi = E\psi \quad (2.1)$$

Where H is the Hamiltonian, ψ is the electron wave function, \hbar is the Plank's constant, m is the mass of the electron, and U is the potential, which has the property that

$$U(r + R) = U(r) \quad (2.2)$$

for all R in a Bravais lattice.

Bloch proposed a wave equation solution for the electron that was similarly periodic behavior:

$$\Psi_{nk}(\mathbf{r}) = e^{i\mathbf{k}\cdot\mathbf{r}}u_{nk}(\mathbf{r}). \quad (2.3)$$

The subscript n is a band index, \mathbf{k} is the wavevector, and u is a local solution of the wave function. Electrons that satisfy the Hamiltonian with energy E_n are said to be in the n^{th} energy band. Bloch's Theorem showed that $u_{nk}(\mathbf{r})$ had the following property:

$$u_{nk}(\mathbf{R} + \mathbf{r}) = u_{nk}(\mathbf{r}) \quad (2.4)$$

for all \mathbf{R} on the Bravais lattice, which implies that the electron wave function has a similar behavior:

$$\Psi_{nk}(\mathbf{R} + \mathbf{r}) = \Psi_{nk}(\mathbf{r}) \quad (2.5)$$

for all \mathbf{R} on the Bravais lattice. This is interpreted to mean that an electron in a given energy band n can move through the lattice in that energy band. There is a correspondence between an electron's atomic orbital state and the energy band n in the solid.

At moderate temperatures, the lower energy bands will be occupied, while the occupation of the higher energy bands may vary according to the Fermi-Dirac distribution. At thermal equilibrium, the Fermi energy level of the system is defined as the energy level where the probability of an electron occupying that energy at any given time is 50%.

If the Fermi level should reside near the middle of a partially filled energy band, then the material is described as a metal (Fig. 2.1 metal column). Examples are Ag, Au, and Pt. When electrons in an energy band have nearby empty higher energy states, then electrons can easily be elevated into those states by an applied electric field. The net current density of the band will sum up to a net current in response to the electric field.

If the Fermi level should reside between two energy bands with a large band gap and the states below the Fermi level are fully occupied, no electron conduction can take place in the material. This is a result of there being no nearby energy states for the electron to move into, under an electric field. The net current density will sum to zero so that there is no current, hence the material is insulating. (Fig. 2.1 Insulator column). For some material types, there are various energy band conditions that lead to defined material types that support modest conductivity. These are materials with no band gap, Semimetal; a very small band gap with the Fermi energy midway, Intrinsic Semiconductor; a small band gap with the Fermi energy near the lowest unfilled band, n-type semiconductor; or a small band gap with the Fermi energy near the valence band, p-type semiconductor. (Fig. 2.1 middle columns). These materials may display weak conductivity under an applied E-field.

2.2 Strongly Correlated Material

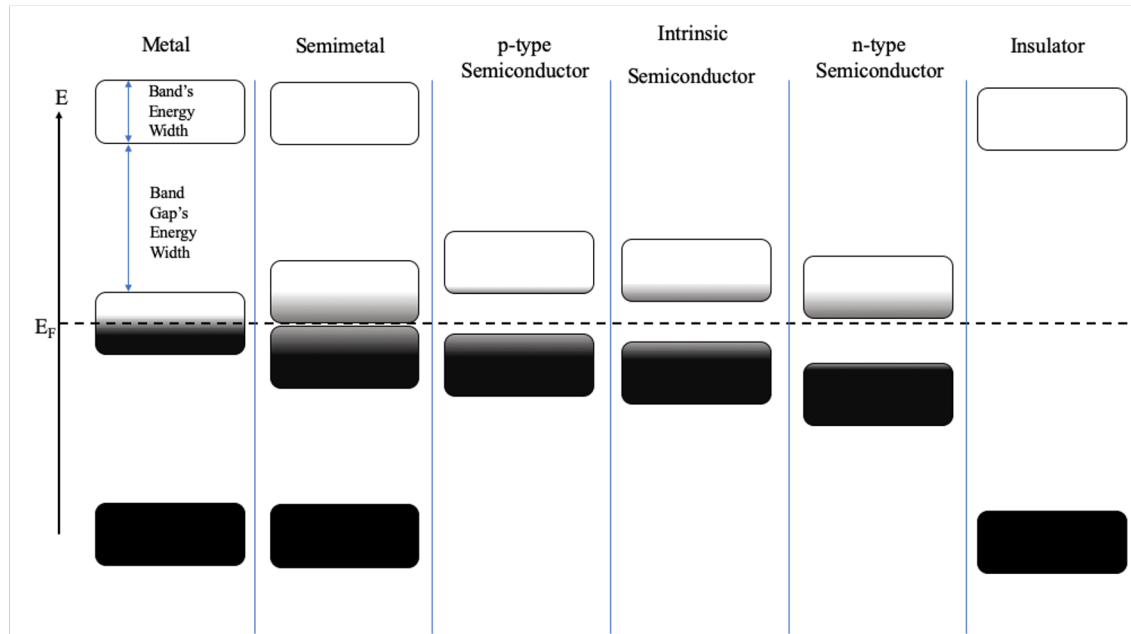


Figure 2.1: The band structure of various materials types. The vertical axis is the energy of the band. The dotted line is the fermi level. As you go from left to right you will see the band valence and conduction band separate. The black color represents electron fill level in the material. Greyed levels represent the case where electrons are partially occupying levels according to Fermi Statistics.

A Strongly Correlated Material is a material that has partially filled d-orbitals yet is insulating or a poor conductor.

The first early successful model of conduction in materials was proposed by Drude [39]. With the advent of quantum theory, early band theories predicted that partially filled electronic orbitals should be good conductors. Yet there were a class of materials including VO_2 that did not follow early theories. Mott [40, 41] and Peierls [42] described how strong electron-electron correlations could impede free electron motion and create different band splittings of the d orbital structures.

A significant amount of strongly correlated materials are transition metal oxides. Transition metal oxides are materials that have a half-filled d-orbital. VO_2 is a quintessential strongly correlated system. VO_2 is insulating at room temperature but can be converted to a metal with a moderate temperature increase. VO_2 and its other oxides were studied as early as 1959 by Morin [3], who showed there is an insulator to metal transition at its critical temperature (T_c). In these early studies the transition was thermally activated and was detected by measuring surface conductivity of bulk crystals that exhibited several orders of magnitudes difference in conductivity [3]. Under early metal theories, VO_2 was expected to be a metal and the insulator case was not expected.

In the study of highly correlated materials pertaining to VO_2 , there are two modes of thought on where the insulator state came from. In 1937, Rudolph Peierls proposed an idea that related the unexpected lack of conductivity with lattice distortions. His theory states that for a 1D crystal lattice, the periodicity creates energy gaps at the edge of the Brillouin zone [42]. This is very similar to the Kronig-Penney model [39] that explained a theory for the origins of band gaps in semiconductors. If each ion contributed an electron, then the band would be half filled in the ground state. Peierls theorem states that a distorted lattice, in which ions have long bonding or short bonding potentials (Fig 2.2) results in a lower energy state. Because there are two different bond lengths forming, new band gaps

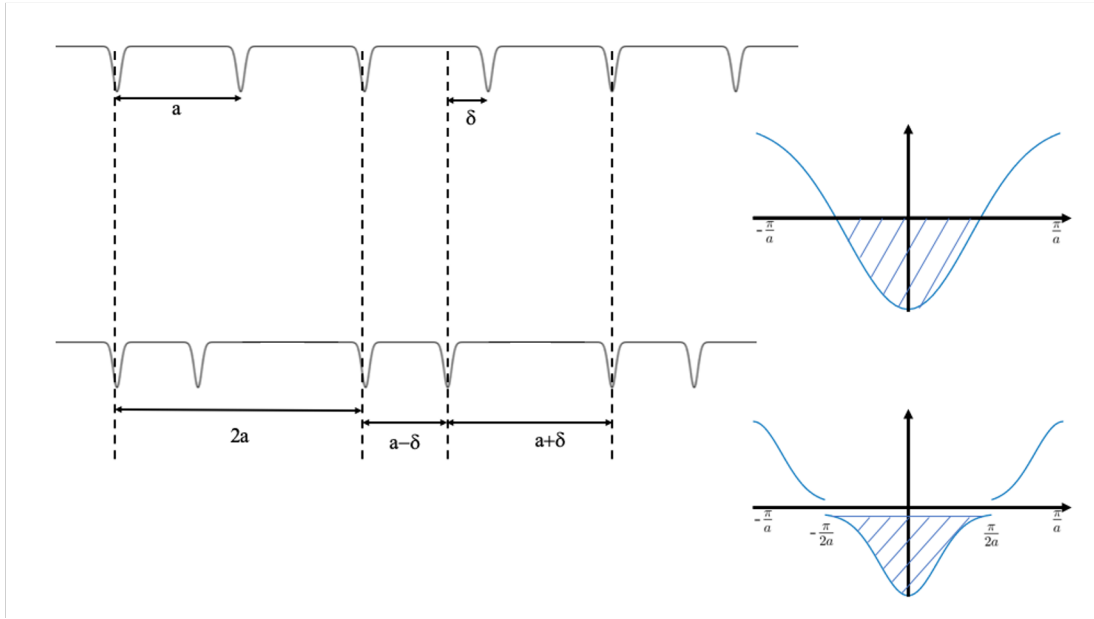


Figure 2.2: Shows simple graphic of a 1D periodic potential. The top line is a 1D periodic potential with equal spacing with the introduction of a perturbation of δ . This creates a distorted 1D periodic potential with a period of $2a$, with alternating potential positions dimerization offset by δ .

are induced and are seen (Fig 2.2). Thus, the lattice had a lower energy state from the splitting of the bands, where the distorted bands are more energetically favorable than a perfect lattice making certain materials behave as insulators in these highly correlated systems. The Peierls transition is more closely associated with thermalization of the lattice and is seen at lower temperatures. Distortion of the lattice that the Peierls transition describes is sometimes called a dimerization. The Peierls transition and theorem is one argument for why the insulator state appears in VO_2 at low temperatures [43].

From the 1950's on, the effect of electronic interactions were proposed for describing the insulating state in strongly correlated systems [40]. This was due in large part to Mott [41], who investigated the role of electron-electron interactions in a lattice with an electron at each lattice position. Without electron-electron interactions, the additional electrons filled the bands without an energy penalty and the electron occupation was simple. Adding the Coulomb repulsion between electrons introduced the possibility of distorting the bands slightly. Mott showed that splitting the bands could lower the net energy of the system, compared to the simple case of a single band, forming an insulating material.

Peierls' and Mott's theories led to numerous debates and studies as to the true underlying mechanism of the insulator to metal transition in VO₂ [43]. Experiments were proposed to elucidate which of those mechanisms was driving the VO₂ IMT. This has been an ongoing area of research for the past sixty years. Recently it was proposed that both of these theories are at play to explain the VO₂ insulating and metallic phases [44].

2.3 VO₂ Crystal Structure

When VO₂ goes through a phase transition there is a physical change to the lattice of the crystal. In its insulating state, VO₂ is a distorted monoclinic crystalline structure, shown in Fig 2.3. Its lattice crystal classification is space group P2₁/c (no. 14) per Shao et al. It has unit cell parameters a=0.575 nm, b= 0.452 nm, c=

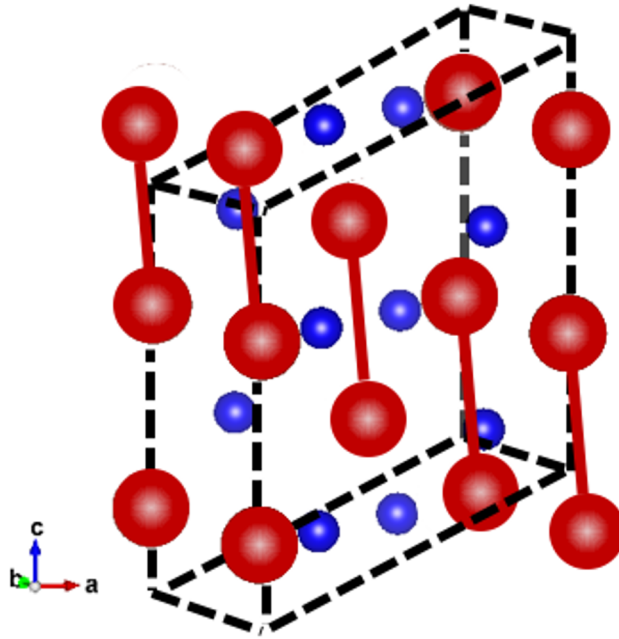


Figure 2.3: Insulating lattice structure of VO_2 with the dotted line shows the unit cell, and the red lines represent the dimers that form from the V ions. Red spheres indicate the V atoms and blue spheres indicate the oxygen atom.

0.538 nm, $\beta = 122.6^\circ$ [20, 45, 46]. The solid red lines in Fig 2.3 highlight the dimerization of the vanadium atoms off the lattice.

The lattice classification of the metallic phase of VO_2 is a rutile structure which is also tetragonal as shown in Fig 2.4. It has a space group of $P4_2/mnm$ (no. 136). The cell parameters are $a=b=0.455\text{nm}$, $c=0.286\text{ nm}$. Fig 2.4 shows the two crystal phases overlaid to highlight the difference. Red spheres represent the vanadium atoms, and the blue spheres represent the oxygen atoms in the unit cell of VO_2 .

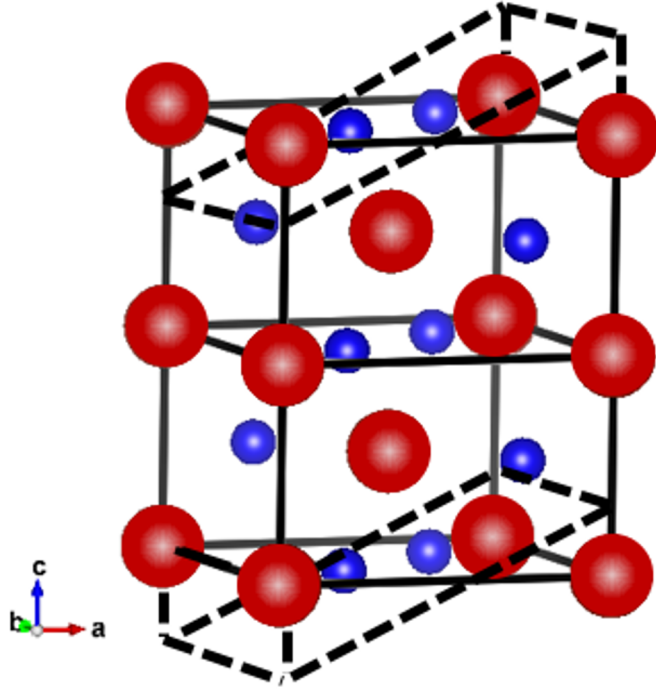


Figure 2.4: Metallic crystal structure of VO_2 . The solid line represents the unit cell of the VO_2 in metallic state. The dotted line represents the cell for the insulator state.

2.4 Energy Band Structure in VO_2

VO_2 band structure was first described by Goodenough [1], and can be explained by d orbitals in the vanadium being hybridized due to the octahedral oxygen atoms that are located around it [45]. In the insulator state, the d orbital splits into a $d_{||}$ band and a d_{\perp}^* band along with a Π^* band. The d_{\perp}^* is a conduction band that lies above the Fermi energy while the other bands are filled valence bands. This band structure is shown in Fig. 2.5. Typically, the reported value for the band gap

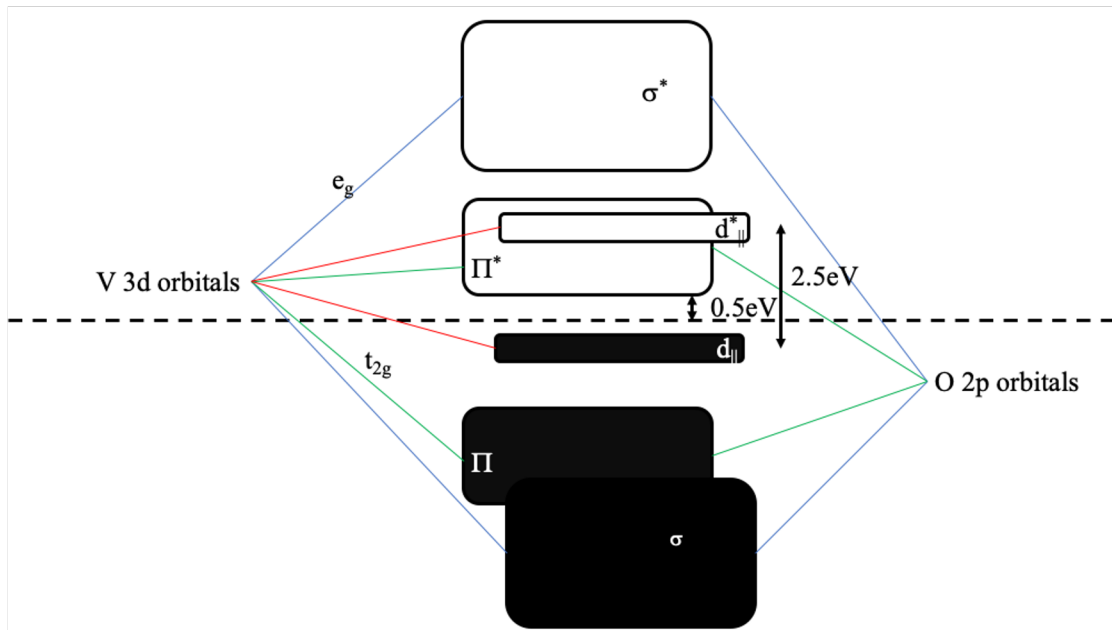


Figure 2.5: Band representation of the insulating case of VO_2 and the orbitals being used to form the bands.

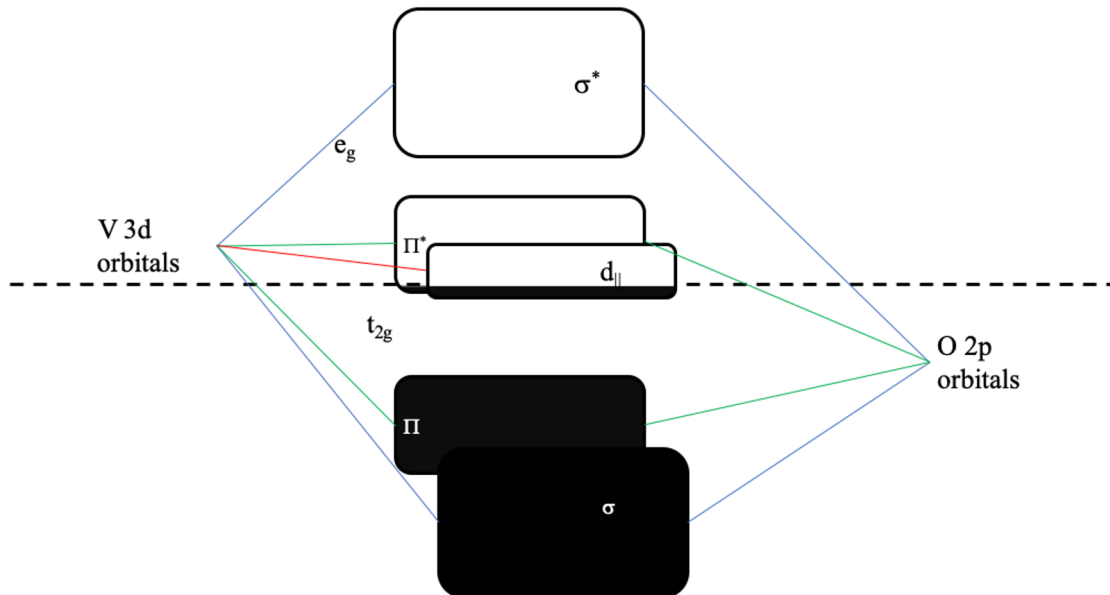


Figure: 2.6 Representation of the metallic case of VO_2 with orbitals used to form the bands.

is 0.5 eV above the fermi level, and band widths between the $d_{||}$ and $d_{||}^*$ are around

2.5 eV [2, 41, 43, 45, 47].

In the metallic state the band structure is different, with the d_{\parallel} and d_{\parallel}^* bands coalescing into a single d_{\parallel} band that resides across the Fermi energy level. The Π^* band also shifts downward to straddle the Fermi level, as seen in Fig. 2.6.

2.5. VO₂ Optical Properties

As VO₂ goes through the IMT, changes are seen in the band structure that represent corresponding changes to the optical properties between the two states of matter. In these experiments, most of the measurements are optical in nature, and knowledge of the optical properties of the material is necessary for analyzing the results. These optical properties are reflected in the complex index of refraction [4]. Fig. 2.7 shows the changes occurring in 30nm of VO₂ on c-plane sapphire. The blue lines represent the insulating case and the red lines represent the metallic case.

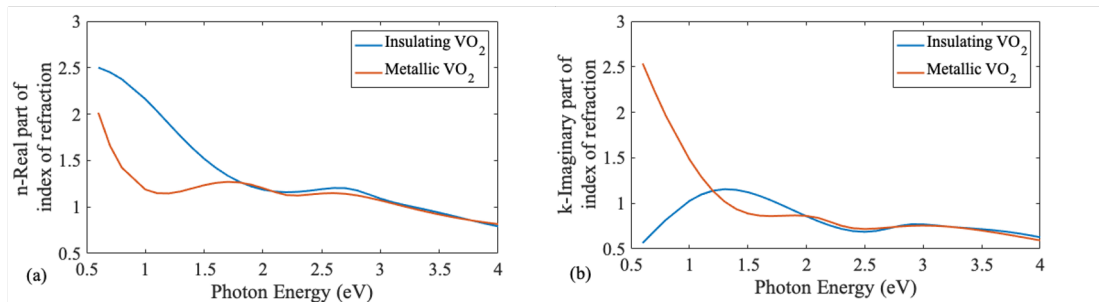


Figure 2.7: (a) Real and (b) imaginary component of VO₂ refractive index as a function of the photon energy. Measurements are for a 30nm thick VO₂ film on c-plane sapphire.

Panel (a) of Fig 2.7 shows the real components of the index of refraction and panel

(b) show the imaginary components of the index of refraction. There are differences noted between the two states. Noticeable in the lower photon energy (IR range), the larger extinction coefficient, k , is seen in the metallic data, which is indicative of metals [39].

2.6 Insulator to Metallic Transition Theories

2.6.1 Thermally Induced IMT in VO₂

One of the first identified methods of inducing the transition of VO₂ was heating of a VO₂ sample [3]. Increasing the temperature caused two effects in a VO₂ sample [3]: it removes a lattice dimerization and modifies the electronic structure. Bubai et al. [48], who performed first-principle calculations along with x-ray and neutron scattering measurements on VO₂ to support those calculations, showed that as heat was added into the lattice, the vanadium atom orbitals began to increase the electron density in the $d_{x^2-y^2}$ (Π^* band) orbitals while the d_{xz} and d_{yz} ($d_{||}$ bands) decreased their electron densities. Once the band energy differences between the electron bands increased by a sufficient amount, a Peierls instability caused the lattice to shift. This resulted in the lattice switching from the lower energy insulating monoclinic structure into a higher entropic metallic rutile structural state by removing the dimerized V lattice locations. This model is reasonably accurate for describing the thermodynamic IMT.

Another feature of thermally induced IMT in VO₂ is thermal hysteresis. It was observed in both VO₂ resistance or CW optical properties when the temperature was swept across the IMT threshold value in different directions, (Fig. 2.8) [49]. The presence of hysteresis, is a common characteristic of first order phase transitions [50].

This transition process was imaged showing random microscopic regions of VO₂ undergoing the IMT [50]. Those regions expanded and coalesced as the temperature changed until the whole sample was converted. The hysteresis width can be on the order of a few degrees to tens of degrees in macroscopic materials and <1°C in real crystals [51, 52]. Hysteresis can be affected by the sample's crystalline structure, ie. single crystal vs. polycrystalline, the presence of defects,

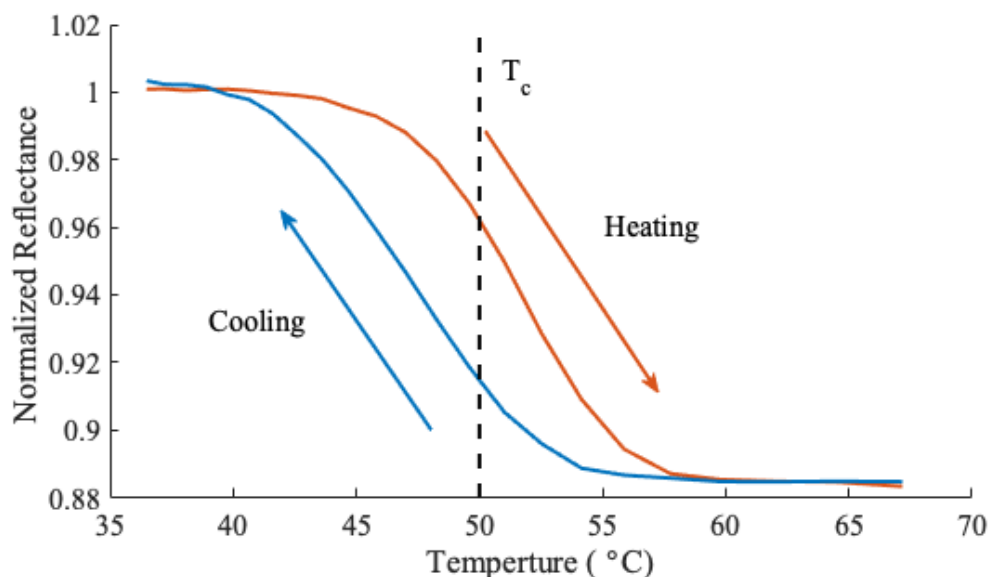


Figure 2.8 The normalized reflectance of a 30nm thick sample on TiO₂ when illuminated with 700nm light as the sample is thermal transitioned. The sample had a T_c of approximately 50±5 °C and shows a hysteresis between heating and cooling of the sample.

and doping, etc. [53-59]. Studies on controlling or modifying the IMT temperature and the width of the hysteresis curve in VO₂ are important to support applications of VO₂ in technologies.

2.6.2 Electric Field Induced IMT

Another method of inducing the IMT in VO₂ is the application of strong electric fields. Both Peierls and Mott-Hubbard interactions can describe such processes. This transition methodology was implemented with Metal-Oxide-Metal devices [60-67]. In those cases, the transition via the electric field was described as joule heating coming from the electric current generation in the sample. The generation of heat brought the VO₂ up to its T_c. For these types of devices that used the electric field to transition, the voltage required to cause the transition was lowered as the temperature approached the T_c of the VO₂. The electric field switching method described in these earlier papers was considered “the model of critical temperature” [67].

$$V_{th} \propto \sqrt{T - T_c} \quad (2.6)$$

This simple model states that as the temperature of the sample is raised, the voltage requirement to cause the IMT is lowered. In studies of field enhancement caused by surface plasmons (section 3.1.2), the enhanced electric fields can influence the IMT. The electric field effect is quite similar to the Poole-Frenkel effect [68], revealing the number of carriers dependence on the electric field strength:

$$n = N_o e^{\left(\frac{-W-\beta\sqrt{E}}{k_B T}\right)}. \quad (2.7)$$

Here N_o is a constant that has a slight temperature dependence but no dependence on field strength, W represents the conductivity activation energy, β represents the Poole-Frenkel constant, E is the electric field, k_B is the Stefan-Boltzmann constant and T is the temperature. The Poole-Frenkel constant, β , depends on the high frequency dielectric permittivity and the vacuum permittivity along with the electrical charge.

$$\beta = \sqrt{\left(\frac{e^3}{\pi\epsilon_\infty\epsilon_o}\right)} \quad (2.8)$$

When the number of free carriers is elevated to a critical value, the IMT is initiated. The critical number of carriers for VO₂, n_c is determined by the Mott criterion [41]:

$$a_H n_c^{1/3} \approx 0.25 \quad (2.9)$$

Where $a_H = \epsilon\hbar^2/m^* e^2$ is defined as the effective Bohr radius and m^* is the effective mass of the charge carriers [68]. The dielectric constant for VO₂ is approximately 100 [69], the m^* value for VO₂ is about $3m_e$ [41], giving the n_c value for VO₂ as $3 \cdot 10^{10} \text{ cm}^{-3}$.

The application of electric field increases the VO₂ carrier density. This increase of the carriers will, in effect, screen Coulomb interactions. The screening of the Coulomb interactions will lead to a collapse of the Mott-Hubbard energy gap

that supports the insulator phase of VO₂ [5, 68, 70]. The field induced generation of additional carriers is caused by the lowering Coulomb barrier lowering which is, in effect, auto-ionizing. Once the n_c value exceeds a carrier density of as $3 \cdot 10^{10}$ cm⁻³, the VO₂ will experience a band gap collapse.

2.6.3 The Ultra-Fast Photo Induced IMT

2.6.3.1 Pump-probe physics

With the advent of ultrashort laser pulses on the order of 100s fs and shorter, the ability to investigate material physics at this timescale becomes possible [71]. The fine time resolution of such laser pulse systems allows fast dynamic processes to be studied and their temporal signatures found.

When photon energy is greater than the material's bandgap, the photon is absorbed, generating photoelectron carriers in the conduction band. Interband absorption of photons can happen in two different ways: absorption via a direct process excites carriers straight into the conduction band if the energy of the photon is sufficiently high.

$$E_\gamma \geq E_{gap}. \quad (2.10)$$

The second method is an indirect process which requires a scattering event to occur, in which a phonon is created to conserve crystal momentum of the lattice:

$$E_\gamma \geq E_{gap} - E_{phonon}. \quad (2.11)$$

Fig 2.9 illustrates these two processes.

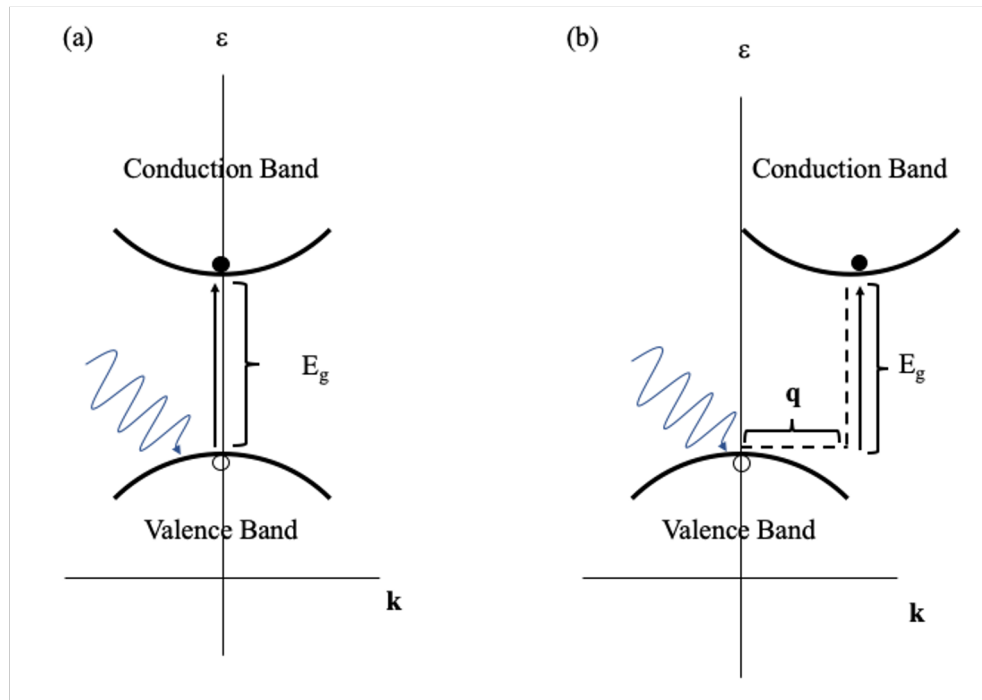


Figure 2.9 A graphic of two types of photon excitation processes in semiconductors: interband direct absorption seen in (a) and interband indirect absorption seen in (b).

Immediately after photon absorption, the material responds to such excitation by undergoing several stages. Each stage has a characteristic time. During the first 200 fs, known as the coherent regime, the electrons in excited bands participate in momentum scattering, carrier-carrier scattering, and hole-optical phonon scattering. That is then followed by non-thermal events such as electron-hole scattering and electron-optical phonon scattering occurring in less than 2ps. The next stage includes carrier-acoustic phonon scattering and decay of optical phonon events, and typically lasts from 1 to 100ps. It is referred to as the

Hot Excitation Regime and is typically 1 to 100ps. Finally, there is carrier recombination which is the isothermal regime at >100ps times. [72]

Another important physical parameter is the penetration depth of the pump light into a sample, δ , where

$$\delta = \frac{\lambda}{4\pi k} \quad (2.12)$$

Which is related to the light absorption coefficient, α , where

$$\alpha = \frac{4\pi}{\lambda} k. \quad (2.13)$$

In very thin samples, in which the thickness is small compared to the penetration depth, the laser power may be uniformly distributed throughout the thickness of the VO₂. For very thick samples, most of the absorbed light is at the front of the thin film.

2.6.3.2 Ultra-Fast IMT models for VO₂

The ultrafast photo induced process is one of the more powerful ways to study the physics of the IMT in VO₂. A short laser pulse has the ability to excite electrons into conduction bands where the light and fast-moving electrons can respond before phonon and lattice effects in the sample can occur. Thus, the electronic and lattice effects can be observed over time if there is enough temporal resolution with the laser system.

Theories of the VO₂ ultrafast photo induced IMT developed over time with changes and improvements being added as new results give more insight into what

was occurring within the lattice. Theories support the concept that the bandgap collapse of the $d_{||}^*$ and $d_{||}$ band into a single continuous band overlapping with the Π band at the Fermi level is almost instantaneous [16-18]. The structural effects of lattice changing were explored by Cavalleri [17, 18] who noted a structural bottleneck of the reorientation of the V ions in the VO_2 lattice of the system, lasting about 80fs after photo excitation. Later, Lysenko and Vikhnin attributed the IMT to Frenkel excitons and Wannier-Mott excitons [73, 74]. That work was followed by van Veenendaal's model for the photoinduced IMT [75].

Van Veenendaal's model is a good conceptual model to describe the photo induced IMT in VO_2 showing the interplay of the structural and electronic interactions. This model describes the ultrafast transition of VO_2 within the first 160 fs. The model incorporates optical excitation, electron-electron scattering, and coherent motion of vanadium dimers along with the changes to the electronic structure of VO_2 . In this model the insulator state of VO_2 is caused by the dimerization of vanadium atoms that give the electronic structure that was defined by Goodenough [1].

The process is shown in progressively longer time steps in Figures 2.10 and 2.11. At $t=0$, a light pulse excites electrons across the band gap into both the $d_{||}$ and the Π bands. In the first few steps, the conduction bands begin to partially fill (Fig. 2.11). Immediately after the pulse, the V atoms start to respond to a change

in their original potential well which is beginning to distort as a consequence of the electrons entering the higher electron bands. After 40fs the bands' distortion begins

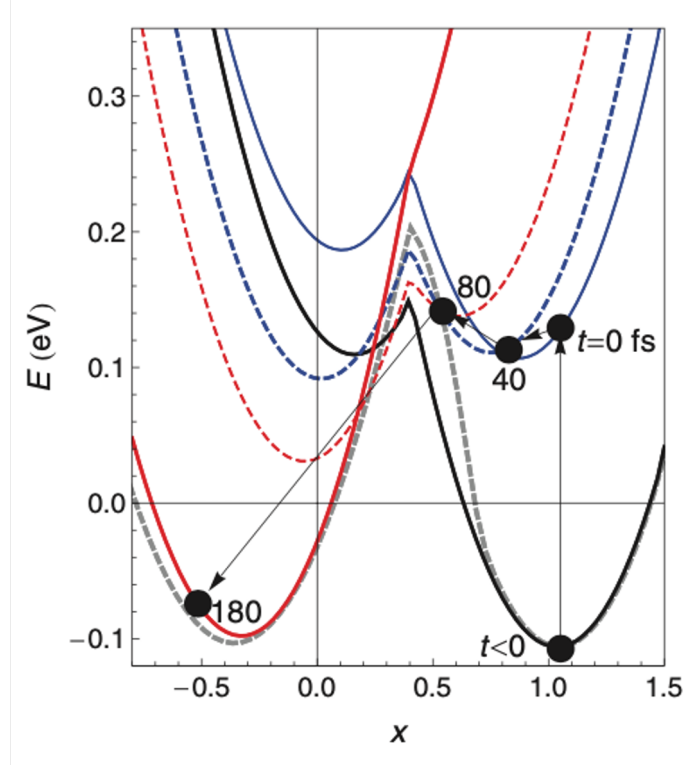


Figure 2.10 Shows the potential that the V atom that make up the V dimerization in VO_2 experience under the photo induced IMT. The x axis and coordinate are generalized to the displacement that describes the V dimer in VO_2 . With the $x=1.05$ being full dimerization (insulating case) $x=-0.36$ represents no dimerization. The curve is the potential that takes into account the occupation of electrons in the bands, n_{\parallel} in the valence band and n_{π} in the conduction band. The dashed grey line is the total electronic and potential energy of the system that covers both insulating and metallic case for the generalized coordinates. The solid black line is the potential for the case for the insulating state. The solid blue line is the case for just after photo excitation has happened (meaning number of electrons, n_{π} , are in the Π band). The dash blue line is 40fs after excitation and the dashed red line is 80fs after the start. Finally, the solid red line is the final state which is metallic. The black dots represent the V atom position at each of those time locations.

Figure reproduced from [75]with permission from Phys. Rev. B.

to drive the V atoms to a slightly new lattice position in the lattice and the

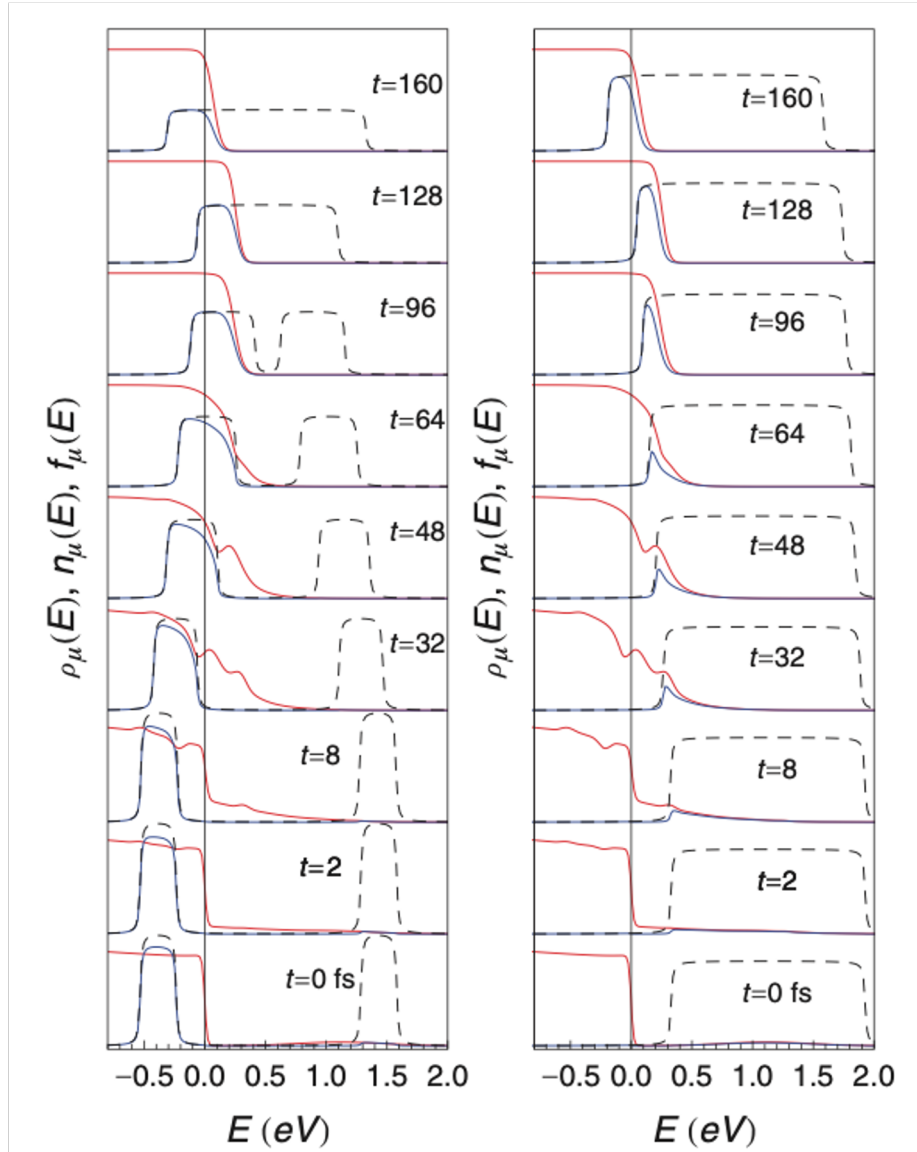


Figure 2.11 Left panel is the density of states of the d_{\parallel} band progressing through time in the vertical direction with the splitting being shown through the density of states (dashed-gray lines), the electron occupation is the red lines and the electron density is the blue lines. Right panel is density of states of the Π band seen with the same line colors. As the system is photo induced the changes in the band structure show the progression of the n_{π} electron density shifting and collapsing into the n_{\parallel} electron density into a signal band.

Figure reproduced from [75] with permission from Phys. Rev. B.

potential well begins to develop evidence of a second weak potential well in the vicinity of the V atom coordinate at $x \cong 0$ (Fig. 2.10) This causes further band filling (Fig 2.11) and is accompanied with additional V potential well distortion. After about 80 fs, the developing double potential well begins to favor a new position of the V atom, although there is a small potential barrier that blocks full conversion at this moment (Fig. 2.10) and the electron occupation of the Π band is filling while the $d_{||}$ and $d_{||}^*$ bands are collapsing closer together (Fig. 2.11). If the laser light pulse promotes enough electrons into the Π band, at this point in time, the V potential well fully shifts over to a new position of the V atoms (Fig. 2.10). At which time, the $d_{||}$ and Π bands collapse. Alternatively, if the number of excited electrons are not sufficient enough, after about 80fs time frame, the system will relax back to the insulator state. This time frame is the source of the structural bottle neck that is reported in literature [76, 77] Van Venedaal’s model does not incorporate all the new observations and experimental data that is now available due to the advances in recent light sources. More recently Wegkamp suggests that the IMT is in part driven via photoexcitation generated holes which affects lattice screening and his contribution is to add the effect of hole screening. Inclusion of the lattice screening allows the band gap to collapse faster, which separates it from the coherent motion of the vanadium dimers. This is followed by hot carrier relaxation and is then stabilized by structural evolution [19, 20] . Wall’s additional

insight addresses the ability of the vanadium dimers to displace at very high rates. Meaning that even the disordered motion of the vanadium atoms allow the IMT to occur whereas previous authors required a coherent displacement of the vanadium atoms for the IMT to occur [21].

CHAPTER 3

Experimental Arrangements

Several experimental apparatuses were used for this work. One system generated and monitored SPR in a VO₂ sample. A pump probe system performed time resolved measurements of VO₂ samples. Photocurrent generation used a method described by Creeden [78, 79] with some minor adaptations to get time constants from the photocurrent generation.

3.1 Surface Plasmon Resonance System

3.1.1 Surface plasmon polaritons

SPP, are charge waves that form at the boundary of a metal surface. Certain physical boundary conditions must be met to generate SPP. For SPP to be generated they require a material with mobile electrons [80, 81], which come from the metal surface at the interface. The better the electrical conductivity of the conductor at the frequency being used, the stronger the charged waves will be. This is a guided wave and will follow the surface of the metal-dielectric interface. All electromagnetic guided waves follow a dispersion curve derived from Maxwell's equations. Raether showed that for a charge wave traveling in the x direction with

the E-field oriented in the z direction, the dispersion equation has a z -component of an SPP at the metal to dielectric interface and given by:

$$D_0 = \frac{k_{z1}}{\epsilon_1} + \frac{k_{z2}}{\epsilon_2} = 0, \quad (3.1)$$

where the subscript 1 refers to the metal element and subscript 2 refers to the second material in the layered system [80]. k_{z1} is the wavevector in the z direction (into the metal) and k_{z2} is z component of the wavevector in the adjacent material

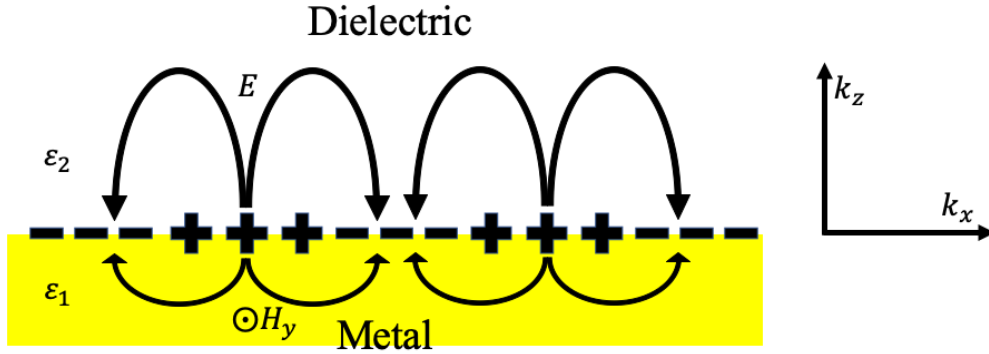


Figure 3.1 Shows the SPP at the interface of a metal to dielectric surface. The SPP is propagating in the x direction and the generated E field is in the z direction. The H_y field is pointing out of the page. The orientation of the wavevector are shown to the right.

(into the secondary material). The dielectric constant ϵ_1 of the metal is complex, while the dielectric constant ϵ_2 of the material 2 is assumed to be real. The wavevectors in the x -direction are required to be continuous across the interface to maintain the wave. The following relationship of the wavevectors in both the x and z directions:

$$k_{zi} = \sqrt{\varepsilon_i \left(\frac{\omega}{c}\right)^2 - k_x^2}, \quad (3.2)$$

where the index i is the material 1 or 2. From eq 3.2 and 3.1 the wavevector for the SPP is fully determined [80] :

$$k_x = \frac{\omega}{c} \sqrt{\frac{\varepsilon_1 \varepsilon_2}{\varepsilon_1 + \varepsilon_2}} \quad (3.3)$$

Because ε_1 is complex, $\varepsilon_1 = \varepsilon_1' + i\varepsilon_1''$, the k_x also has a complex solution:

$$k_x' = \frac{\omega}{c} \sqrt{\frac{\varepsilon_1' \varepsilon_2}{\varepsilon_1' + \varepsilon_2}} \quad (3.4)$$

$$k_x'' = \frac{\omega}{c} \left(\frac{\varepsilon_1' \varepsilon_2}{\varepsilon_1' + \varepsilon_2}\right)^{2/3} \frac{\varepsilon_1''}{2(\varepsilon_1')^2} \quad (3.5)$$

Since in metals $\varepsilon_1' < 0$, the only real solution that allows SPP is $|\varepsilon_1'| > \varepsilon_2$.

Ideally ε_1'' is kept small because it represents a damping term. This derivation only works for p-polarized light.

With k_x defined by Eqs. (3.4, 3.5), SPP are possible in principle in the geometry shown in Fig. 3.1. Light with a k_x wavevector component that matches equation 3.4 will couple to the metal generating the SPP. Experimentally, a glass cylindrical half prism is used in the geometry shown in Fig. 3.2. Light enters the cylinder perpendicular to the cylinder's wall and, based on the angle at the flat side, it refracts by Snells' law. An angle where the light's k_x vector component equals the SPP k_x is the condition where SPPs are generated, which is given by:

$$k_x = \frac{\hbar\omega}{c} \sqrt{\varepsilon_0} \sin \theta_0, \quad (3.6)$$

where ϵ_0 is the dielectric function of the prism, θ_0 is the incident angle of the light and ω is the frequency.

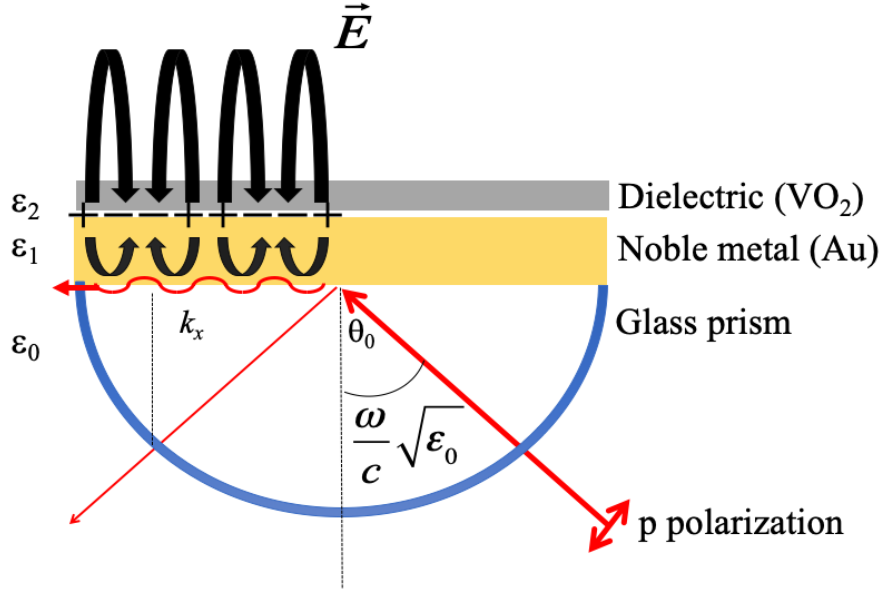


Figure 3.2 Shows the SPP at a metal to dielectric surface interface. This is an example of the Kretschmann method for generating SPP. The angle θ_0 is angle where the light k_x wavevector component equals the plasmon k_x wavevector. In our experimental apparatus, the metal is gold and dielectric is VO₂.

As the incident angle θ_0 of light is changed, a surface plasmon resonance (SPR) is mapped out with respect to the angle of the reflectance of light. A simulation of the SPR on a surface of 31nm of Au and 5nm of VO₂ (Fig. 3.2) shows the strong resonance point seen as a minimum value in reflectance curve.

SPP are a useful tool in studying physical systems. SPP are sensitive to any change to the surface of the material attached to the metal that the SPP are propagated on [82]. This makes an ideal method to detect changes that occur as

VO₂ goes through an IMT when VO₂ is grown on the metal layer because SPP are sensitive to changes at the surface

3.1.2 SPP Field Enhancement

Electron density build-up associated with a charge wave, induces a surface

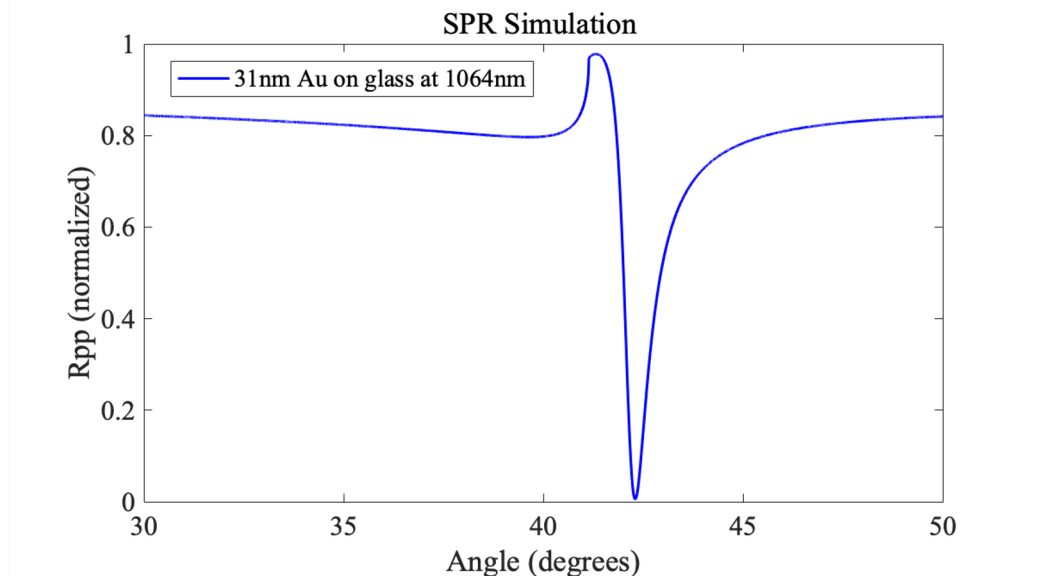


Figure 3.3: SPR simulated response of the reflectance of p polarized light at 1064nm on 31nm Au with 5nm of VO₂.

electric field enhancement to cause the IMT in VO₂

Field enhancement is calculated from the ratio of the field intensity at the two interfaces::

$$\frac{|H_{y(2/1)}|^2}{|H_{y0(0/1)}|^2} = |t_{012}^p|^2. \quad (3.7)$$

H_y field components in equation 3.7 are the magnetic fields in the y-direction, seen in Fig. 3.1 pointing out of the page. t_{012}^p is the Fresnel's transmission coefficient

for the system. Fresnel's equation can be written as an expression of the dielectric functions:

$$|t_{012}^p|^2 = \frac{1}{\varepsilon_0} \frac{2|\varepsilon_1'|^2}{\varepsilon_1''} \frac{\sqrt{|\varepsilon_1'|(\varepsilon_0-1)-\varepsilon_0}}{1+|\varepsilon_1'|} \quad (3.8)$$

The following equation can be used to maximize the electric field enhancement and derived by [80]

$$\left(\frac{|H_y(2/1)|^2}{|H_{y0}(0/1)|^2} \right)_{max} = \frac{\varepsilon_2}{\varepsilon_0} \left(\frac{|E(2/1)|^2}{|E_0(0/1)|^2} \right)_{max} = \frac{1}{\varepsilon_0} \frac{2|\varepsilon_1'|^2}{\varepsilon_1''} \frac{\sqrt{|\varepsilon_1'|(\varepsilon_0-1)-\varepsilon_0}}{1+|\varepsilon_1'|} \quad (3.9)$$

In these equations, the electric field enhancement is dominated by the dielectric properties of the metal, Eq. 3.9, by the term of $\frac{|\varepsilon_1'|^2}{\varepsilon_1''}$. The maximum electric field amplitude occurs at the minimum or nadir location of the SPR curve [80]. At the nadir, maximum light energy is being converted into SPP, seen as the loss of reflectance and referenced as the attenuated intensity reflection . Fig. 3.3 shows the nadir to be at $\sim 42^\circ$. The narrower the SPR the stronger the field enhancement will be [80].

3.1.3 Experimental SPR Setup

Figure 3.2 shows a schematic representation of the sample in an attenuated intensity reflection setup. The laser light is incident into a cylindrical glass prism from the bottom right, travels through the sample's glass substrate and reflects off the gold layer. SPP are generated at a critical incident angle at the glass-Au surface

interface. Index matching fluid was used between the glass substrate and the glass

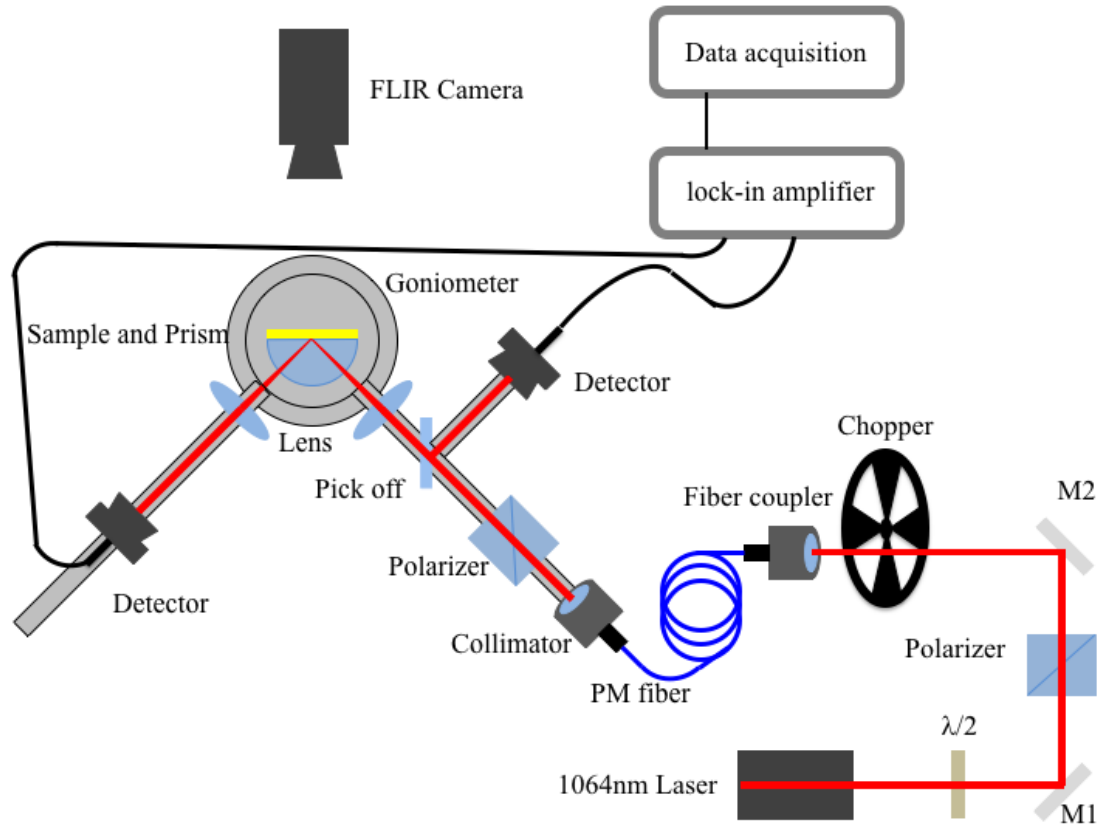


Figure. 3.4 Diagram of the experimental setup. The lock-in-amplifier is set up to perform a differential measurement from the sample signal and the pick off.

prism to maximize transmission through the system and to avoid parasitic reflections at the gap.

The attenuated total reflection assembly for SPP monitoring Fig. 3.2, was mounted at the center of rotation of a goniometer shown in Fig. 3.4 that had an accurate angular resolution of 0.004 degrees. While the sample was accurately located at the center of rotation, the orientation of the sample was set by eye and was difficult to get the sample perfectly normal to the goniometer stage. This could

lead to small angular errors. To avoid possible repositioning errors, all measurements were made without changing the sample's original position, once mounted.

The full experimental apparatus set-up is shown in Fig. 3.4. The arms of the goniometer operated in a θ , $-\theta$ motion, where both the goniometer arms rotated together in opposite directions. This kept the incident and reflected angle the same throughout the measurement. Each goniometer arm was always operated in the same rotation direction during the data acquisition to remove possible backlash errors in the goniometer motion. One arm of the goniometer held the output of the single mode polarization maintaining fiber followed by the polarizer set to transmit p-polarized light, a signal pickoff for power reference measurements, and a lens with focal length 76.2 mm focusing the laser beam onto the sample. The lens focuses the beam to an elliptical spot with a vertical minor axis of $45\mu\text{m}$ and a major axis in the range of $62\text{-}64\mu\text{m}$ (which varies with the incident angle). The second arm of the goniometer held a collimating lens and photo detector. A thermal imaging camera monitored the sample temperature for any laser heating effects.

A Nd:YAG 1064nm laser and other optics were located on a nearby optical table and were coupled into a polarized maintaining fiber optic cable. A half-wave plate and polarizer in front of the fiber coupler controlled the laser light power on the sample. A mechanical chopper modulated the laser beam power at 503 Hz, and

the read-outs from both the laser pickoff and signal detector were inputted to a lock-in amplifier. A differential measurement reduced the effects of any laser power fluctuations by subtracting the pick off power reference signal from the main signal. The output of the lock-in amplifier was recorded with a computer via a USB data acquisition module.

The nadir position of the SPR for each laser power level was measured by monitoring the reflectance during the uniform angular motion from a lower angle below the total internal reflection point to a higher angle beyond total internal reflection. For each recorded position, the goniometer motion was stopped for 20

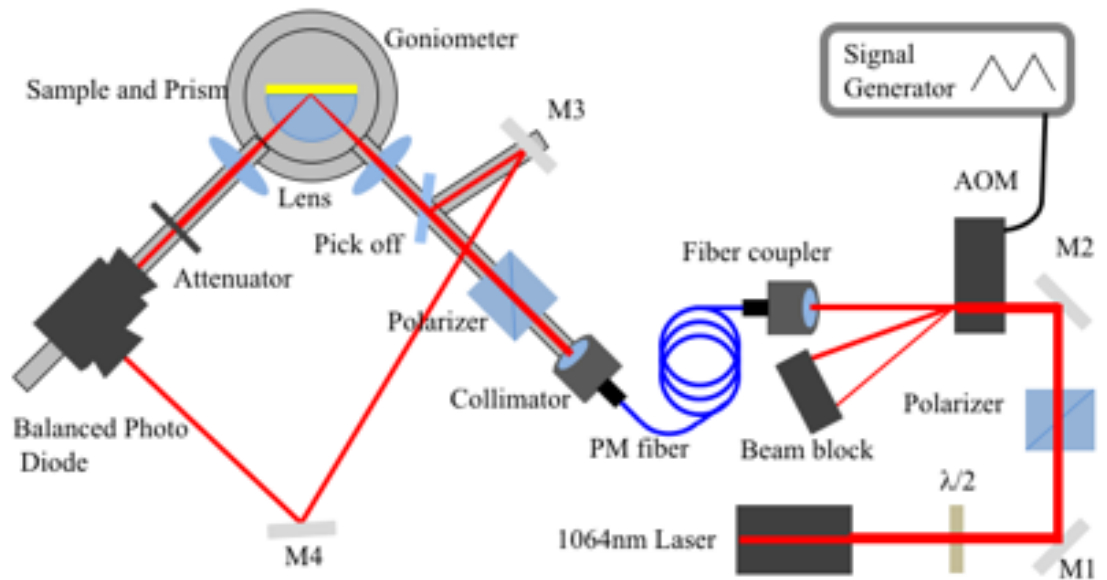


Figure. 3.5 Diagram of the experimental setup used for variable intensity measurements.

seconds to allow vibrations to settle before acquiring the reflection response. At each angle, data was collected for 100 seconds with a data acquisition system operating at 16kHz to extract the average and variance signal. The stage was then moved to the next angle, repeating the data acquisition process until the SPR angular response was mapped.

In the previous set up, the measurements were made angle by angle and at each angle the signal was averaged over time. As will be explained later in Sec. (5.3), we also needed to track the change in the SPR reflectivity as a function of incident laser power for a fixed angle.

For these measurements, the SPR set up was changed as shown in Fig. 3.5, and the chopper was replaced with an acousto-optic modulator (AOM). The AOM used Bragg diffraction to diffract a certain amount of power from the beam. The AOM was used to vary the laser power by using a triangular waveform for a drive signal. A balanced photodetector was used instead of using two individual photodetectors to give a better signal to noise. An oscilloscope captured the data from the detectors.

3.2 Ultrafast Laser System / Pump-Probe System

3.2.1 Ultrafast Laser System

A multi-based laser system was used for the time resolved pump probe experiments, consisting of a mode locked Ti sapphire oscillator (Mantis), seeding the regenerative ultrafast amplifier (Legend Elite).

The mode locked Ti sapphire oscillator outputted short laser pulses of approximately 60 fs in duration with a repetition rate of 80 MHz and typical average power of 430mW. An average energy per pulse was approximately 5.4nJ. The gain medium for the laser was a Titanium-doped sapphire ($\text{Ti}^{3+}:\text{Al}_2\text{O}_3$) crystal. The larger gain bandwidth of the Ti^{3+} ions provided a wide wavelength tunability, and thus was used to generate short pulses with high optical bandwidth. The Ti sapphire can amplify light with a wavelength range of about 680nm to 1100nm. The maximum gain is at 800nm, so most cavity optics are optimized for generating wavelengths around 800nm [83]. The Ti sapphire gain media was pumped at 532nm with a frequency doubled neodymium doped in yttrium lithium fluoride crystal (Nd:YLF) laser that outputs 5 watts of CW power.

Fundamentally, the Mantis was engineered to support the generation of multiple cavity modes that are locked in phase, thus adding up to a high intensity short pulse of light [84]. To sustain this operational regime, a Kerr lens method which changes the beam focus and self-selects the higher intensity phase-locked pulse was used, because it had a smaller spot size due to nonlinear self-focusing [83, 85]. The use of the Kerr lens method made the laser system modelock passively,

so that once the generation started no extra active components were needed to keep the generation of the pulses going. A telecoil was used to generate an initial power fluctuation in the cavity and triggered the Kerr lens system mode locking.

The rep rate of the laser was related to the time-of-flight of a round trip of the pulse inside the cavity. The cavity is from the high reflector to the output coupler, with a the time of travel of 12.5ns and which gives a 80MHz rep rate [83].

The second part of the laser system was a Ti sapphire regenerative amplifier and was used to amplify the oscillator pulse so the output of the Ti sapphire oscillator is a 60 fs pulse with 5.4 nJ. That pulse energy and duration cannot be amplified as is. There is a damage limitation to the optics and gain material from high peak intensity beams which have a tendency to self-focus due to non-linearity in the index of refraction. This self-focusing is destructive if uncontrolled. The main way of avoiding damage is by keeping the intensity in the regenerative amplifier below 10 GW/cm² [86]. Damage is avoided by chirped pulse amplification [85-87], Taking a short 60 fs oscillator pulse and stretching it in time lowers the pulse's peak power. Now the lower peak power pulse can be amplified safely without damaging the system. Once the amplification of the pulse is complete it can be compressed back into a short 150 fs pulse with high peak power.

The initial pulse was stretched with the use of diffraction gratings. A simple schematic of a grating based stretcher is shown in the top Fig. 3.6. Using other

optical elements, the blue or short wavelength component can be sent on a longer path length through the stretcher, while the red or long wavelength components have a short path length. Once the pulse is stretched in time, the laser system picks one pulse from the 80MHz train coming from the Ti Sapphire oscillator using a Pockels cell. That pulse becomes a seed pulse for the regenerative amplifier. The regenerative amplifier is another Ti:sapphire crystal being pumped by an Nd:YLF

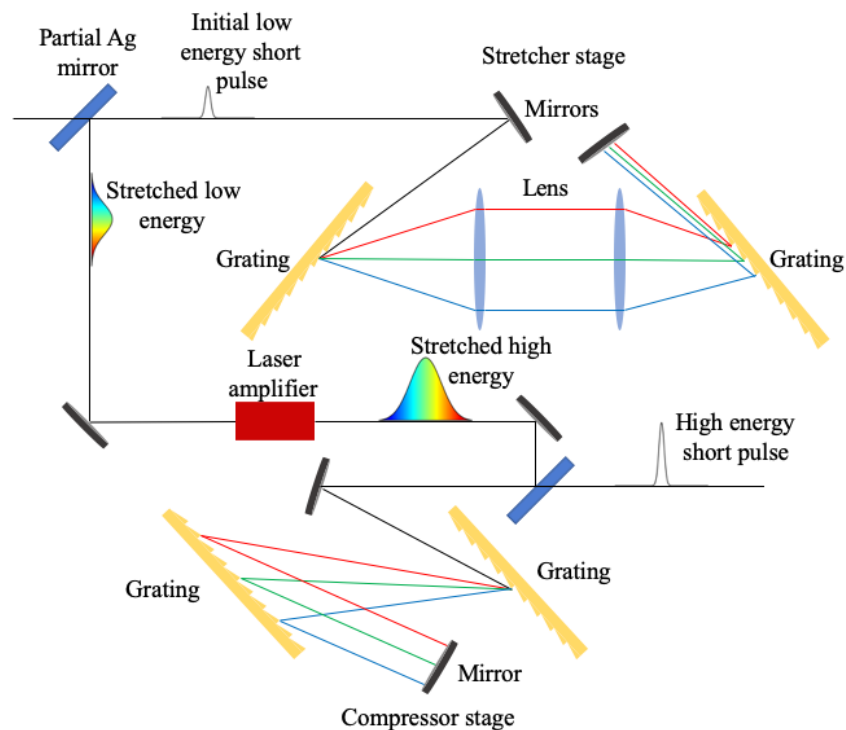


Figure. 3.6: A simple example of pulse chirp amplification with seed pulse and stretcher and compress stages along with the gain media. The seed pulse goes into the stretcher. Increasing the pulse duration will lower the peak power of the pulse which is represented as the lower amplitude rainbow gaussian. This lower peak power pulse will interact with the gain media to increase the amplitude and has low enough starting amplitude to not damage the amplifier's gain media. After amplification the stretched light pulse goes into the compressor stage which decreases the pulse width while the peak power will be increased. Reproduced from [85].

laser. The seed pulse makes many passes inside the cavity, picking up energy with each pass through the Ti:sapphire crystal. Typically, the energy amplification of each pass is 3-4 times, but over many passes through the crystal the amplification of 10^6 can be obtained [86]. At the last stage the amplified pulse has to be compressed back down to 150 fs. This is achieved by using gratings again but now the set up sends the blue/shorter wavelengths on shorter pathlength and the red wavelengths on a longer path. After the compressor stage the pulse now has 1mJ of energy in about 150 fs time after the compression stage. Fig. 3.6 shows both the stretcher and compressor grating systems of a chirp pulse amplifying system.

Because the pulse is Gaussian in nature, its peak power can be approximated [88] with the following equation:

$$P_p \approx 0.94 \frac{E_p}{\tau_p}. \quad (3.10)$$

In this equation, the τ_p is the full width at half maximum of the pulse duration and E_p is the energy of the pulse. The regenerative amplifier has a peak power of 6.3 gigawatts. That equates to $4 \cdot 10^{15}$ photons at an energy of 1.55 eV in each laser pulse.

The relationship that exists between laser pulse width and optical bandwidth [88] is:

$$\Delta\nu\tau_p > 0.441 \quad (3.11)$$

where $\Delta\nu$ is the bandwidth and τ_p is the laser pulse width. For a laser pulse of 150 fs at 800nm wavelength the corresponding bandwidth is ~ 6.3 nm. With 800 nm light gaussian pulses that are transform-limited, the optical bandwidth is 2.93 THz.

3.2.2 Nonlinear Generation of 3.1eV Light

In many experiments the 1.55eV light ultrafast laser output is used for both the pump and probe in ultrafast measurements. In these experiments, the UV light was used as a pump, produced by doubling the 1.55 eV. Frequency doubling was accomplished using a nonlinear crystal, a 0.3mm-thick β -barium borate crystal (more commonly known as a BBO crystal). BBO crystals lack inversion symmetry, and thus possess large second order χ_2 nonlinearity, making them an ideal nonlinear material for second harmonic generation [89]. This was seen from the \mathbf{E} polarization vector with the non-linearity term included. The BBO material polarization vector is defined as

$$\mathbf{P} = \chi\epsilon_0\mathbf{E} \quad (3.12)$$

By expanding the function in non-linear terms of χ and higher powers of the \mathbf{E} field:

$$P = \epsilon_0(\chi_1 E + \chi_2 E^2 + \chi_3 E^3 + \dots) \quad (3.13)$$

If the second order term is expanded out by putting in the \mathbf{E} field, using the expression

$$E = E_0 e^{-i\omega t} + E_0^* e^{i\omega t} \quad (3.14)$$

The polarization term P_2 becomes

$$P_2 = 2\varepsilon_0\chi_2 E^* E + \varepsilon_0\chi_2 E^2 e^{-i(2\omega)t} + \varepsilon_0\chi_2 (E^*)^2 e^{i(2\omega)t}, \quad (3.15)$$

where the first term is a DC electric field response and is often called the optical rectification. The second terms describes the response of the medium at the frequency 2ω leading to generation of frequencies that are exactly twice the input frequency [85]. The high \mathbf{E} field of short intense ultrafast pulses helps maximize the generation of the second harmonics light.

3.2.3 Pump Probe Experimental Setup

Short intense laser pulses, described in the previous section, are useful for measuring photo induced IMT dynamics in VO₂. The issue is how to record the fast IMT dynamics that occurs in ranges of the 100s of fs to ns. Most detectors are not fast enough to correctly measure these pulses properly. A PIN or high-end commercial photodetector is limited in its ability to detect short time signals, as electronic bandwidth is limited to a few GHz in [90]. One solution is to split a laser beam into two beams; the stronger powered pump pulse is used to induced changes in the material and the weaker energy probe pulse arrives after a controllable time delay after the stronger pump pulse has reached the material being tested. The pump pulse is energetic enough to modify the material's optical properties. The probe pulse is much weaker and is used to measure the material's

evolving state at a very short instance after the pump pulse initiates the material's optical modification.

With this system, simpler, lower bandwidth photodiodes can be used. This pump probe technique is similar to what Topley introduced in 1867 using light sparks of 2ms and a schlieren method [91].

The figure (3.7) illustrates a simplified depiction of the experimental apparatus just described. The laser output was split into two beams using an 80/20 Beam Splitter.

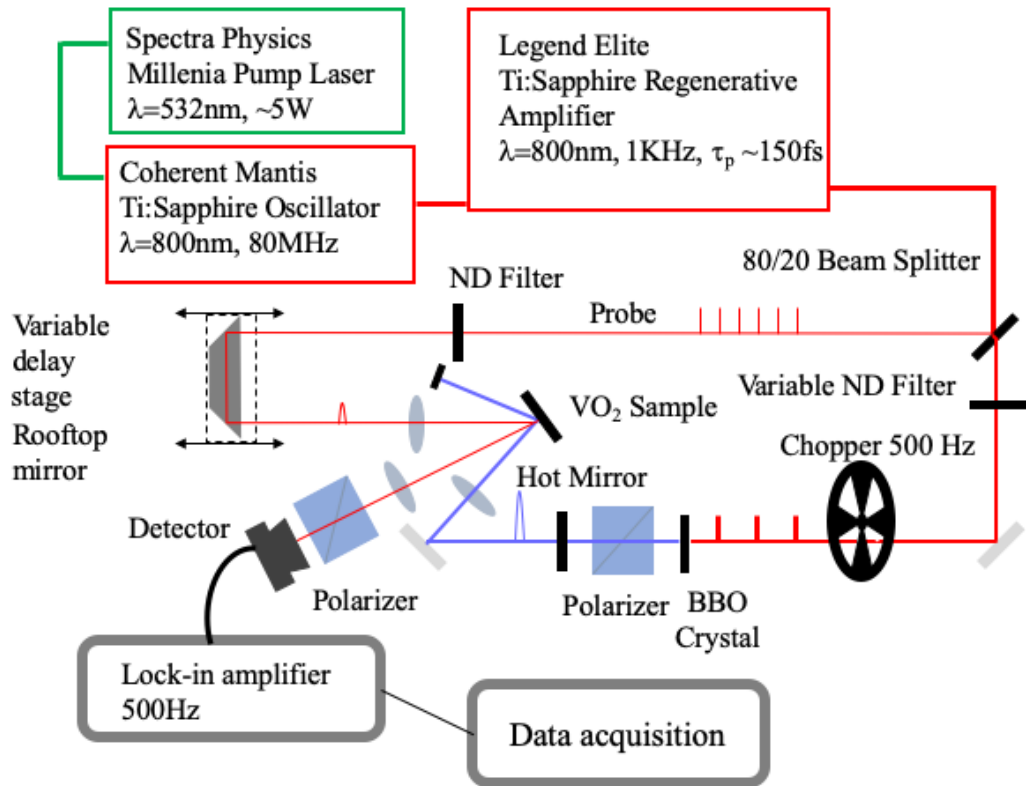


Figure. 3.7: Simple graphic of the pump probe experimental set up.

beam splitter, and the more powerful beam was doubled to 3.10 eV (400 nm) using a 0.3mm-thick β -barium borate crystal. A combination polarizer and hot mirror efficiently removed any residual 1.55eV light from the pump line to a maximum level of 100 nJ/cm², an order of magnitude lower than the probe line fluence which was verified by scattering small portion of the pump light into a fiber spectrometer. The weaker 800nm beam, serving as a probe, was redirected to a delay line that introduced an adjustable delay up to 4ns between probe and pump pulses. The delay line made stable steps of controllable size over a range of 600 mm. The minimum step size is 1.25 μ m which corresponds to an 8 fs time delay. For some measurements, the step size was adjusted during the scan to record fast early features using shorter delay steps and later slower features using longer delay steps. The powers of both beams were further adjusted using neutral density filters. The probe beam was kept at a fluence of 4.3 μ J/cm² for all measurements, significantly below the IMT threshold of 100 μ J/cm² for the 1.55eV photon energy for these samples. Because the pump and probe are cross polarized, a polarizer was used in front of the photodetector to help remove any additional residual pump signal scattered from the sample into the probe beam line.

3.2.4 Pump Probe Signal Analysis

When the pump pulse interacted with the sample, it induced dynamics by flooding the conduction band of VO₂ with photo electrons from the valence band.

With this non-equilibrium state of VO₂, the VO₂ will start its IMT transition, displaying changes to optical properties. For the pump probe measurements here, all of the changes measured from the probe were in the format of $\Delta R/R$ where $\Delta R/R$ is defined as $\frac{R_o - R_\tau}{R_o}$. R_o is the measured reflectance without excitation and R_τ is the measured reflection a short delay time, τ , after the pumped sample is excited. This is shown schematically in figure 3.8.

A silicon photodetector was used to convert the probe reflectance signal to a voltage. A lock-in amplifier which provided gain and noise suppression was used to measure both the $R_o - R_\tau$ and R_o terms. The laser system was triggered at a

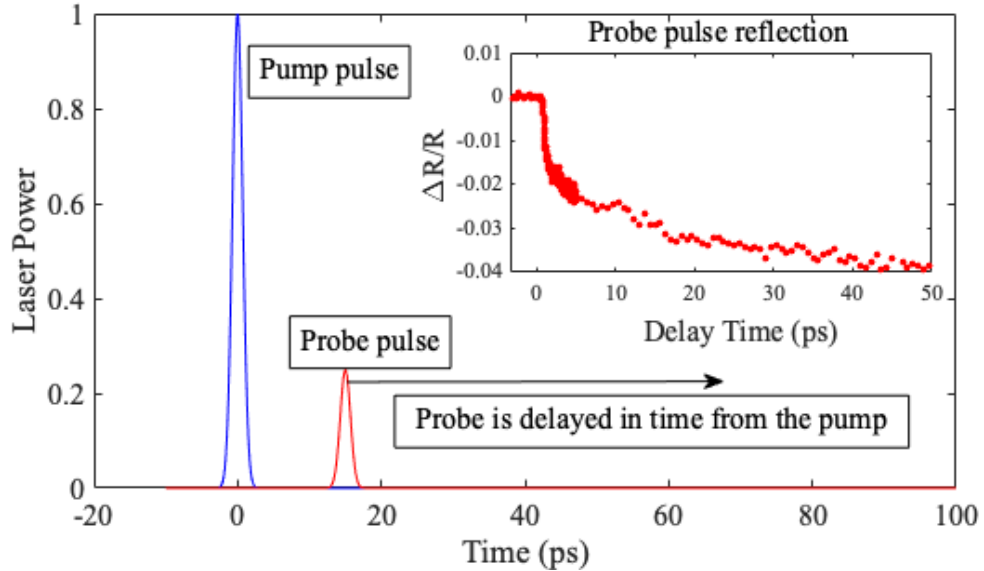


Figure. 3.8: Simple graphic of the timing sequence of the pump probe measurement system, where the time delay of the probe pulse is generated by a variable spatial delay line. The inset shows the $\Delta R/R$ data that was generated in a typical VO₂ thin film sample.

one kHz rate. To measure the R_o signal, the lock-in amplifier's reference frequency was set at 1kHz and the pump signal was completely blocked so that the reference signal is the surface reflectance without any excitation. To measure the $R_o - R_\tau$ signal, a 50% duty cycle optical chopper was operated in the pump line at 500Hz, which was synced to the 1kHz laser timing signal. This rejected every other pump pulse. The lock in reference frequency was also 500Hz. This provided alternating R_o signals without a pump and R_τ with a pump excitation into the lock-in input. In the lock-in at the reference frequency of 500Hz this had the mathematical effect of subtracting alternating signals, provided a signal that represented the $R_o - R_\tau$ directly as an output.

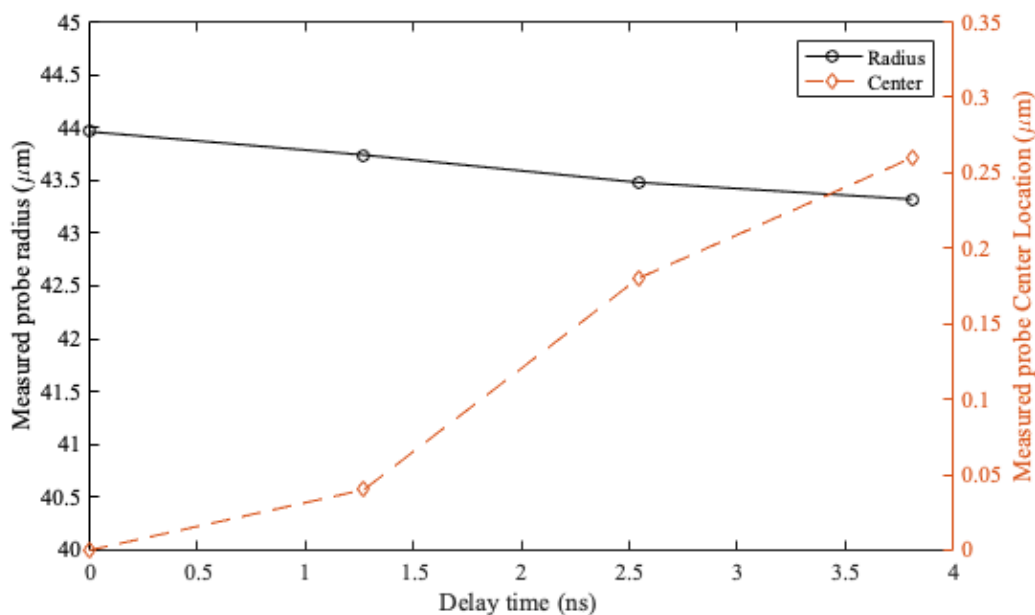


Figure. 3.9: Vertical beam radius and location measurements from knife edge. Black line is the radius of the beam at the sample location and red is the beam center location of the probe.

Pump probe experiments rely on beams being perfectly co-located on the sample. Several knife edge measurements were performed on the probe beam's profile at different delay locations using the "90%-10% knife edge" method to verify that the probe beam's position and size were stable with translation of the delay stage. Figure 3.9 shows the vertical movement of the beam was small with the probe's center location only moving about 250nm throughout the whole 4ns of delay stage movement. The measured probe radius changed about 600nm over the whole delay. Both measurements showed that for the test measurements there was little movement of the probe beam affecting the accuracy of the pump probe measurements. Horizontal measurements had similar results. The knife edge measurement of the pump beam was done in the same way to determine its beam size.

Cross-polarized pump and probe beams were focused on the samples so that their diameters on the surface were centered on each other. The pump and probe beam diameters were $\sim 130\mu\text{m}$ and $\sim 70\mu\text{m}$ respectively. The smaller probe size ensured that the probed region was sampled across a uniformly pumped area. Fluence of the beam was calculated using the diameter derived from the beam waist, ω_0 , measurement and the rep rate of the laser and laser power in the following equation:

$$Fluence = \frac{Power}{Rep\ rate * \pi \omega_0^2} \quad (3.16)$$

3.3 Photocurrent Speed Measurement

VO₂ on TiO₂:Nb samples showed photocurrent production with external quantum efficiency (EQE) by Creeden [79], but these measurements lacked temporal resolution of 10's of Hz because of the use of slow bandwidth instruments with high sensitivity. For the measurements here, faster time rates were investigated.

A modified Van der Pauw set up was used for the measurement of photocurrent rates. Four copper beryllium pins contacted the sample. A 405nm diode laser, generated up to 7mW of CW power, was used. An optical chopper was used to generate 50% duty cycle square pulses to modulate the laser and have a timing reference. The photocurrent signal generated by the VO₂ on TiO₂:Nb sample was amplified with a current amplifier and recorded with an oscilloscope. Three signals were taken; (1) light “on” case generating photocurrent in the sample, (2) light “off”, to measure the noise and dark current level, and (3) a “pickoff” signal was also taken for a timing reference. The data was fitted to extract the exponential time constants.

3.4 Ellipsometry

Ellipsometry on VO₂ samples was completed in Professor Qazilbash's lab using a J.A. Woollam Co. Inc. V-VASE ellipsometer. Both metallic and insulating states were investigated to obtain the optical properties of the VO₂ samples. Samples were heated via thermal stage to achieve the metallic state. The ellipsometry

measurements were taken from 0.5 eV to 4 eV in photon energy for the insulator and metallic states of VO₂. The sample's response to the probe light was fitted using the WVASE software. Appendix A has an explanation of the data processing.

CHAPTER 4

Samples and Sample Characterization

4.1 Characterization Methods

Characterization methods were performed to ensure that VO₂ existed along with determining surface morphology, the optical properties, and thermal metal to insulator characterization.

XRD, X-Ray Diffraction, provides information about the structure of a sample. The basis of XRD is that x-rays scatter off the lattice ions of a solid sample. Because of the regular lattice periodicity, the x-rays Bragg scattering forms characteristic diffraction patterns [39]. This allows lattice structure reconstruction. For the x-ray to interfere constructively, the Bragg formula describes the condition:

$$n\lambda = 2d \sin \theta, \quad (4.1)$$

where n is an integer, and λ is the wavelength of x-rays, and d is the distance between the ions centers and θ is the Bragg angle. The measurements of the diffraction peaks provide the lattice structure, identifying the molecules, such as VO₂. Fig. 4.1 depicts an x-ray diffraction configuration on the lattice.

Atomic force microscopy (AFM) is a powerful tool used to study the surface of a sample and can give topographic information of the surface. It is based on a scanning probe microscope which uses a cantilever with a sharp tip that interacts with the surface of the sample via the van der Waals forces [92]. The cantilever deflection is usually tracked by a laser, and translates the amount of deflection of the cantilever to surface profile [93].

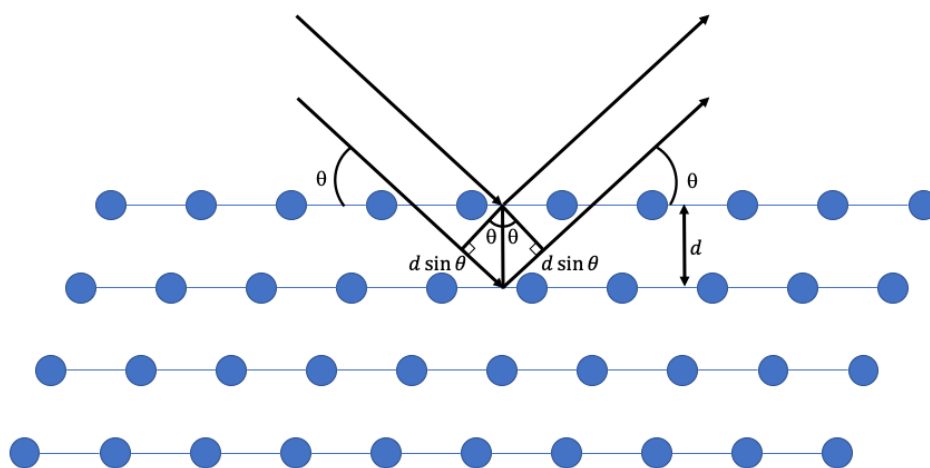


Figure. 4.1 Shows a simple Bragg reflection off a periodic lattice represented by the blue circles with a lattice spacing of d and the source beam at an incident angle θ . The path difference between the incident and reflected rays off adjacent lattice planes will be $2d \sin \theta$. Reproduced from [39].

Optical properties were measured by Ellipsometry. Appendix A provides a theoretical background for ellipsometry and Section 3.4 discuss the measurements of the VO_2 sample.

4.2 Samples for Pump Probe Ultrafast and Photocurrent Tests

4.2.1 Sample Manufacturing Background

Samples used in the ultrafast study and photocurrent test were grown at W&M with a lower energy process of reactive pulsed magnetron sputtering [78, 79]. This was the basis of a research project done at the same time as the ultrafast pump probe work. The W&M samples were grown on two different substrate types: TiO_2 and $\text{TiO}_2\text{:Nb}$. The $\text{TiO}_2\text{:Nb}$ was bulk doped at 5% by weight. Both of the TiO_2 substrates had the same crystal orientation of (001). For the TiO_2 30 nm and 50 nm thickness samples were grown. $\text{TiO}_2\text{:Nb}$ samples of thicknesses 15 nm, 22 nm, 30 nm, and 50 nm were grown.

4.2.2 Crystal Characterization

Details of the sample's structure and chemistry were measured by Creeden [78, 79, 94]. Fig. 4.2 and Fig. 4.2 indicate growth of the VO_2 on the TiO_2 substrates used for the photo induced IMT and photocurrent measurements. The crystal

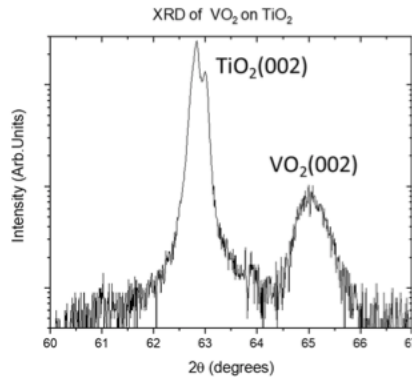


Figure. 4.2: XRD of the 30nm VO_2 on TiO_2 from [78] showing the presence of VO_2 and TiO_2 and their respective crystal orientations.

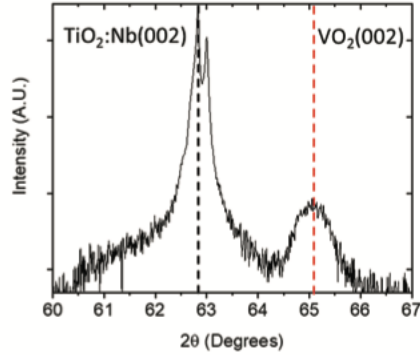


Figure. 4.3: XRD of the 30nm VO₂ on TiO₂:Nb from [79] showing the presence of VO₂ and TiO₂ and their respective crystal orientations.

orientation for the VO₂ was (002). The TiO₂ substrate was one-side polished and TiO₂:Nb was dual-side polished. Both samples measured showed a high degree of uniformity, with single crystal orientation as measured in the XRD images from the samples reported in [78, 79, 94].

4.2.3 Surface Morphology Characterization

The surface profiles from AFM for the 30nm VO₂ on TiO₂ and on TiO₂:Nb are shown in Fig 4.4. This figure showed some differences that were considered insignificant in regard to the roughness. Both VO₂ thin film samples used were approximately 30nm thick. AFM studies showed the VO₂ on TiO₂ had 18.8 nm RMS roughness from the 5x5 μm scan and the VO₂ on TiO₂:Nb has 15.5 nm RMS for the 5x5 μm scan (Fig. 4.4).

4.2.4 Ellipsometry on the VO₂ on TiO₂

Substrate choices [95], interface strains, and growth processes can influence the optical properties of individual VO₂ thin films. Accurate optical properties of our samples were obtained by ellipsometry in the spectral range from 0.6 to 4.0 eV.

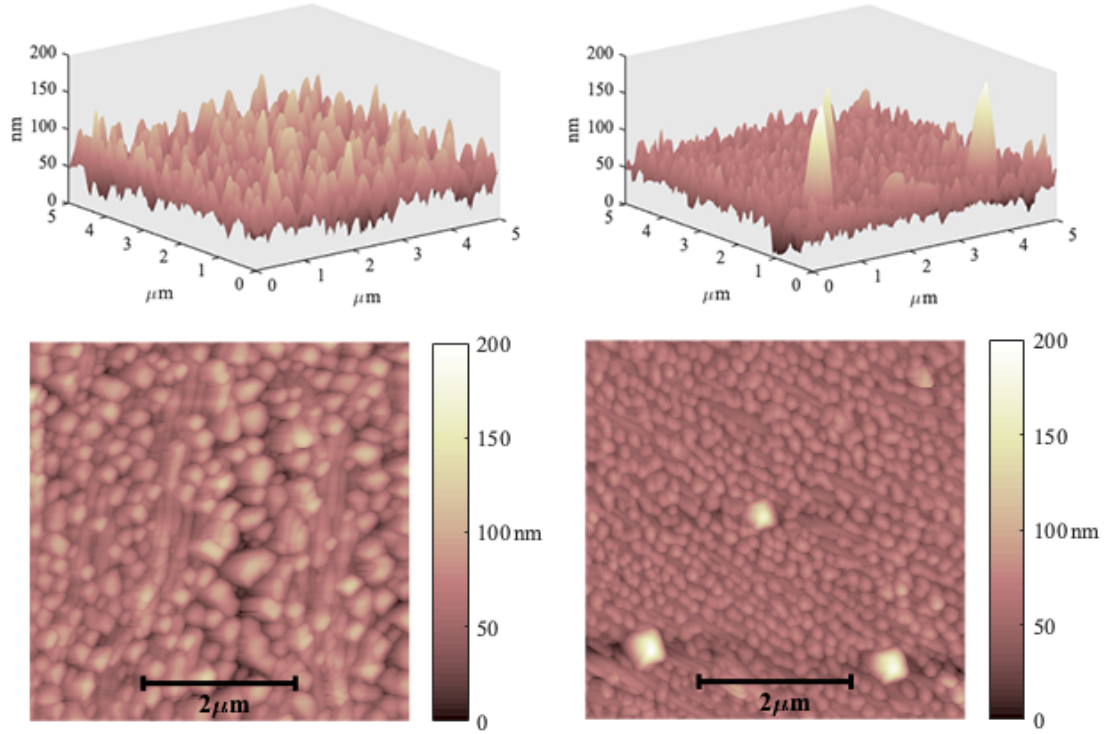


Figure. 4.4: AFM scans of the two-sample used for this experiment. Left are 30nm VO₂ on TiO₂ with 18.8nm RMS roughness. Right is 30nm VO₂ on TiO₂:Nb with 15.5nm RMS roughness. Top images are 3D and bottom are 2D. From [79,94].

The WVASE program fitted optical properties using Tauc-Lorentz oscillators [96] and is discussed in Appendix A. The sample was measured in the insulating state and then in the metallic state after heating above the IMT critical temperature. The calculated optical properties also incorporated surface roughness effects, measured by AFM (Fig. 4.4) for the VO₂ on TiO₂ sample. It was assumed that the

first 10nm of the VO₂ layer had grown with low surface roughness, and subsequently roughened during further growth (Fig. 4.4) [94]. Data was fitted as a 10 nm smooth layer below an effective medium layer representation for the roughness for both the insulating and metallic states.

The dielectric functions obtained from ellipsometry in the insulating state and the metallic state are shown (Fig. 4.5a and b) and help explain the sample's response to pump-probe excitation. Fig. 4.5b shows according to the Tauc-Lorentz oscillator (TLO) model, ϵ_2 , the insulator state (blue lines) exhibits a large low energy band centered around 0.8 eV that has a low energy gap of about 0.2 eV. The three TLOs for the insulating state of VO₂ are shown for both ϵ_1 and ϵ_2 (Fig. 4.5). The second bump at 2.75 eV, shown as a dotted blue light, results from two

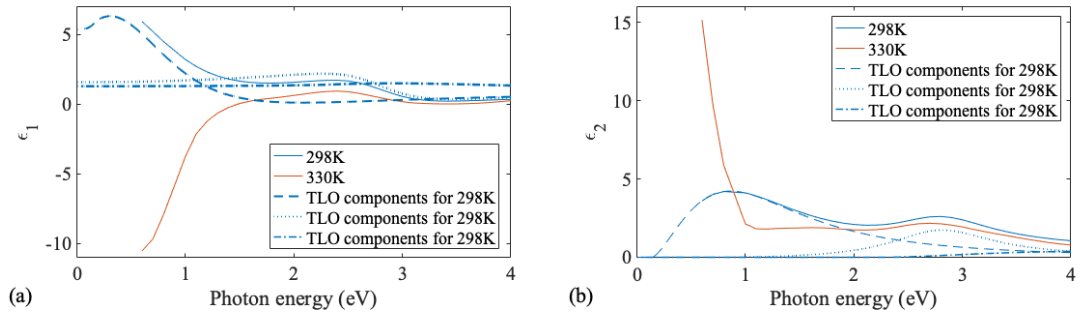


Figure. 4.5: Dielectric function ϵ of 30nm VO₂ on TiO₂. Graph (a) is the real component of ϵ and graph (b) is the imaginary component of ϵ . The blue line represents the insulating state and the red line represents the metallic state. The dashed blue lines are the components of the Tauc-Lorentz oscillators that make up the real and imaginary component of ϵ in the insulating state.

higher overlapping energy bands. Hence, 3.1 eV pump energy can excite electrons

from the valence band into all three of these energy bands, while the lower 1.55 eV probe energy can only excite electrons into the lower energy band.

ϵ_2 increases at low photon energies for the metallic state (red lines), consistent with the collapse of the band gap and the emergence of free carriers. Further evidence of the metallic state is seen in negative values of ϵ_1 for the low photon energy range of the curve. At around 1.5 eV, photon energy, the dielectric functions for the two states have a larger magnitude difference than what is seen for the pump photon energy. Measuring at 1.55 eV indicates differences in ϵ_1 and ϵ_2 between the two states will be more sensitive at 1.55 eV than 3.1 eV.

The optical properties of the insulating and metallic states at 1.5 eV and 3 eV are summarized in Table 4.1. n and k represent the real and imaginary components of the index of refraction, ϵ_1 and ϵ_2 represent the real and imaginary parts of the dielectric function, and δ is the optical penetration depth.

Table 4.1. Optical properties of VO₂ on TiO₂

State	Photon energy (eV)	n	k	ϵ_1	ϵ_2	δ (nm)
Insulating	3.0	1.22	0.98	0.55	2.39	32.6
	1.5	1.58	0.92	1.65	2.90	69.4
Metallic	3.0	1.03	0.94	0.18	1.94	33.8
	1.5	0.98	0.96	0.04	1.87	66.5

4.2.5 Thermal IMT of the VO₂ on TiO₂ Sample

Temperature dependence of the optical reflection for 700 nm and 400 nm light was measured to characterize the thermal IMT properties of a 30 nm VO₂ on TiO₂ sample under thermal excitation (Fig. 4.6). The incoherent light source used for this measurement did not reach 800nm, so the longest wavelength available, 700 nm, was used. The thermal transition behavior was sufficient to verify the accuracy of numerical modeling. As expected, a reduction in reflectivity as the sample underwent thermal transition was observed. Both measurements showed that the transition occurred at 50 ± 5 °C. The lower transition temperature seen for this sample was expected due to the strain that the TiO₂ substrate imparts on to the VO₂ film [12, 97]. $\Delta R/R$ is the relative change in the sample reflectance over its base reflectance in the VO₂ insulator state. Negative value of $\Delta R/R$ showed the reduction of reflectance as the sample transitioned into the metallic state. The larger $\Delta R/R$ change between the two VO₂ states compared to the photoinduced transition measurements, arose from the larger incidence angle (45°) used for this measurement. Interestingly, the 400 nm light reflectivity exhibited a suppressed thermal hysteresis (i.e. the difference in the curves for heating and cooling cycle were smaller) that is clearly observed in 700 nm measurements. In fact, repeated measurements at varying wavelengths of the optical probe showed a complete

collapse of hysteresis below 400 nm, while the hysteresis was clearly observed for longer wavelengths, and its width was constant above 500nm.

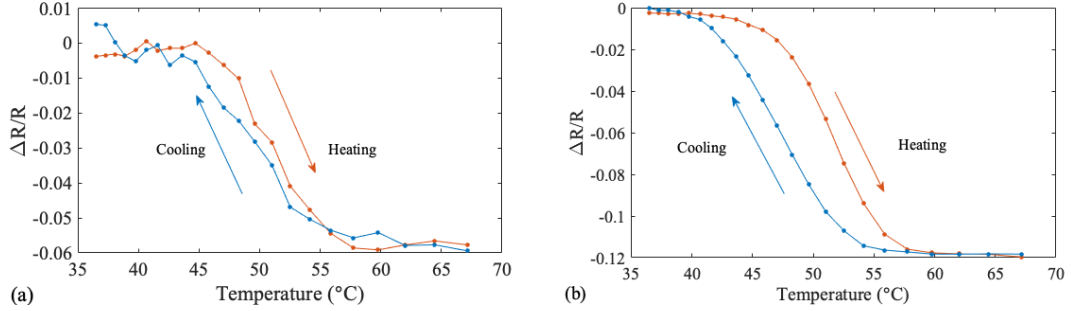


Figure. 4.6: Characterization of the thermally induced IMT of the VO₂ on TiO₂ film using the reflectivity of (a) 400nm and (b) 700nm incoherent light. The red dots indicate the measurements taken while heating the sample, while the blue dots correspond to the cooling.

4.3 Au-VO₂ Sample for SPR Experiments

4.3.1 SPR Sample Design and Manufacture

The sample used in this study was grown on plain soda lime glass substrate in two stages. A layer of 31nm of Au was deposited by evaporative deposition on the glass substrate. Next, a 5nm VO₂ layer was deposited via reactive biased target ion beam deposition onto the Au layer, which was been described by West [98]. Both Au and Ag are adequate metallic layers for our proposed structure because of their excellent dielectric properties for SPP generation at 1064nm [99]. However, Ag quickly oxidized during the growth process for the VO₂ layer. Thus, the more stable Au was chosen for the base metal layer. The thickness of the VO₂ layer was chosen such that the SPP electric field was expected to be fairly uniform across the full

VO₂ thickness.

The exact thickness and composition of the sample was designed using a 4×4 optical matrix formalism that was described in [100] and implemented in Mathematica[©] code. Simulations were carried out for various thicknesses of the Au layer to establish the largest absorption and the narrowest full width at half max (FWHM) resonance for the SPP resonant curve. VO₂ was included in the simulations to predict the optimum Au and VO₂ layer thicknesses for a strong SPR response for the sample. The overall goal was to obtain a sensitive SPR response [80], corresponding to the strongest E-field enhancement at the Au surface. That determined that 31nm Au with 5nm VO₂ was optimal for 1064nm light. The optical susceptibility values used for the simulation were: for Au: $\epsilon' = -48.480$, $\epsilon'' = 3.6006$ [99], for insulating bulk VO₂: $\epsilon' = 9.56$, $\epsilon'' = 2.81$, and for metallic bulk VO₂: $\epsilon' = -1.71$, $\epsilon'' = 5.97$ [4].

4.3.2 SPR Sample Characterization

AFM images were taken at UVA, as were XRD scans. The UVA Material Science Department has a long history of successfully manufacturing VO₂ samples using reactive biased target ion beam deposition [36, 49, 98, 101-104]. The sample used here had a rms surface roughness of 2.4 nm measured by colleagues at UVA. The AFM image of the sample can be seen below Fig 4.7 and was taken at UVA. The XRD showed that the VO₂ had grown with a crystal orientation of 011 as can be

seen in Figure 4.8 VO_2 grew as a polycrystalline sample, due to the sample being grown on amorphous glass.

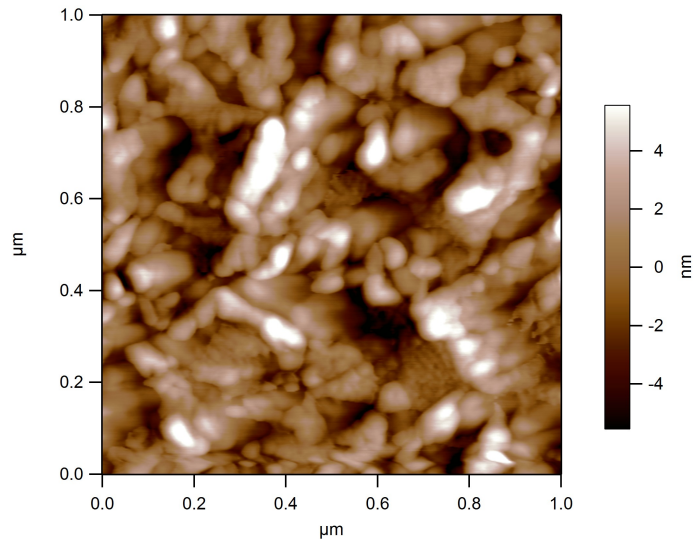


Figure. 4.7: AFM image done at UVA for 5nm of VO_2 over 31nm Au. The RMS roughness was 2.4nm.

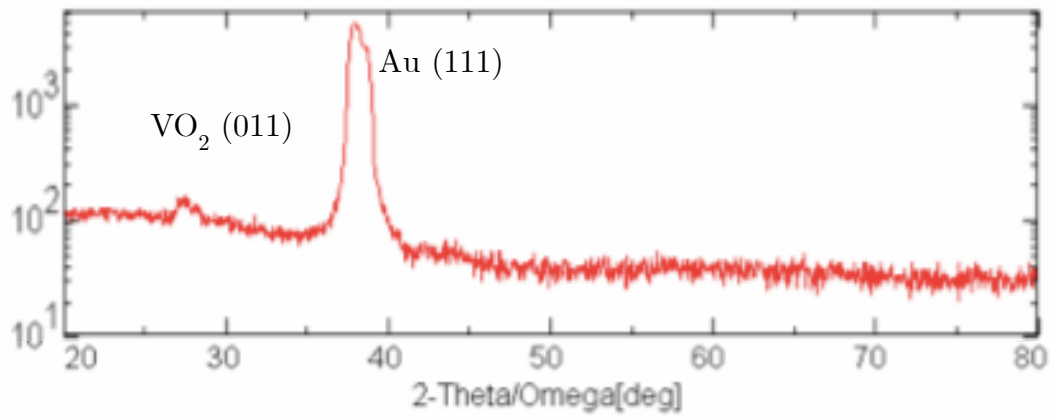


Figure 4.8: XRD of the 5nm of VO_2 over 31nm Au done by UVA the Au and VO_2 peaks are labeled on a 2-theta axis.

CHAPTER 5

Insulator to Metal Transition Induced by Surface Plasmon Polariton in VO₂/Au Thin Films

5.1 Introduction

This chapter reviews work which sought to induce and detect the insulator to metal transition in VO₂ using surface plasmons polaritons.

The approach utilized to both induce and detect the IMT in a 5-nm thin VO₂ layer was based on SPR, in which SPPs were excited at the VO₂ - gold interface over a narrow range of incident angles of a laser beam in the Kretschmann configuration. [80] At resonant conditions, the electric field at the interface of the Au-VO₂ was enhanced by a factor 16 times the incident E-field strength for our sample geometry, and reached threshold values for IMT in VO₂ with lower peak input laser powers compared to the direct excitation at room temperature by either standard or ultrafast optical pulses [18] or applied dc electric field [5, 105]. This experiment showed a clear change in the SPR nadir position similar to predictions

based on known VO₂ optical constants in the insulating and metallic states when laser power was increased above the threshold value of 5mW. An alternative method, such as thermally inducing the IMT to independently confirm the occurrence of IMT in the VO₂ layer was not applied because the observed SPR behavior was fully consistent with this expectation. Furthermore, heating of the glass would cause thermal expansion leading to a non-stable reflectance signal. The heating would also cause changes to the optical properties of the Au layer [106] leading to changes in the reflectance that are not due to the VO₂ IMT.

Experimental apparatus and background on SPR including E-field enhancement are discussed in section 3.1. Sample properties are presented in section 4.3. Modelling methods used to compute the E&M components of the SPR fields and reflection values are discussed in Appendix B.

5.2 Surface Plasmon Resonance IMT Studies in VO₂

5.2.1 SPR Modelling Response

A finite difference time domain (FDTD) calculation, EM Explorer[©] software was used, in addition to the use of a 4×4 optical matrix method to numerically model the optical response, which allowed extraction of the spatial distribution of the electric fields. Fig. 5.1(a) shows the sharp decrease in *p* polarized light reflectivity as the incident angle approaches the critical angle of total internal reflection. Both the 4×4 matrix method (shown as solid lines) and the FDTD calculations (shown

as dotted lines) agreed with each other in the estimation of the nadir location of the SPR for both fully insulating VO₂ properties (blue data lines) and fully metallic VO₂ properties (red data lines). They also clearly predict that the IMT in VO₂ must cause the nadir location of the SPR to shift to smaller angles. The narrowness of the SPP resonance helps revealing the shift in the SPR curve when the IMT occurred, which was one of the design parameters for the sample.

Figure 5.1(b) is a close-up of the central region of the SPR curve, highlighting the shift in the SPR nadir location by approximately 0.1° between the two material states of VO₂. The nadir location for the insulating state was at 42.3 degrees while the metallic state's nadir was 42.2 degrees. The same shift was predicted by both the 4×4 matrix method and in the FDTD model. Away from

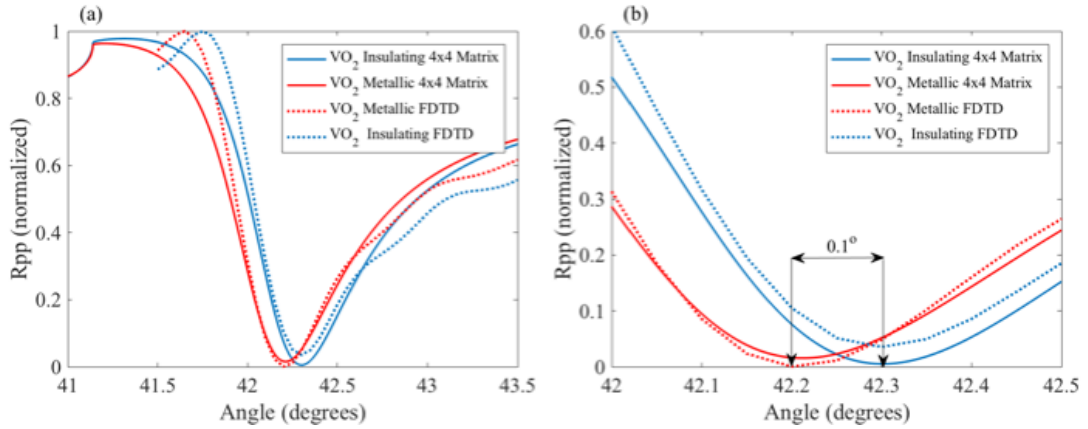


Figure. 5.1: (a) The reflection of the P polarized light (R_{pp}) from two different simulations methods; the (dotted) FDTD method the (solid) 4×4 optical matrix method. The blue lines are for the case when the VO₂ is in the insulating state and the red lines are for case of metallic VO₂. (b) close-up view of the nadir region of the SPR curve showing the nadir shift produced by the SPP-induced IMT in the VO₂.

the resonant points, the two methods showed small discrepancies from each other.

5.2.2 SPR VO₂ IMT Results

Figure 5.2 shows the normalized SPR reflectivity of p polarized light over a wide range of angles with the laser at low power (definitely below the IMT threshold) and at high power (above the projected IMT threshold). An angle step size of 0.04° was used for this data and the signals were normalized to the maximum signal measured at a 44.12° angle (which is not shown). Since maximum energy was transferred to SPP near the bottom of the reflectivity resonance, the effect on the IMT in that region when the laser power exceeds the necessary threshold was expected to show IMT behavior. Indeed, the two curves showed a clear separation at the resonant point highlighting that the IMT in this sample was in good agreement with our theoretical predictions of 0.1° change of the resonant point as indicated in Fig. 5.1(b) for a thin film VO₂ sample with this geometry. Both model calculations (Fig. 5.1) agreed, showing a consistent difference in nadir locations between the two material states of VO₂ (either fully insulator blue curves or metallic red curves) at all angles of the SPP. Fig. 5.2 only showed a difference near the SPP resonant point. Below 44.88° and above 45.5° the two curves converged and showed a reflectivity commensurate with an insulating VO₂ state, while between those two angles, the reflection better matched the metallic VO₂ for the 5.4 mW SPR curve and the insulating VO₂ better matched the 10 μ W SPR curve.

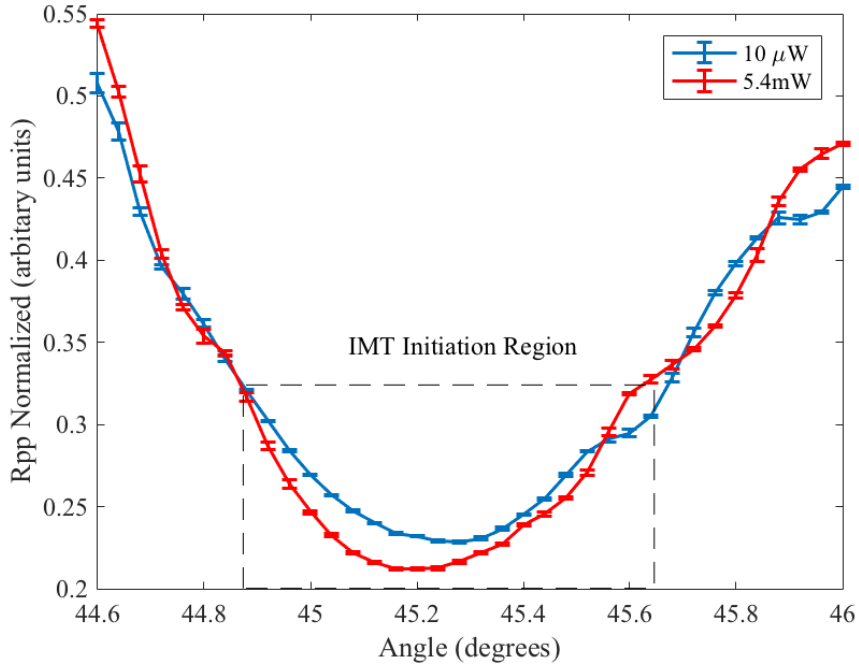


Figure. 5.2: SPR data for two power levels. The vertical axis is normalized Rpp. The horizontal axis is the incident angle in degrees. The blue curve is for $10\mu\text{W}$ power level scan. The red curve is for a 5.4mW scan. The dashed box highlights the region where the IMT differences are detectable between the two power levels.

The 44.88° angle was 0.35° below the resonant angle for the insulator state of VO_2 . When VO_2 was irradiated at 5.4 mW laser power, the angle of the incident beam moved off resonance and SPP generation decreased with a corresponding decrease in the electromagnetic energy density. Outside the IMT initiation region shown by the dashed box in Fig. 5.2, the electric field enhancement at the Au- VO_2 interface is weaker and VO_2 exhibits the behavior of the insulating phase.

Figure 5.3 focuses into the experimental measurements for the SPR reflectance over a very narrow angle range using a smaller angular step size of $.016^\circ$

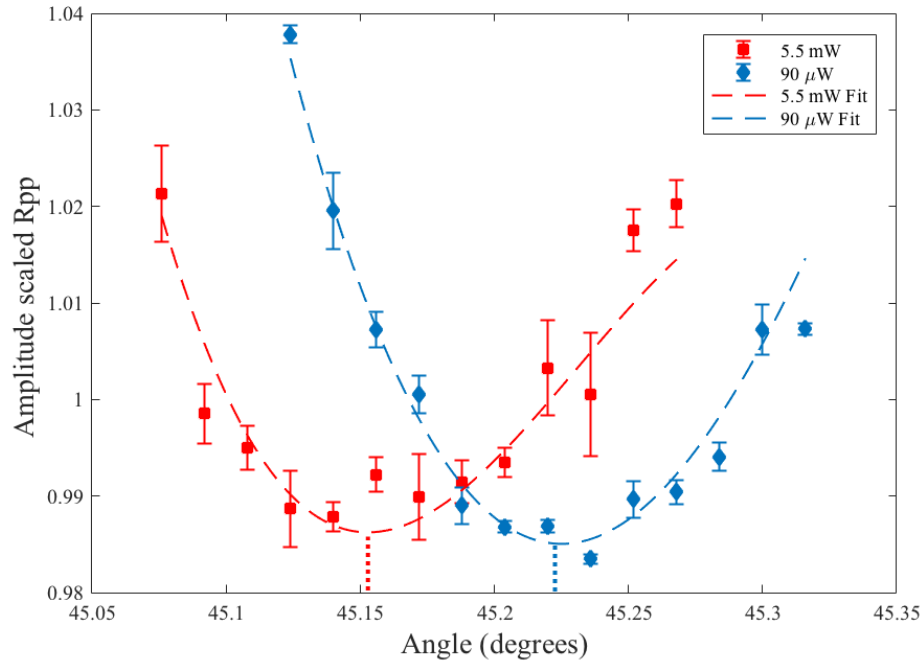


Figure. 5.3: The SPR response curve of two different laser power scans on the sample. The blue diamonds show the data points for the 90 μ W power scan with uncertainty. The red squares show the data points for the 5.5mW power scan with uncertainty. The dashed blue line is the corresponding weighted polynomial for the 90 μ W scan. The dashed red line is the corresponding weighted polynomial for the 5.5mW scan. The dotted vertical blue and red lines are visual guides for the respective nadir locations for the polynomial fit.

for better resolution of the nadir. Each data set was normalized by their averaged signal amplitudes. This resulted in rescaling of data onto the same amplitude range for easier visual comparison of the nadir locations. In this case, the vertical scale was denoted as “Amplitude scale Rpp” instead of the “Rpp Normalized” used in Fig. 5.3. There was a clear angular shift in the SPR nadir point of approximately 0.07° , which is 70% of the model’s prediction. A weighted polynomial fit was used to determine the precise angle of the nadir location for each laser power. It provided

a minimum location and a value for the confidence interval for the quality of the data. The short vertical dotted lines in Fig. 5.3 indicates the fit's angle for the nadir locations of the two laser power levels examined in Fig. 5.3.

Figure 5.4 shows experimental results for the VO₂ SPR nadir's location shifts vs. the laser power input. Despite relatively low signal to noise, the change in the SPR minimum position above a certain laser power was clear. At low laser power the nadir's location was stable. The threshold for the onset of the transition occurred at 2mW and further increase in laser power caused the nadir position to shift toward a lower angle. At approximately 5mW power level the nadir position reached saturation and the angle was no longer changing.

The inset in Fig. 5.4 shows measurements of the SPR's nadir location variation measured in the same manner, but on a plain layer of 31nm Au on glass without VO₂ to verify that the observed behavior cannot be attributed to a change in the optical properties of the gold layer. In contrast to the Au/VO₂ sample, the pure Au sample's SPR nadir value was unchanged over the tested power range.

Indeed, heating of the Au layer can also induce changes to the Au optical properties [106], causing the resonant nadir point to shift to higher angles at higher temperatures, as opposed to the VO₂ layer, which shifted the nadir to lower angles when it went through an IMT. However, the temperature-dependent changes in the Au layer made it hard to reliably detect changes in VO₂ layer optical properties

for a thermally induced IMT attempt.

Fig. 5.4 shows the relative magnitude change of the expected shift of the nadir's location from the simulation which was also plotted in the figure as black dashed lines for zero, 50% and 100% of metallic VO₂. The data approximated the magnitude of the shift predicted by the simulation, especially since the

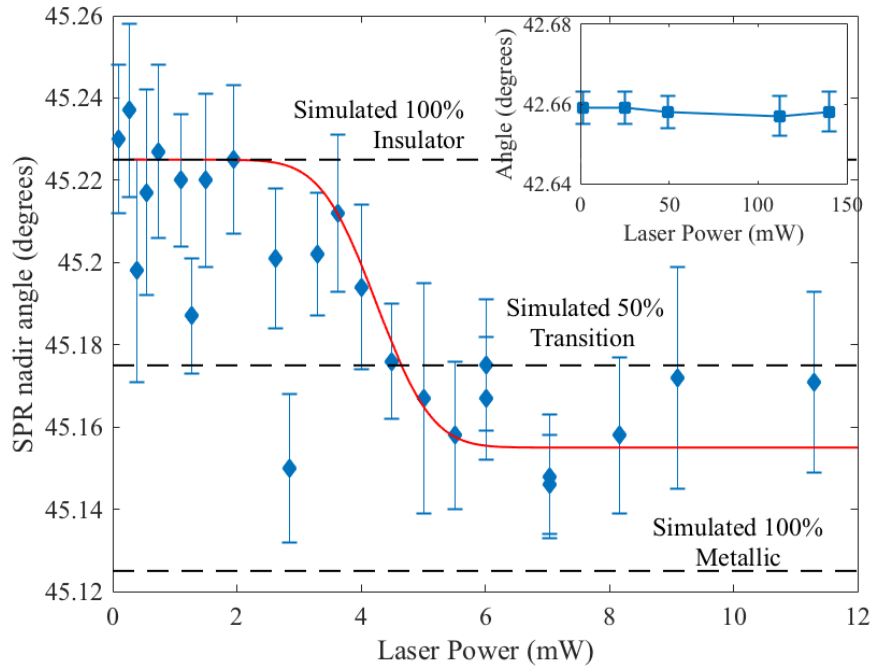


Figure. 5.4: Shows the SPR nadir locations versus the laser light power level. The dashed lines represent the simulation values for 100% insulating VO₂, 50% metallic/50% insulating VO₂, and 100% metallic VO₂. The red line is a visual guide for the transition behavior. The insert displays the SPR nadir locations for the bare 31nm-thick film of Au. For small scans in the vicinity of the resonant points, the data was fitted with a polynomial function. The weighted polynomial was a 3rd order polynomial and the minimum of the polynomial determined the nadir location for that power level scan. The uncertainty in amplitude of the fit at the nadir location was used to determine the uncertainty in the angular location.

susceptibility values for bulk VO₂ were used in simulations and these values might not be identical to those in thin films. The relative nadir shift is evidence of a significant change in the optical properties of VO₂. Its magnitude suggested that this was due to IMT, as predicted by simulations. Independent measurements of the optical properties of this thin film sample of VO₂ have not been carried out because of concerns regarding possible sample damage caused by thermal cycling. Under these considerations, the observed discrepancy in the nadir shift between the measurements (0.07°) and the numerical modeling (0.1°) was reasonably small.

Measurement of the IMT of VO₂ raised the question of the possibility that the observed effect could be caused by an increased temperature due to heating by the laser beam. A thermal FLIR camera was employed to address this issue in the measurement system as shown in Fig. 3.4. The FLIR camera would detect temperature changes with 0.1° accuracy. At the optical power levels used in these tests, no thermal increase was detected either in the VO₂ layer or in the polycrystalline Au layer. Output images of the FLIR camera are shown in Fig. 5.5, with Fig. 5.5(a) having the laser on, Fig. 5.5(b) having the laser off, and Fig. 5.5(c) subtracting panel (a) and (b). These images confirmed that the laser used did not raise the sample's temperature appreciably.

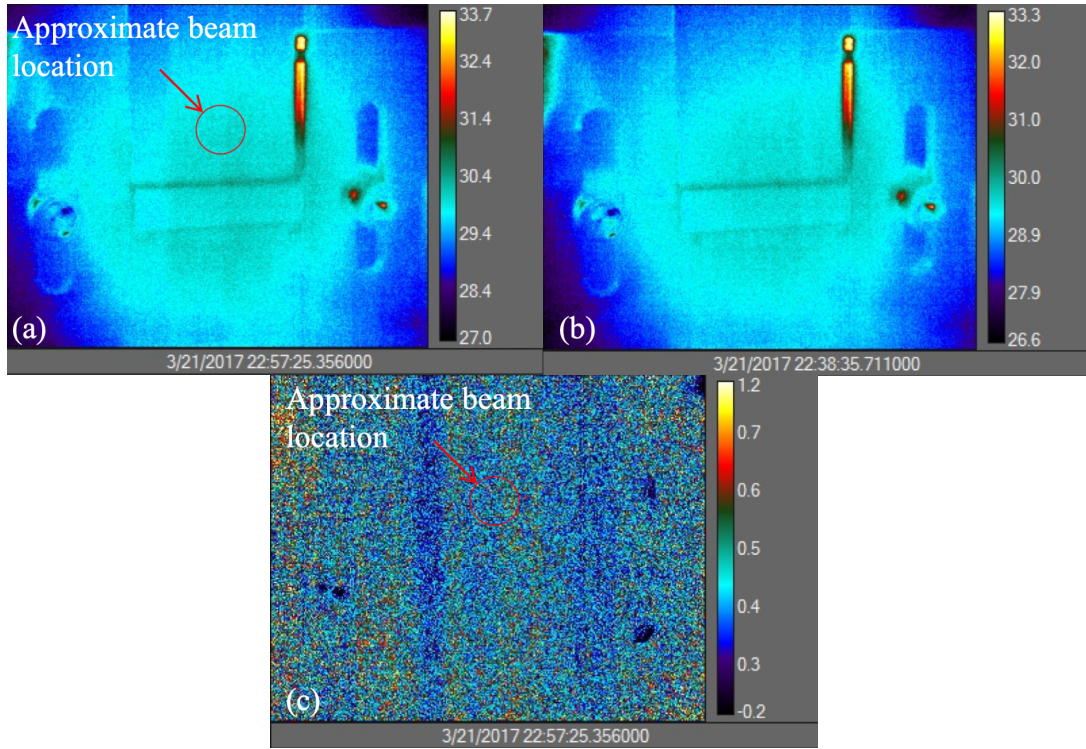


Figure. 5.5: FLIR image of the back of the sample with the SPR being a its nadir location for the metallic case of VO_2 the color gradient bar on the right is the temperature in $^{\circ}\text{C}$. Panel (a) is the laser power on (12.4mW) and the red circle shows the approximate location of the beam on the sample. Panel (b) is the case where there is no laser power incident on the sample. Panel (c) is the difference between the two panels (a)-(b) measurement and again the red circle is the approximate location where the energy was deposited.

5.2.3 E-Field Model Comparison with Data

The FDTD model and published optical properties [4, 99] were used to estimate the internal electric E_z or magnetic H_y field amplitude enhancement in the sample at the wavelength of 1064 nm. Figure 5.6 illustrates the FDTD output for the density of electromagnetic energy across the Au and VO_2 layers normalized to the incident EM wave at the nadir location for the insulating VO_2 of 42.3° and the

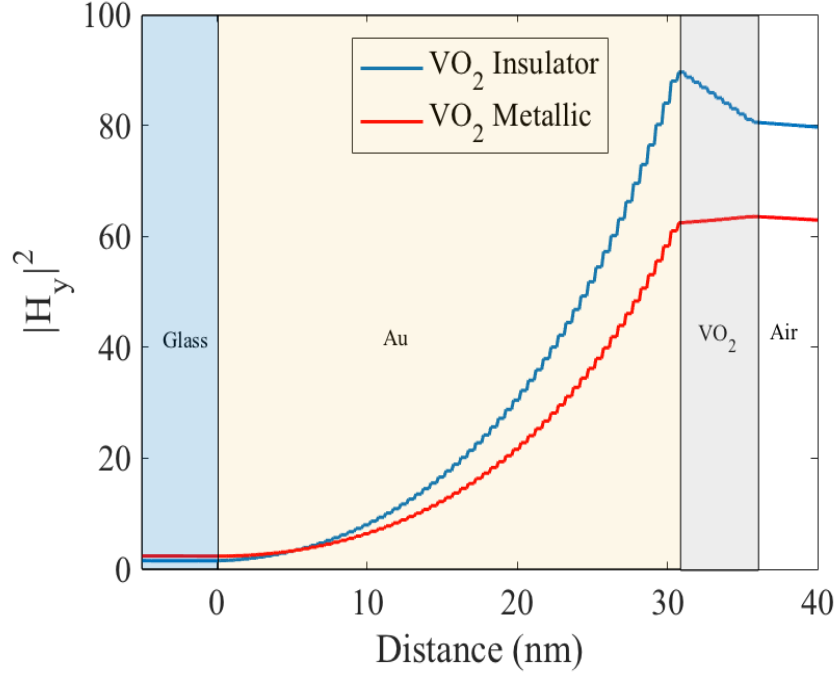


Figure 5.6: FDTD simulations for $|H_y|^2$ field in the sample for the case of Insulating VO_2 state (blue line) and metallic VO_2 (red line). $|H_y|^2$ is the density of the relative electromagnetic energy in the sample and shows the field enhancement caused by surface plasmons at the resonant point.

metallic VO_2 case of 42.2° . The cell size in the FDTD simulation was set to 0.5nm , as a compromise between the sufficient spatial resolution and the computational time. Even though the effect of the cell size was visible during the rapid rises in the field strength, it provided reasonably accurate measurement of the field amplitudes inside both the 31nm Au and 5nm VO_2 layers. Figure 5.6 shows a gradual buildup of the electromagnetic energy density across the Au layer, followed by its exponential fall in the VO_2 layer when the latter was in an insulator state. For metallic VO_2 the electromagnetic energy density was lower on average, and

slowly increased in the VO₂. In the metallic case, such behavior might be related to the possibility of SPP excitation/coupling in the metallic VO₂, demonstrated in previous experiments [102].

The FDTD computation predicted that with a threshold transition laser power level of 2.0mW (which equals 1.76 kV/m electric field strength in air), an enhanced electric field of 29.6 kV/m in the VO₂ at 42.3° resulted, which was the nadir of simulation for the insulating case of VO₂. From the data in Fig. 5.2, it was noted for the high-power level scan (5 mW) that the IMT initiation occurred 0.35° below the resonance angle of the insulator state of VO₂. Utilizing that 0.35° shift below the VO₂ insulator's nadir angle in the FDTD simulation, a calculation of the enhanced electric field strength was made at that angle for 5 mW laser power level (which was equal to 4.40 kV/m in air). The simulation computed electric field enhancement at that angle was 30.9 kV/m in the VO₂. These separately computed IMT threshold values showed the consistency of the approximate onset of the IMT measured in this sample.

Fig. 5.7 illustrates calculation of the FDTD for the field strengths at the VO₂ interface of the Au layer. There was a strong difference in the E-field values between the resonant angle (45.16°) where the field jumps up to approximately 65 kV/m for a 5mW laser input (red line) compared to the non-resonant angle of 44.8°

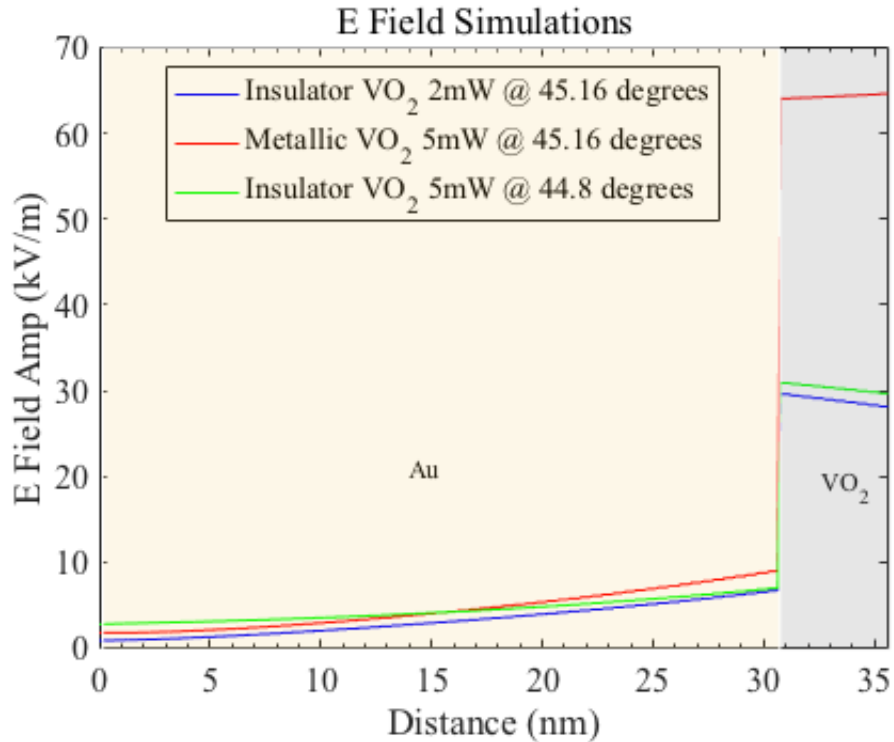


Figure 5.7: FDTD simulations for E field amplitude in the sample for the case of Insulating VO₂ state (blue line) and metallic VO₂ (red line) at the nadir location. The green line is the field amplitude at the angle location the where the deviation from Fig 4 starts at the power full IMT power threshold.

with the same 5mW laser input (green line) and a calculated E-field enhancement of 30.9 kV/m. Fig 5.7 shows the strong response to field enhancement with respect to power and angle near the resonance.

A brief comparison of electric fields from alternative IMT mechanisms in VO₂ highlights the benefits of this new approach. Researchers required a field on the order of 34 kV/m [5] for a DC electric field method with a four lead resistance measurement in a 200 μm long VO₂ sample. In a second report, a field estimated at 65 MV/m at room temperature [105] was estimated via an atomic force

microscope measuring through the thickness of a VO₂ thin film on a Si doped substrate. The E-field from the four lead resistance measurements was ~10% higher than the calculated E-field induced by the SPP at the transition thresholds. Another transition process was the photo induced IMT in VO₂ via a pump probe ultrafast measurement, using an amplified Ti:Sapphire laser at 800 nm [18, 19]. Assuming an average pulse power for transition threshold of 7 mJ/cm² with a pulse duration of 0.5 ps [18] the laser peak intensity gave an instantaneous peak intensity of $1.23 \cdot 10^{10}$ W/cm², which correlated to a 304 MV/m peak electrical field strength in air. From [107] another short pulse process for inducing the IMT in VO₂ was used along with plasmonic antennas to lower the transition energy. It used an instantaneous peak intensity of $2.63 \cdot 10^8$ W/cm². The electric field amplitude for their beam would be at 44.5 MV/m. Both of these photo induced methods involved very high electric fields.

5.3 Hunt for Hysteretical Response in VO₂

The IMT in VO₂ initiated by SP methods did not involve thermal heating. This was verified by using a FLIR thermal camera monitoring the back of the VO₂ sample while the laser was inducing SPP on the Au layer, as discussed above.

Heating VO₂ exhibited hysteresis in optical reflectivity with temperature. This type of thermal hysteresis was discussed in section 4.2.5 in Fig. 4.6 for the 30 nm VO₂ sample on TiO₂. The SPP generated IMT are electronic in nature. The

question arises: is it possible to detect hysteresis effects in signals when causing IMT by SPP? Thermal hysteresis can be thought of as the turn-on and turn-off of individual VO₂ grain sizes at different critical temperatures throughout the sample [108]. It would be interesting for practical applications to know if an SPP induced IMT in VO₂ exhibited any hysteresis. One variable that could display hysteresis would be the laser power threshold. The transition is sensitive to being at the resonant angle within 0.3°, hysteresis in the angle variable would be difficult to accomplish.

The experimental setup to test for this effect was described in section 3.1.3, Fig 3.5. An OAM modulator was inserted into the beam line to allow power control. It allowed a linear sweep of the laser power across the IMT threshold level between 2 to 5 mW, determined from the scans shown in Fig 5.4. Measurements were made at the metallic SPR angle and then at far off resonance where no IMT should occur. The stability, variability, and nonlinearity of photodiodes responses are a complication for these measurements. When a simple silicon diode was employed, the signal vs. power did not follow a simple phase relationship but was distorted. The purpose of using a balanced diode was to try to remove the effects of variability between photo diodes. Balancing the SPR signal with an amplitude adjusted power signal was to try to enhance the diode's sensitivity to best detect any hysteresis effect, if it was present. The signals from the balanced diode were

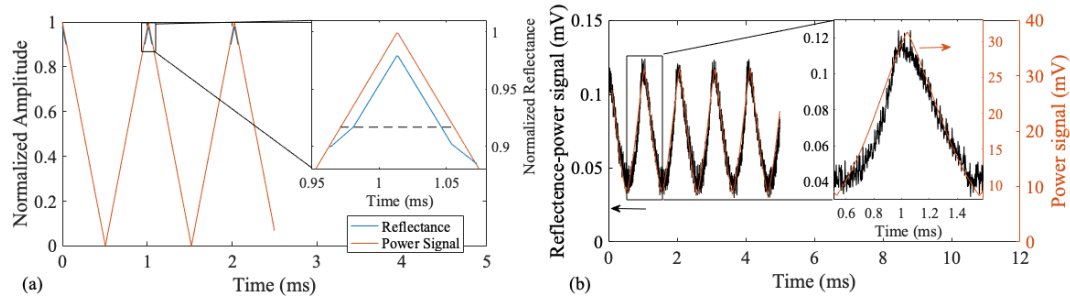


Figure 5.8: (a) A simulation of a triangle wave that represents the normalized reflectance versus time. By putting the laser signal through the optical modular, the amplitude of the laser light can be varied over a power range that crosses VO₂'s IMT threshold. At the power level where the IMT is initiated, a jump in the reflectance (a loss in R) should occur. If there is hysteresis, the reflectance jump with a rising laser power will not follow the reflectance jump with a falling laser power, which would show separate paths in the rising power vs. falling power. (b) An implementation of the concept using a laser's output that is modulated with an OAM to control the power level between 1.8mW to 6.4mW of laser light power, which is crossing the IMT threshold. The black line is the raw signal from the SPR monitor that comes from the balanced photodiode which is monitoring changes in the SPR reflectance output from the sample. The red line represents the laser's output.

recorded; one diode read the reflectance from the sample while the other diode recorded the power input to the sample. Fig 5.8(a) demonstrates the expected signal in the case of IMT occurring during the power sweep. If there was a small variation of the reflectance, it would be seen near the threshold of the IMT. In the case of hysteresis, the change in the reflectance would occur at different power levels and might show differences in the rate of change of the reflectance with power swings.

Fig. 5.8 (b) shows the raw signal from the balance photodiode when the laser power was swept from 1.8 mW to 6.3 mW. There is no clear response that would be indicative of the hysteresis.

Recorded signals were then mapped on a graph of the normalized balance diode output vs the power to get a better visualization of the possibility of hysteresis, Fig.5.9. The normalized balanced diode signals laid nearly horizontal on the graph with respect to the power. This presentation was similar to a Lissajous type figure. The idea was to enhance any evidence of the IMT effect in the signal. If there was any detectable hysteresis in the IMT, there should be differences between the signal on its way up through the IMT versus signal reversing through the IMT.

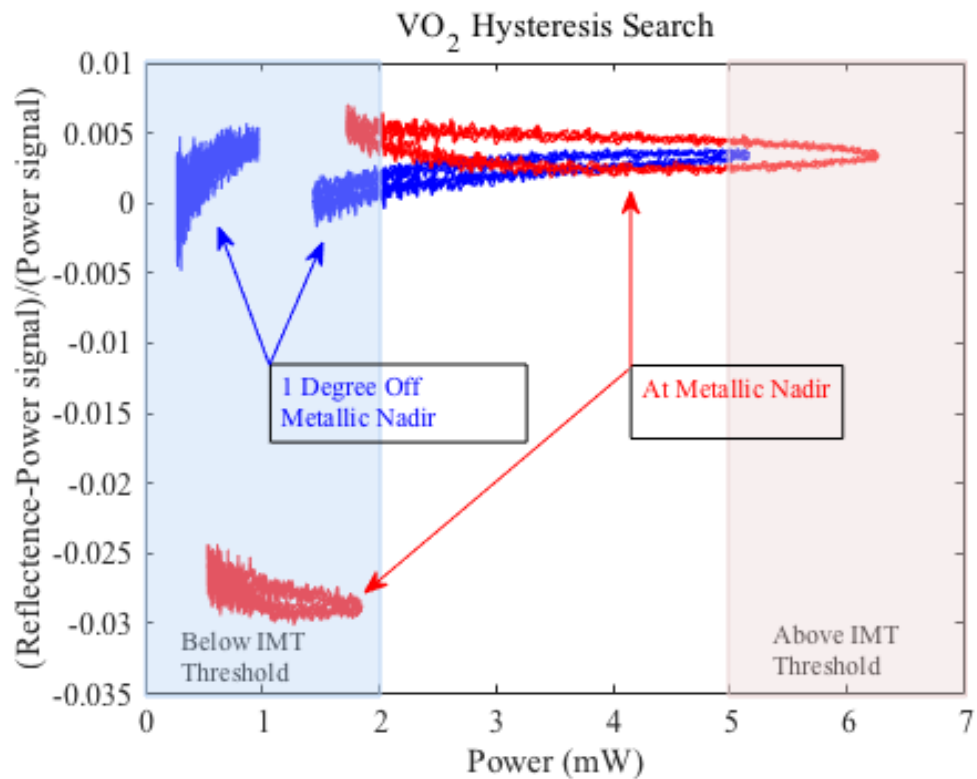


Figure. 5.9: Hysteresis study. Red lines are the measurements made at the nadir location over a power range that should cause the IMT to occur. The blue lines are made 1 degree off the nadir location where SP will not be generated, and the power is from above and below the IMT threshold.

This method did not have enough signal to noise to clearly detect the IMT transition. Fig.5.9 shows the responses for several power ranges and angle locations relative to the resonant angle. For the red line examples, the measurements were made at the metallic SPR angle where the field enhancement would be the strongest and the sample was most able to cross into the metallic state. This location was seen in Fig. 5.2 and 5.3 (as the red line). The blue traces were made one degree off resonance where the field enhancement effect was too low to induce the IMT at that angle. Fig.5.7 shows that the IMT threshold was not attained at 0.3° off resonance, so at 1° off resonance this measurement should not induce the IMT, while at resonance the power crosses the IMT threshold. In Fig.5.9 Both scans were performed at the metallic resonance angle as shown in Fig 5.9 and there was some loop forming in the traces. Since hysteresis was expected to appear only at the resonant angle over the full range of powers that crosses the IMT threshold, the lower power scan should not have shown any looping. At the 1 degree off resonance, the high-power measurement again showed a loop forming on the trace. Because this was off resonance the looping could not be evidence of hysteresis from the IMT, so this loop was not related to the hysteresis of an IMT. For the low power off resonance case, the noise was excessive and no clear Lissajous loop was evident. Overall, there was no clear evidence of hysteresis in these measurements and if hysteresis was present, it was buried in the noise.

5.4 Conclusion

The FDTD model shows that SPP excitation concentrated significant electromagnetic energy density into the VO₂ layer. Observed changes of reflectivity upon SPP excitation correlated with changes in the optical properties expected for the IMT in the VO₂ sample. The optical model suggests that the SPR sample should have a 0.1° shift in the resonance's nadir location. Experimentally, a resonance's nadir shift of 0.07° was observed. Optical properties of VO₂ appear to exhibit a shift in the resonance's nadir location at approximately 2 mW of laser power. At 5 mW of power, changes in the shift in the resonance's nadir location were saturated, suggesting that the sample had fully transitioned. Finally, wider angle scans around resonance performed at 10 μW and at 5.4 mW showed that the shift in the SPP resonance curves only appeared near the resonance's nadir. There is an unobservable difference between the two resonant curves at high and low laser powers away from the SPP resonant point. Near the resonant point for the higher power measurements, the VO₂ appeared to behave like a metallic material while the lower power measurements indicated the behavior of the insulating state of VO₂. Thermography verified that there was no discernable heating in the VO₂ layer of the sample. Attempts were made to detect IMT hysteresis in the sample for the SPP induced IMT. With the level of noise in these measurements, the test did not detect any clear evidence of hysteresis in VO₂ for this IMT process. SPP induced

IMT in VO₂ may allow a method of fast switching using lower energy transition of VO₂. An application for optical switching of arrays would be useful for an all optical beam steering system for use in the IR spectrum.

CHAPTER 6

Ultrafast Photo induced IMT in VO₂

6.1 Introduction

The purpose of studying VO₂ samples grown on TiO₂ and TiO₂:Nb at 3.1 eV was motivated by the need for developing a superior UV photo detector. One key benefit of VO₂ on TiO₂:Nb is its superior photocurrent generation with higher quantum efficiency. Another motivation is related to its potentially fast response. Techniques such as ultrafast time resolved measurements are advantageous for exploring the time dynamics and recovery response of VO₂ at the relevant wavelengths and provide a more complete understanding of the value of VO₂ on these substrates. Previous work used the same 3.1 eV pump on VO₂ but used different substrates like MgO, SiO₂, and Al₂O₃ and had perplexing $\Delta R/R$ responses [73, 74, 109, 110]. It is important to note, however, that those experiments were conducted on much thicker (>200nm) polycrystalline VO₂ films and with almost three orders of magnitude higher pump fluences that caused a thermal IMT. This work is the first demonstration of VO₂ on TiO₂:Nb displaying such temporal response patterns for 3.1 eV pumping and for much thinner (30nm) epitaxial film

samples with uniform crystal orientation and with much lower pump fluences that do not cause a thermal IMT. The experimental apparatus, section 3.2, discusses how the measurements are made. Section 4.2 describes the samples with XRD, AFM, and optical properties of the samples.

6.2 Photo Induced IMT in VO₂ on TiO₂ or TiO₂:Nb

Figure 6.1 shows the time resolved $\Delta R/R$ response of a 30nm thick sample of VO₂ on a TiO₂ substrate for different values of blue pump fluence. For higher fluences, ($>25 \mu\text{J}/\text{cm}^2$), the general time dependence is similar to the IMT dynamics produced by 800nm pump pulses [104, 111, 112]. An initial few ps rapid reduction in reflectivity due to IMT produced by a pump pulse, is followed by a

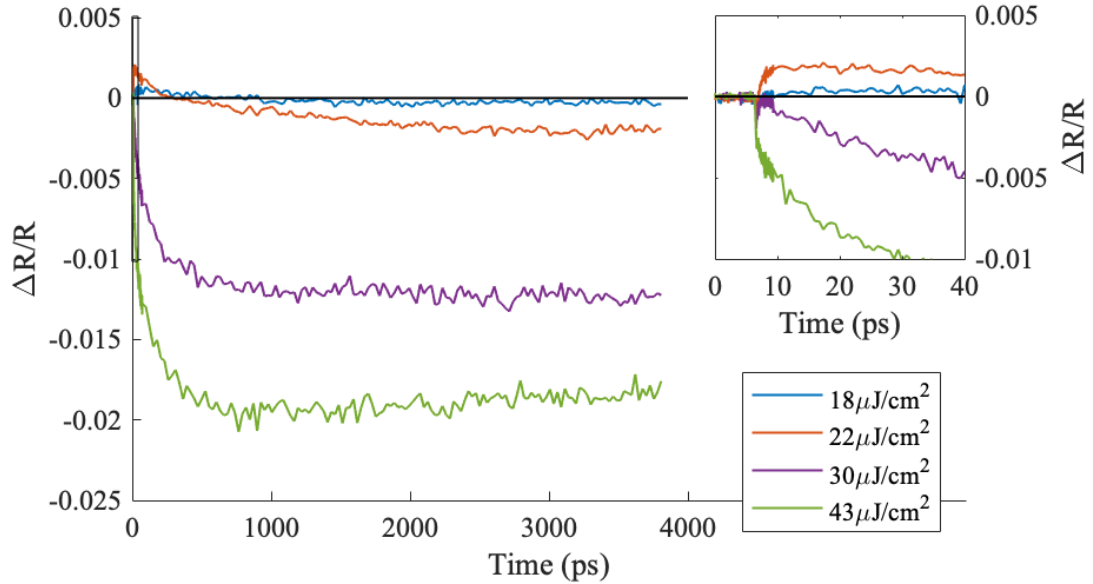


Figure 6.1: 30nm VO₂ on TiO₂ time response for various fluences from 0 to 4000ps. The insert at top right shows times from 0 to 40ps which corresponds to the first 1% of the data and the area of the insert is represented by the small box seen at t=0. The vertical scale of the insert directly aligns with the corresponding main $\Delta R/R$ scale.

“slow-growth” stage, in which the sample continues to transition to metallic stage for several hundreds of ps via slower phonon-mediated interactions. The slow-growth response behavior has been described for photoinduced VO₂ when pumped at 1.55 eV [104, 112], although this type of behavior was typically observed in the range of several tens of ps. The slow-growth response in the measurements lasted up to 1000ps, which can be related to differences in the surface roughness or grain size in the samples, since it has been shown that larger particles or grain sizes can slow down this transition process[113]. After slow growth the film began to relax back to its insulating state, causing the relative reflectivity to reverse direction and begin to increase toward zero again. Thermal recovery relaxation rates measured here were substantially faster than the previously measured value for VO₂/TiO₂ samples that had time constants of 200 ns [95], potentially due to the smaller thickness of our sample and substantially lower pump powers and is further discussed and quantified in section 6.4.

Unlike previous experiments, an unexpected variation in $\Delta R/R$ signal for low pump fluences, as shown in Fig. 6.1 was encountered. Specifically, an immediate increase in reflectivity was observed after the initial pump excitation, with the positive $\Delta R/R$ signal lasting up to a few hundreds of ps, depending on the pump fluence. The lowest fluency used, 18 $\mu\text{J}/\text{cm}^2$ (blue line), was too low to cause the IMT, and thus the negligible $\Delta R/R$ response indicated little change in

the optical properties of VO₂. However, even a slight increase in pump fluence to 22 $\mu\text{J}/\text{cm}^2$ (red line) produced noticeable optical changes and an increase in reflectivity to $\Delta R/R \approx 0.002$, followed by a slow linear decrease, crossing zero at approximately 400-500ps and finally reaching negative $\Delta R/R \approx -0.002$ at 2-3ns after the initial pump pulse. When the pump fluence was increased further to 30 $\mu\text{J}/\text{cm}^2$ (purple line), the system's response had a negative $\Delta R/R$ for all time delays, reaching $\Delta R/R = -0.0125$ after about 1ns. Further increase of fluence to 43 $\mu\text{J}/\text{cm}^2$, (green line), did not change the overall temporal dependence, but allowed a faster drop toward a lower reflectivity change $\Delta R/R = -0.02$.

6.3 Optical Response Diffusion Model

This unexpected increase of reflectivity patterns soon after the pump pulse occurred has been reported previously when thicker samples on different substrates were pumped with 3.1 eV photons, but at much higher fluences [74, 110]. The fluence-dependent reflectivity dynamics in these previous studies was attributed to constructive or destructive interference of the probe pulse reflecting off the evolving boundaries between various VO₂ phases inside the film. As shown below, this model can qualitatively capture the essence of our experimental results. The key difference between our work and that of Lysenko et al. [74] is that their pump power deposited onto the VO₂ film was high enough to induce the IMT thermally, in addition to direct photoexcitation. Thus, according to Ref. [74], the thicker VO₂ film did not

homogeneously undergo a thermal IMT across the thickness as the energy of the absorbed pump pulse diffused through the 100-nm thick film. In our samples, however, the energy required for initiation of the IMT was orders of magnitude lower and was attributed to the TiO₂ substrate-induced strain in epitaxial VO₂ films. Strain has been theorized to modify the bands and the effect has been modelled [114]. Furthermore, modifying the bands via doping of VO₂ has been shown to further lower the fluence requirements of the IMT [115]. In our experiment the expected temperature change is not sufficient for inducing IMT by itself. Overall heating of the 30nm sample was calculated to be less than 3° C which is well below the thermal IMT value for this sample starting at room temperature at the maximum fluence of 43 μJ/cm². This calculated temperature change was a conservative estimate based on the specific heat of VO₂ found in Ref. [116], the pump spot size, the sample thickness of the VO₂, and the assumption of 60% absorption from the pump energy as predicted by the optical model of the beam's energy entry into the VO₂. At these low energy densities, the system was nevertheless able to photo induce the IMT in a manner that produced a $\Delta R/R$ zero crossing that roughly mimicked the thermal IMT process proposed in Ref. [74].

To model the varying material states throughout the VO₂ film, the VO₂ material was treated as layers to be locally either an insulating layer, or a metallic layers, or a layer that is a combination of nucleated metallic area intermixed with

insulating material [50]. As the sample was probed in time, the fraction of metallic to insulator material evolved through the thickness of the sample. As a first order approximation, the changes in the VO₂ optical properties was modeled throughout the film thickness as temporally evolving processes based on a first order diffusion equation in one dimension in order to describe the VO₂ sample's atypical $\Delta R/R$ zero crossing response at the fluences used on these samples. For a delta function surface excitation, representing a sub-ps pump pulse, the solution to the diffusion equation is of the form:

$$\Phi(x, t) = \frac{1}{\sqrt{4\pi\kappa t}} \exp\left(\frac{-x^2}{4\kappa t}\right), \quad (6.1)$$

where Φ represents the material state (such as metal or insulator) of the VO₂ sample due to the photoexcitation, x is the depth, t is time, and κ is a diffusion constant. It is important to note that the exponentially measured value of the diffusion constant ($\kappa=2\cdot 10^{-7} \text{ m}^2\text{s}^{-1}$) is an order of magnitude lower than the reported thermal diffusion [116]

The solution form of the diffusion equation ignores the fact that the pump light would partially penetrate into the sample. (From the optical properties seen in Table 4.1. The penetration depth is about 32-33 nm depending on the conductive state in VO₂.) This would cause an initial jump in amplitude at the beginning of the model's time, but for a simple model it captures the essence of the IMT behavior at later times and is very instructive.

For a 30 nm sample, based on the penetration depth of the light (about 32-33 nm depending on the conductive state in the VO₂.) one would initially expect that the front layers of material would absorb many more photons compared to the deeper layers creating a gradient of converted material. Furthermore, VO₂ exhibits conversion from insulator to metal as localized islands [50]. This feature provides a large area of boundaries where the insulator to metal exists. Those boundaries occur where carrier band bending would be prevalent. If excited electrons and holes in those regions continue to exist, there could be forces at the boundaries that might favor continued evolution of the IMT at those boundaries. As those boundaries grow and coalesce the sample would demonstrate a diffusion-like process.

For application to the 30nm VO₂ sample, the 30nm thickness was discretized into 60 equal layers. Initially, all the layers were in the insulating state. The pump beam converted the surface layers into the metallic or intermixed metallic-insulator states. The distribution of the insulator or metal states was determined by threshold levels of Φ ; the higher threshold of Φ represents the transition between metallic and intermixed metallic-insulator states. The lower threshold represents the intermixed metallic-insulator states transitioning to the insulator optical properties. Between the upper and lower thresholds are layers of material with varying intermixed optical properties. In this model, the intermixed optical

properties were linear interpolations between the metallic and insulator optical properties in proportion to the relative Φ levels.

As time progressed, the sample composition evolved with time following the diffusion equation Eq.(6.1), causing deeper and deeper insulating layers to convert into metallic layers. A 4×4 optical matrix method was used [100] to calculate the probe beam's propagation through each layer, taking into account their proper optical properties and layer dynamics. The 4×4 optical method used here is explained in Appendix B. Fig 6.2 shows the film layer distribution at 10ps and 200ps. The color map shows the modeled depth ranges with insulating (blue), intermixed (rainbow), and metallic (red) optical properties. The black lines in Fig 6.2 show the plot of the real component of the index of refraction. For the small delays, the front surface undergoes the IMT while deeper regions are unaffected, as seen in Fig 6.2(a). As time progressed, the metallic VO_2 fraction appeared to be

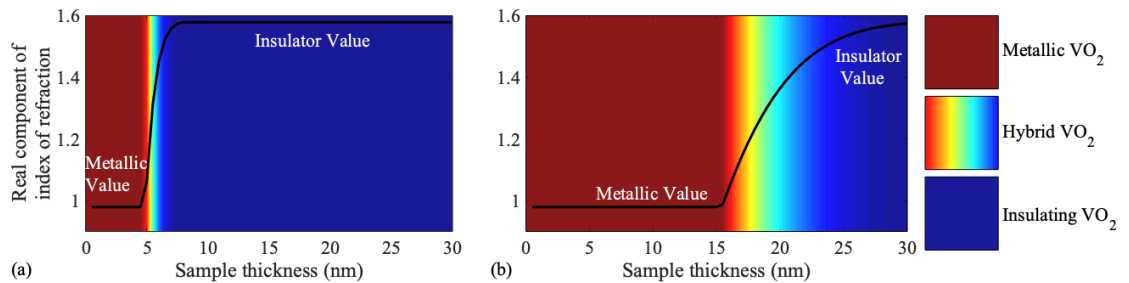


Figure. 6.2: Simulation of diffusion of the insulating VO_2 into metallic VO_2 layers. Red layers are metallic VO_2 . Blue layers are insulating. The colors between represent intermixed values of the optical properties of the VO_2 layers. The black line shows the values of the real component of the index of the reflection. The two graphs (a) and (b) are for 10ps and then 200ps in time. steps for the diffusion of the system.

diffusing into deeper regions of the film, increasing the depth of the IMT region, as seen in Fig 6.2(b). The interference of the probe beam reflected off various boundaries within the evolving film and the overall optical reflectivity briefly increased before finally decreasing when the sample becomes mostly metallic.

Model prediction, shown in Fig 6.3, qualitatively agree with the dynamics observed in the experiments. A wide range of relative pump powers was chosen to elucidate the general time behavior seen in our measurements. The temporal $\Delta R/R$ response of this model mimics the experimental observations $\Delta R/R$ (Fig. 6.1) in these samples, where the sample's $\Delta R/R$ response is initially positive and then goes

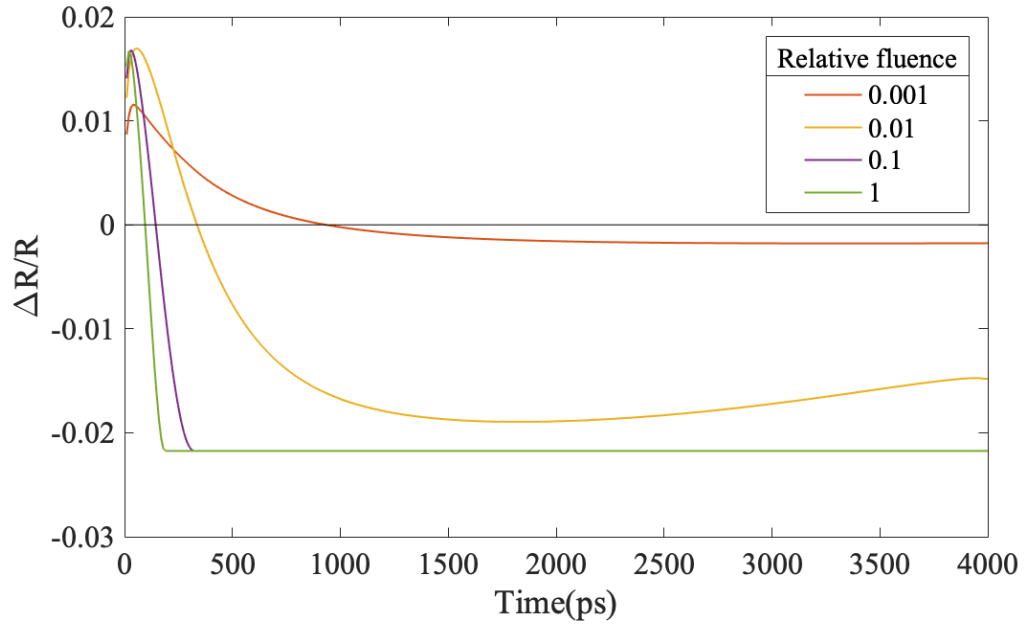


Figure. 6.3: Optical model response of 30nm VO_2 TiO_2 for various relative fluence of light using a 4×4 optical matrix method and the ellipsometry values with a hybrid layer of VO_2 between the insulating and metallic states. The relative fluence at level 1 represents the power to fully transition the film in 200ps with blue light.

negative over time, ultimately reaching the negative value of about -0.02 for the full transition to the metallic state, in full agreement with experimental results for higher fluence. The time at which the reflectivity switched from positive to negative showed similar strong dependence on the pump fluence, with lower pump powers resulting in longer crossover times. This simple model overestimates the initial positive $\Delta R/R$ spike, even for higher pump fluence that stemmed from the oversimplified assumption of the initial delta function excitation. This model does not deal with initial pump beam penetration into the sample, it always predicted a positive spike in the beginning. Since the IMT dynamics at short times were not studied, this model was sufficient to explain the long-term reflectivity evolution. However, if more accurate calculations are desired, one would need to properly account for the beam penetration and the lateral spread of metallic state at the VO_2 surface after the pump pulse. That should dampen the initial fast $\Delta R/R$ rise that was seen in Fig 6.3.

6.4 The Effects of Nb Doping of the TiO_2 Substrate on The Photoinduced VO_2 IMT Dynamics

Recent studies demonstrated the strong effect of doping TiO_2 substrate with Nb on the photoelectric properties of VO_2 in blue and UV spectral ranges [79], due

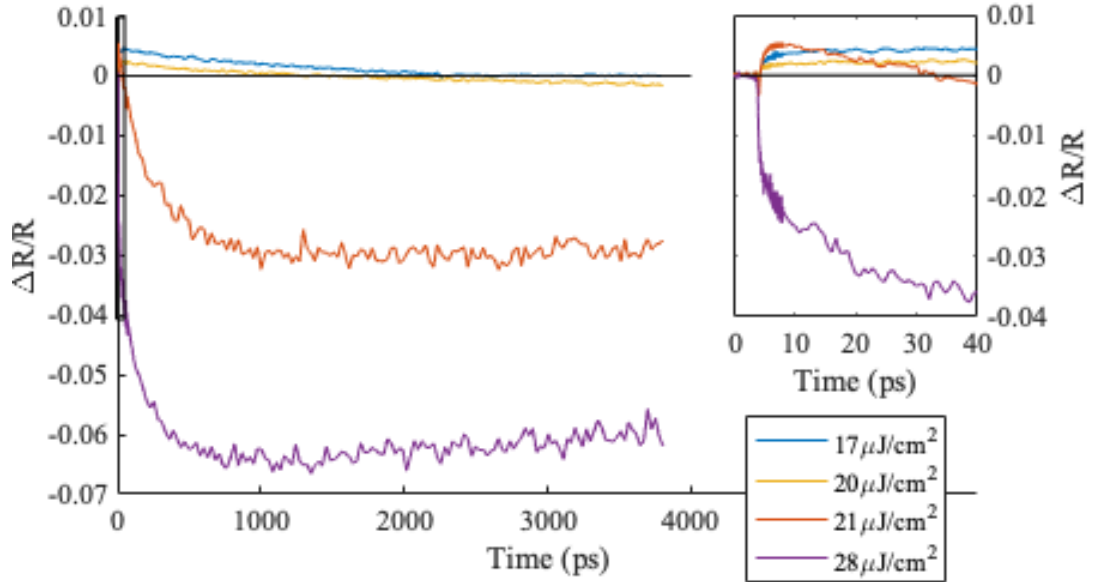


Figure 6.4: 30nm VO₂ on TiO₂:Nb time response for various fluences from 0 to 4000ps. The insert at top right shows times from 0 to 40ps which corresponds to 1% of the total data and is represented by the small box seen at t=0 in the main graph. The vertical scale of the insert is equivalent to the main $\Delta R/R$ scale.

to a more efficient hole diffusion process and band bending at the VO₂/TiO₂ interface. To investigate the possible effects of such doping on the photoinduced IMT, VO₂ samples grown on the volume doped TiO₂:Nb substrate were used, as described in Sec. 4.2. Fig 6.4 shows the data for VO₂ on TiO₂ doped with Nb. The overall behavior of the optical reflection was very similar to that of the VO₂/TiO₂ sample. At the lowest fluence used on this sample, 17 $\mu\text{J}/\text{cm}^2$ (blue line), the $\Delta R/R$ response changes very little and displays a positive change only with a slow recovery to zero after ~ 2 ns, indicating little change in the optical properties of the VO₂. At a slightly higher fluences of 20 $\mu\text{J}/\text{cm}^2$ (orange line) small changes in the

$\Delta R/R$ were seen throughout the time scale. The reflectance ratio crossed zero from a positive ratio of 0.002 to a negative ratio of 0.002 at about 2 ns. Even a very modest increase in fluence by just a few percent to $21\mu\text{J}/\text{cm}^2$ (red line) yields a more drastic response. The material now exhibits a large positive change in reflectivity, followed by a significant negative $\Delta R/R$ after about 30 ps with a sharp downward slope. The graph bottoms out at a $\Delta R/R$ of about -0.03 in magnitude at around 1-2 ns, then starts to relax slowly back to zero. At the highest fluence level of $28\mu\text{J}/\text{cm}^2$, (purple line), the response is even stronger in magnitude and only trends negative with a peak drop of $\Delta R/R$ to -0.065, while the rate of the response is similar to the $21\mu\text{J}/\text{cm}^2$ fluence.

Despite many similarities, the careful comparison of Figs. 6.1 and 6.4 reveals some clear differences between the optical properties of the two samples. For example, it is obvious that the maximum magnitude of the reflectivity change was about three times higher for the samples with the doped substrate. The peak $\Delta R/R$ signal seen in Fig. 6.4 for the VO_2 on $\text{TiO}_2:\text{Nb}$ substrate was about -0.065 as compared to VO_2 on plain TiO_2 substrate, which was -0.02. The optical properties correctly predicted the $\Delta R/R$ for VO_2 on TiO_2 substrate, Table 4.1. In order to obtain a value of $\Delta R/R$ of a magnitude -0.065 for VO_2 on $\text{TiO}_2:\text{Nb}$ substrate, the index of refraction of the $\text{TiO}_2:\text{Nb}$ substrate needed to be lowered from about 2.5 down to the range of 2 (this assumed the VO_2 thin film's optical properties were

constant). The reduction of the refractive index by doping has been reported for thin films of TiO_2 for which the 5% Nb doping resulted in a reduction of the index of refraction by 5% [117].

The other distinct feature of VO_2 samples with the Nb-doped substrate was an even lower fluence threshold ($21 \mu\text{J}/\text{cm}^2$) required to accomplish the IMT and the faster evolution during both the “slow growth” IMT stage and recovery stage, compared to the undoped substrate. Fig 6.5 insert shows examples of the $\Delta R/R$ data for VO_2 on TiO_2 and VO_2 on $\text{TiO}_2:\text{Nb}$, plotted from 0 to 4000ps and shows

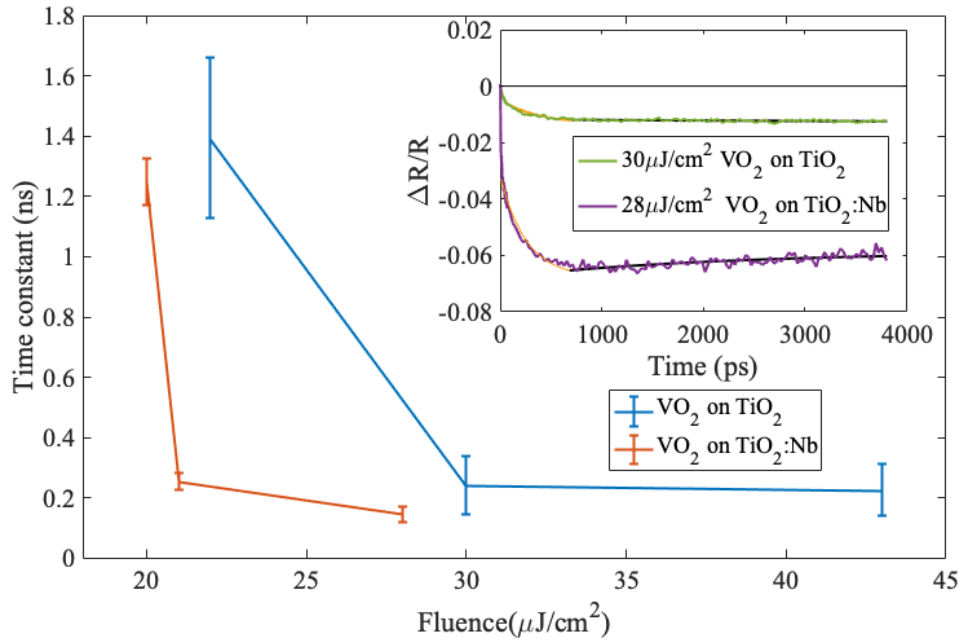


Figure 6.5: Time constants for the slow growth and recovery periods of the $\Delta R/R$ for the for the two VO_2 samples. The blue line is for VO_2 on TiO_2 and the red line is for VO_2 on $\text{TiO}_2:\text{Nb}$. The insert is the graph of $\Delta R/R$ response of the 30nm VO_2 on TiO_2 at $30 \mu\text{J}/\text{cm}^2$ (green line) and 30nm VO_2 on $\text{TiO}_2:\text{Nb}$ at $28 \mu\text{J}/\text{cm}^2$ (purple line). The time constant fits for both samples are shown as orange for the slow growth fit and black for the recovery fit.

the slow growth exponential (orange lines) along with start of the exponential recovery (black lines).

The rates of these time responses were strongly fluence dependent. The responses for the lowest pump fluences were not fitted as they were not amenable to simple exponential time constants. For VO₂/TiO₂, increasing the fluence from 22 μJ/cm² to 30 μJ/cm² resulted in a 83% rate increase in the slow growth rate, while an increase from 22 μJ/cm² to 42 μJ/cm² resulted in about 84% of the slow growth rate, corresponding to an additional 1% increase in rate that suggested that the slow growth rate reached a plateau for that sample at higher fluences, Fig. 6.5. For VO₂ on TiO₂:Nb, increasing the fluence from 20 μJ/cm² to 21 μJ/cm² appreciably increased the slow growth rate by approximately 80%. An increase from 20 μJ/cm² to 28 μJ/cm² only resulted in an 88% rate. This was an additional 8% increase, suggesting that the VO₂ on TiO₂:Nb slow growth rate leveled off similar to VO₂/TiO₂, but at lower fluence. For the present samples, the fastest slow growth was seen at 145 ps for the VO₂ on TiO₂:Nb and 224 ps for the VO₂ on TiO₂. For comparison with previously published work, the slow growth component from Fig 6.5 was slower than has been reported previously [104] with reported rates of 6 to 15 ps.

The recovery rate of the VO₂ ΔR/R responses from the Fig 6.5 insert was 34.35^{+0.01}_{-0.02}ns for the VO₂ on TiO₂:Nb (28 μJ/cm²). For the 30 μJ/cm² VO₂ on

TiO₂, its long-time scale was still growing and produced a larger error with values of $49.32^{+0.66}_{-0.51}$ ns. The 43 $\mu\text{J}/\text{cm}^2$ scan of VO₂ on TiO₂ had a slower recovery time constant of $44.37^{+0.05}_{-0.05}$ ns. That fit is not shown in the insert in Fig 6.5 but the change in the rate can be observed in Fig. 6.1 between the 43 $\mu\text{J}/\text{cm}^2$ scan and 30 $\mu\text{J}/\text{cm}^2$. These recovery rates are faster than what has been reported in ref [95]. Difficulty with these measurements reflects the limited available delay time to truly evaluate the long recovery times, resulting in large confidence limits.

6.5 Photo Induced IMT in VO₂ TiO₂:Nb for Different VO₂ Layer Thickness

Studies were conducted on a thickness series of VO₂ on doped substrates. The samples studied were 15 nm, 22 nm, and 50nm of VO₂ on TiO₂:Nb.

6.5.1 15nm Thick Sample

A series of fluences similar to fluences used in sections 6.2 and 6.4 for the 30nm VO₂ on TiO₂ and on TiO₂:Nb was applied to the 15nm thick VO₂ sample on TiO₂:Nb. The sample $\Delta R/R$ response can be seen in Fig. 6.6. As in Figs. 6.1 and 6.4 and in sections 6.2 and 6.4, the 15nm sample demonstrates very small changes in $\Delta R/R$ at the low pump fluence of 18 $\mu\text{J}/\text{cm}^2$ indicating the IMT is being initiated at a level of 1% (orange line). Increasing the fluence to 21 $\mu\text{J}/\text{cm}^2$, the yellow line in Fig. 6.6, begins to see signatures of the IMT transition (5%) as seen occurring

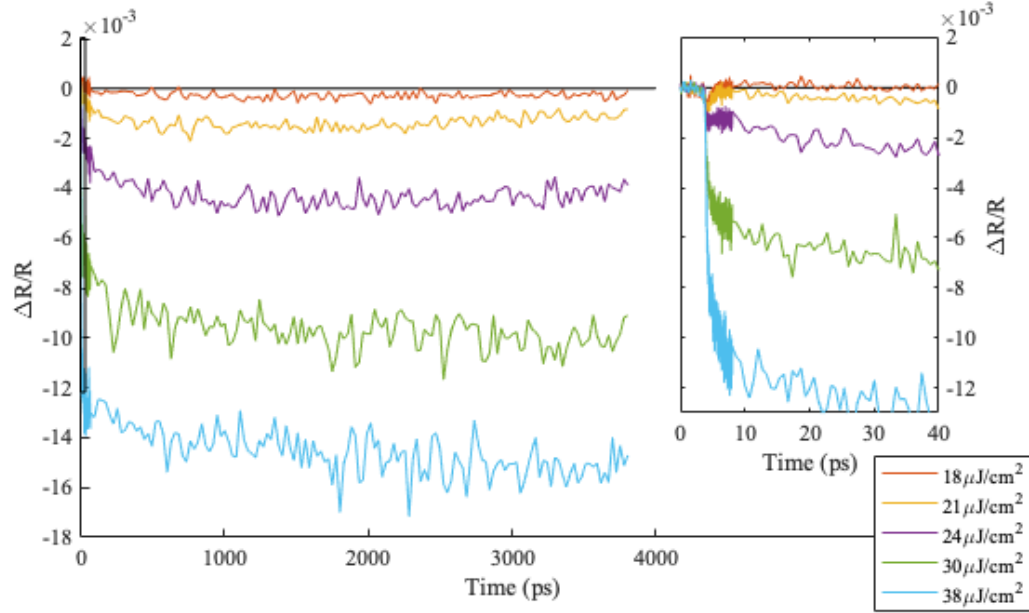


Figure 6.6: 15nm VO₂ on TiO₂:Nb time response for various fluences from 0 to 4000ps. The insert at top right shows times from 0 to 40ps which corresponds to 1% of the total data and is represented by the small box seen at t=0 in the main graph. The vertical scale of the insert is equivalent to the main $\Delta R/R$ scale.

in the hundreds of ps out to 4 ns time frame with the sample. Once the fluence exceeds 24-38 $\mu\text{J}/\text{cm}^2$, stronger responses were seen as the purple, green and blue lines in Fig. 6.6, indicative of the IMT occurring in the sample. A comparison of the 15 nm sample was compared to the 30 nm sample for the thin film from Section 6.4 and Fig 6.4. The $\Delta R/R$ amplitude was smaller. Since the reference reflectivity values (R) of these two samples were approximately equal (within 20%), it was ΔR reflection variations that led to the $\Delta R/R$ differences. This was expected due to the different optical reflection effects caused by different thicknesses of the two layers. One other unique effect seen in Figure 6.6 is that at the higher fluence scans did not show a recovery of signal back to zero during the 4ns of measurement, as

was seen in the 22 nm and 30 nm samples of VO₂ on TiO₂:Nb. The time constant and its comparison to other samples is discussed further in section 6.5.4.

The other striking feature that is specific only to the 15 nm sample is the lack of the zero crossing in the $\Delta R/R$ signal in the thickness series. The 15 nm sample was the only sample that did not exhibit the zero-crossing effect throughout the entire series thicknesses of VO₂ thicknesses grown on TiO₂:Nb samples when pumped at 3.1 eV. This was due to thin film interference that was discussed in the VO₂ diffusion model, Section 6.3, that confirms the experimentally observed reflectivity behavior. Fig. 6.7 shows the diffusion model's response for the 15nm

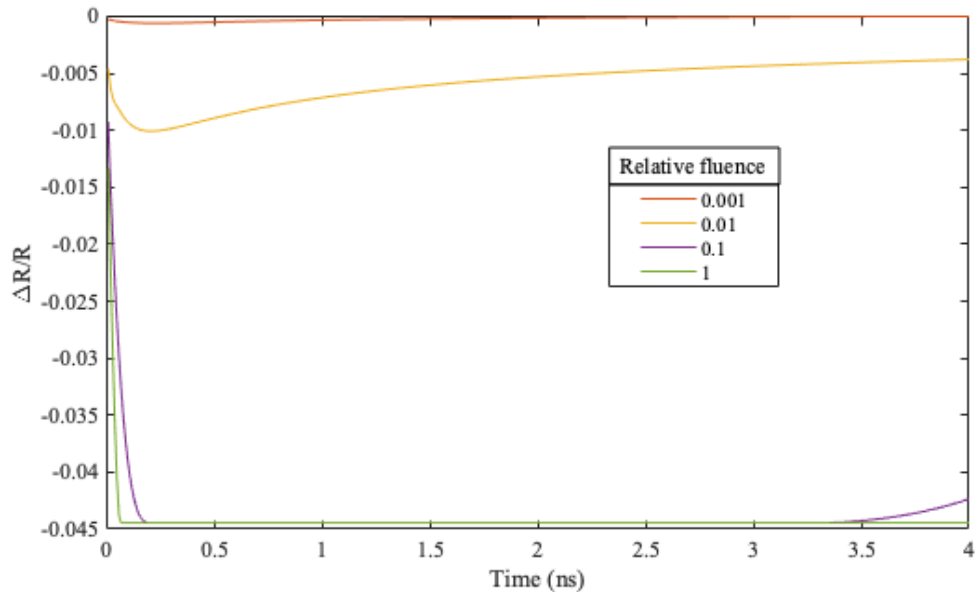


Figure 6.7: Optical model response of 15nm VO₂ TiO₂ for various relative fluences of light, using a 4×4 optical matrix method and the ellipsometry values with a hybrid layer of VO₂ between the insulating and metallic states. The relative fluence at level 1 represents the power to fully transition the film in 200ps with blue light.

sample. This figure uses the optical properties of the 30 nm VO₂ sample on TiO₂, just as in section 6.3, but the thickness of the model was changed to 15 nm, and the number of layers was set to 30 to maintain the same ratio of thickness to layers as the 30nm diffusion model. The diffusion rate was kept constant. It was possible that there were differences in the optical properties between the different samples in these measurements.

The model response from Fig. 6.7 has similar features to the experimental response seen in Fig 6.6 in that both have negative $\Delta R/R$ for all fluences. The model gave a much larger response in the $\Delta R/R$. It may be that the thin film optical properties of the 15 nm sample were different than the 30 nm optical properties of the VO₂ on TiO₂ used for the model.

6.5.2 22nm Sample

Figure 6.8 shows the results of the pump probe measurements for the 22 nm sample of VO₂ on TiO₂:Nb. Both the 22 nm and 30 nm VO₂ on TiO₂:Nb exhibited the same general behavior of an initial $\Delta R/R$ rise and then it transitions negative. As in the 30 nm sample of VO₂ on TiO₂:Nb, the zero crossing in the $\Delta R/R$ response and the sample's crossing was dependent upon power. For the low fluence measurements, the zero-crossing occurred later, while for the higher fluences, it rapidly fell to negative ranges. The peak negative amplitude $\Delta R/R$ change seen

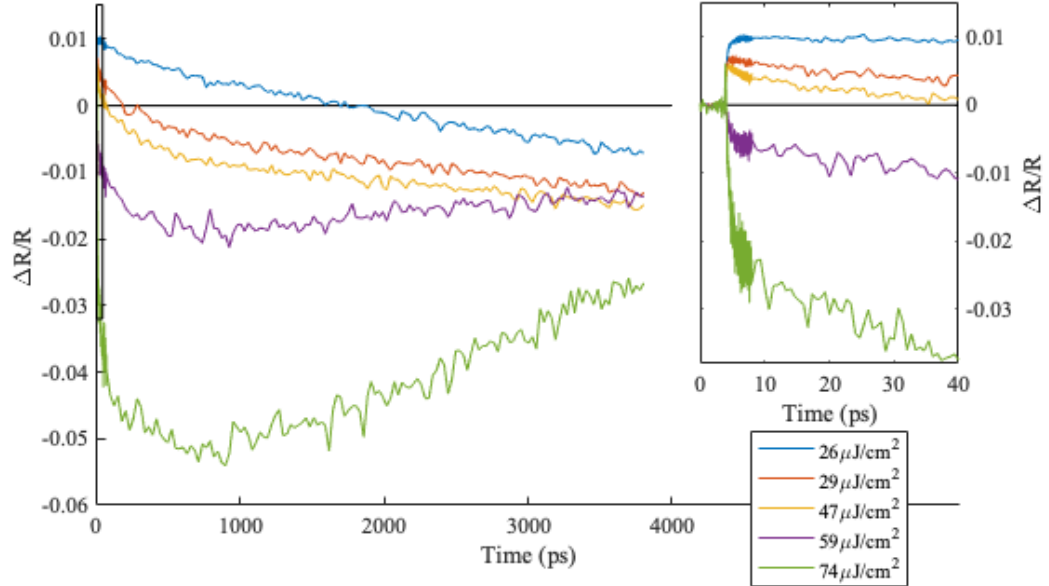


Figure 6.8: 22nm VO₂ on TiO₂:Nb time response for various fluences from 0 to 4000ps. The insert at top right shows times from 0 to 40ps corresponding to 1% of the total data and is represented by the small box seen at t=0 in the main graph. The vertical scale of the insert is equivalent to the main $\Delta R/R$ scale.

for the 22 nm sample was -0.05 and was close to that of the 30 nm sample of -0.06. Both samples showed recovery behavior of the $\Delta R/R$ values tending back towards zero at the 1000 ps range for the higher fluences.

A noticeable difference between the 30 nm sample and the 22nm sample was the fluence required to reach the maximum range of $\Delta R/R$. The thinner sample required approximately 2.6 times more fluence than the 30 nm sample.

6.5.3 50nm Sample

The thickest sample tested and grown was 50 nm VO₂. As seen in Figure 6.9, this sample exhibited a similar $\Delta R/R$ response of the zero-crossing behavior seen in the 22nm and 30 nm samples, where the $\Delta R/R$ response rapidly rose and then more

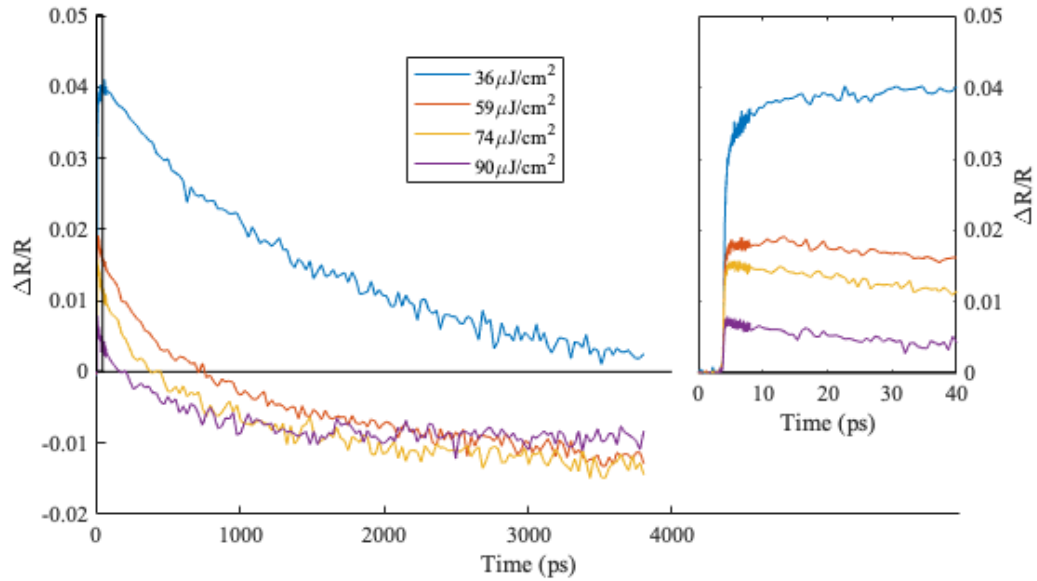


Figure 6.9: 50nm VO₂ on TiO₂:Nb time response for various fluences from 0 to 4000ps. The insert at top right shows times from 0 to 40ps which corresponds to 1% of the total data and is represented by the small box seen at t=0 in the main graph. The vertical scale of the insert is equivalent to the main $\Delta R/R$ scale.

slowly fell before crossing into negative range. A unique feature of the 50nm sample was its strong positive amplitude response seen in the $\Delta R/R$ scans, with the 36 $\mu\text{J}/\text{cm}^2$ fluence measurement being the highest $\Delta R/R$ at a maximum peak amplitude of $\Delta R/R=0.04$, and it's decaying toward zero without a zero crossing before 4000 ps. As the fluency increased, the peak positive $\Delta R/R$ decreased and the time of the zero-crossing shortened. Another interesting effect was that the negative $\Delta R/R$ amplitude was smaller than in the 22 nm and 30 nm samples.

These features coupled with the positive peaks of $\Delta R/R$ seen on the 50 nm sample, inferred thin film interference in the sample. The positive spike seen in the low power measurement corresponded to when the first initial layers converted

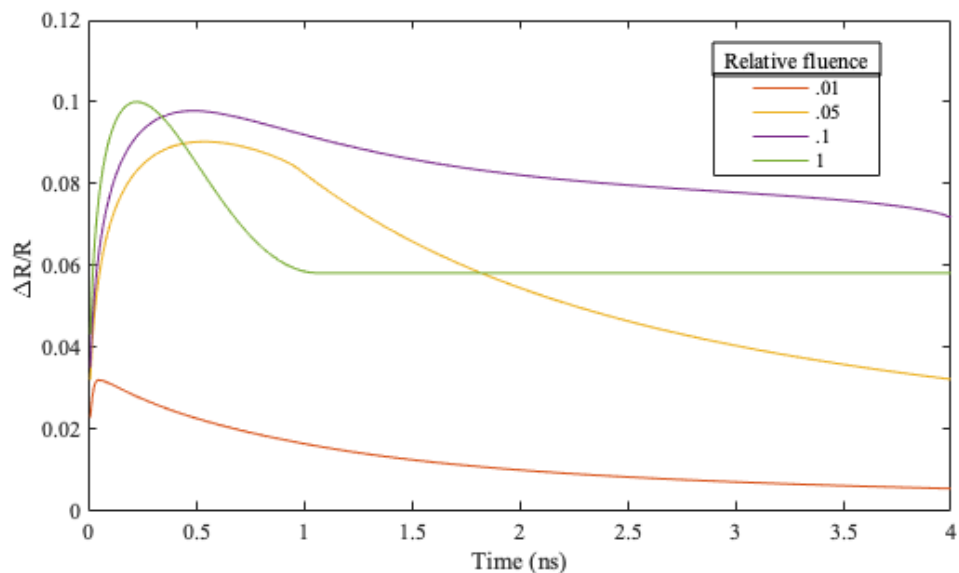


Figure 6.10: Optical model response of 50nm VO₂ TiO₂ for various relative fluences of light, using a 4×4 optical matrix method and the ellipsometry values with a hybrid layer of VO₂ between the insulating and metallic states. The relative fluence at level 1 represents the power to fully transition the film in 200ps with blue light.

into a metallic state, but the back layers were still insulating, giving a net positive response. The diffusion model showed this response in general, although it did not exhibit a negative $\Delta R/R$ at long time scales as seen in Fig 6.10. The model shows the $\Delta R/R$ decreasing, but not crossing-zero as in other modeled thicknesses. As the fluence was increased the loss of amplitude occurred because the ratio of metallic to insulator layers in the samples produced destructive interference. When the sample was fully transitioned, a negative $\Delta R/R$ amplitude of -0.01 was achieved. For the 50 nm sample, unlike the 22 nm and 30 nm samples, no recovery was discerned in the long-time scales. This suggests that the optical properties of the 30 nm sample are different from the 50 nm.

6.5.4 Time Constants

For $\Delta R/R$ time responses seen here, simple exponential fits were used for the different thicknesses:

$$\Delta R/R(t) = c \cdot e^{(t-t_{off})/\tau} + A_{offset}. \quad (6.2)$$

where t_{off} is time of the pump pulse arrival, τ is the slow growth rate constant, c is a amplitude variable of the exponential, and A_{offset} is an offset to adjust the data to be positive for purposes of fitting it to an exponential rate. The data was windowed into regions where a single exponential was relevant and two windows were utilized identifying two-time constants, if possible. One rate was the slow growth rate for VO₂ thin films that was first discussed by Cocker and Radue.[104,

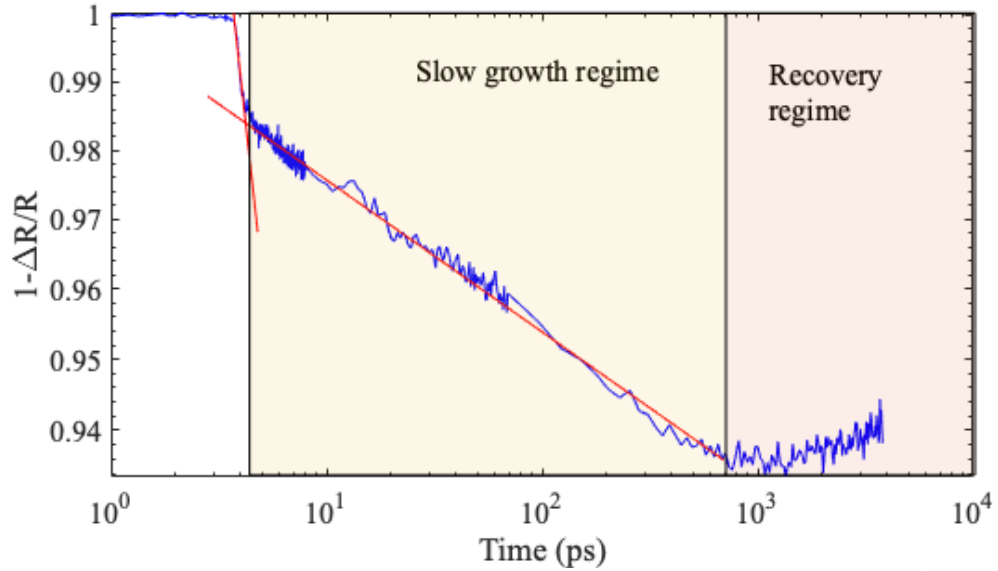


Figure 6.11: The log log plot of the 30nm VO₂ on TiO₂:Nb at 28μJ/cm² . (From Figure 6.4) The slow growth region is within the light tan colored box. The beginning of the recovery is shown in the pink box. This follows Radue et al. [104].

112] Following Radue and Cocker’s definition of “slow growth”, the initial fast turn on response of the sample to the pump pulse was ignored and the following slower component of the IMT was fitted with an exponential curve to extract the “slow growth” time constant, Fig. 6.11. The slow growth fits are shown as red lines overlaying the data (insert in Fig. 6.12). Table 6.1 through Table 6.4 show time constants for different thicknesses versus the fluences used for pumping. There are two columns summarizing the slow growth reported in ps and the recovery time constant (if measurable) reported in ns.

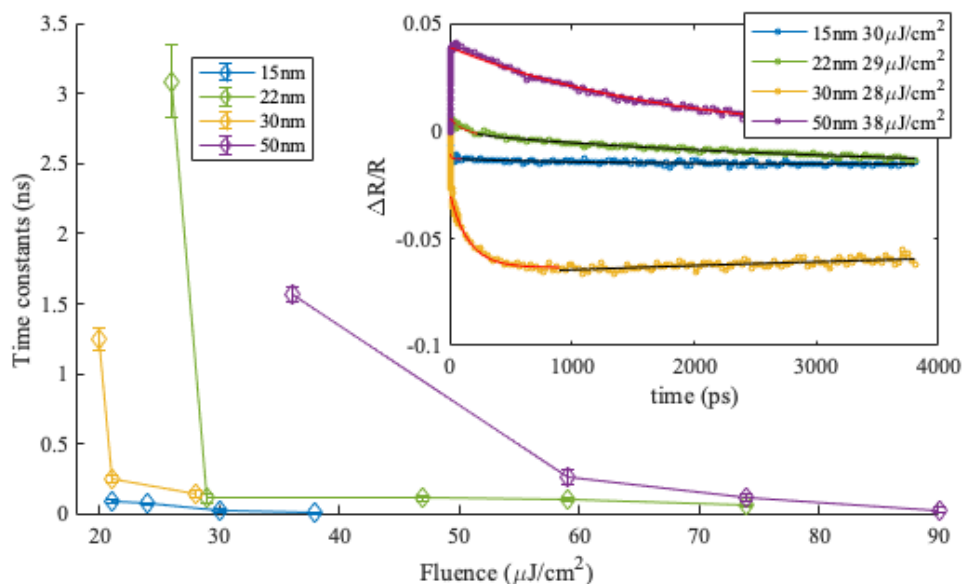


Figure 6.12: Time constants for the slow growth of the $\Delta R/R$ for the for the VO_2 samples of various thickness on $\text{TiO}_2:\text{Nb}$. The insert is the graph of $\Delta R/R$ response. The time constant fits for samples are shown as red for the slow growth fit and black for the recovery fit. It should be noted that the 50nm only show a single exponential slow growth fit and does not need the second time constant.

Some common effects of the slow growth rates are described. First, the slow growth values plotted in Fig. 6.12 shows each sample having a general relationship; as the pump fluence increased, the slow growth time constants decreased. There is an expected relationship between the higher pump powers and the number of carriers they excited into the conduction band. This larger number of carriers that is available to drive the initial IMT behavior throughout the samples, suggests conversion will happen at higher rates.

The effect of the sample thickness was analyzed by looking at the time constant at similar fluence values of $\sim 30 \mu\text{J}/\text{cm}^2$. At these fluences the 15 nm sample had the fastest constant, followed by the 22 nm and finally the 30nm samples. This highlights that smaller thicknesses have faster time constants at similar fluences. The thinner the sample, the less material to convert at a given fluence, hence it should complete the IMT process in less time for a given fluence.

All samples should return to their original baseline reflectivity eventually. In some cases, the measured recovery would require longer time delays than were measurable in this experimental setup. This was the case with the 15 nm and the 50 nm samples (Tables 6.1 and 6.4). These sample's diffusion evolution was ongoing even after 4 ns. A few measurements with higher fluences for the samples with thicknesses of 22 and 30 nm recovery behavior was measurable. (Tables 6.2, 6.3) The recovery rates for 22nm thick sample measurements were the fastest and

occurred at a fluence of 59 $\mu\text{J}/\text{cm}^2$ and 74 $\mu\text{J}/\text{cm}^2$ (Table 6.2). Both of these rates were faster than the 30nm samples on both TiO_2 and $\text{TiO}_2:\text{Nb}$ substrates. The recovery value was $34.35^{+0.01}_{-0.02}$ ns at the 28 $\mu\text{J}/\text{cm}^2$ for the doped substrate and $44.37^{+0.05}_{-0.05}$ ns for the undoped substrate.

Table 6.1 15nm Sample Time Constants

Fluence ($\mu\text{J}/\text{cm}^2$)	Slow growth (ps)	Recovery(ns)
21	$92.89^{+14.01}_{-14.04}$	X
24	$74.77^{+6.58}_{-6.58}$	X
30	$33.01^{+13.17}_{-13.17}$	X
38	$7.89^{+3.28}_{-3.27}$	X

Table 6.2 22nm Sample Time Constants

Fluence ($\mu\text{J}/\text{cm}^2$)	Slow growth (ps)	Recovery(ns)
26	3083^{+258}_{-258}	X
29	$113^{+15.1}_{-13.37}$	X
47	$113.6^{+16.6}_{-16.6}$	X
59	$107^{+13}_{-12.94}$	$8.483^{+0.723}_{-0.881}$
74	$60.59^{+5.85}_{-5.84}$	$4.843^{+0.274}_{-0.245}$

Table 6.3 30nm Sample Time Constants

Fluence ($\mu\text{J}/\text{cm}^2$)	Slow growth (ps)	Recovery(ns)
20	$1247^{+79.23}_{-76.2}$	X
21	$254.9^{+26.75}_{-26.31}$	X
28	$145.6^{+25.04}_{-23.78}$	$34.35^{+0.01}_{-0.02}$

Table 6.4 50nm Sample Time Constants

Fluence ($\mu\text{J}/\text{cm}^2$)	Slow growth (ps)	Recovery(ns)
36	1568^{+58}_{-58}	X
59	$260.4^{+53.9}_{-54}$	X
74	$120^{+28.2}_{-28.11}$	X
90	$32.3^{+17.01}_{-17.00}$	X

6.6 Effects of the Pump Photon Energy on the IMT of VO₂ on TiO₂:Nb

For completeness, one sample was measured in the pump probe setup using a 1.55 eV pump and probe photon energies to compare it with the 3.1 eV pump. For this measurement, the BBO crystal, polarizer, and the hot mirror were removed from

the experimental apparatus. The cross polarization between the pump and probe light was maintained.

Pumping VO₂ at 1.55 eV is more common in published research on VO₂ [11, 15-21, 95, 104, 111, 118-122]. The use of pump photon energy was interesting for comparison because the higher conduction bands were not available to carriers. In addition, lower valence energy states cannot be excited into the lower conduction bands with 1.55eV photoelectrons. Penetration depth of the light into the VO₂ samples was larger at this wavelength.

Fig 6.13 shows the response of the 30nm VO₂ on TiO₂ sample when pumped at 1.55 eV and demonstrates differences with the 3.1 eV pump. First, at pump fluence of 54 $\mu\text{J}/\text{cm}^2$ the $\Delta\text{R}/\text{R}$ response was at the threshold of the IMT transition. This corresponded to an IMT threshold value occurring at 3.1 eV at 20 $\mu\text{J}/\text{cm}^2$. The 1.55eV photon energy required a pump fluence of 94 $\mu\text{J}/\text{cm}^2$ to cause the full IMT in the sample. This was more than three times the fluency required using 3.1 eV photon, (28 $\mu\text{J}/\text{cm}^2$), even though the sample reached similar $\Delta\text{R}/\text{R}$ amplitude. This suggested that the 3.1 eV pump was more effective at accessing the IMT because doubling the fluency of the 1.55eV pump to account for the difference in photon energies did not produce the same IMT response. The excitation of the deeper electrons into the conduction band may affect the shielding of the potential Vanadium atoms.

Another effect seen in the 30 nm VO₂ on TiO₂:Nb sample when pumped at 1.55eV was that $\Delta R/R$ trended only negative (Fig. 6.12 insert) for all values of fluences. A possible reason for this could be the larger penetration depth for a longer wavelength pump produced a more uniform excited carrier distribution throughout the thickness. For the 3.1 eV pump on the 30 nm sample, the 1/e value of penetration depth is 30 nm, close to the sample thickness. At an 800nm wavelength the 1/e value is double the sample thickness. Thus, how the energy is deposited into the sample will differ between the two pump energies. For high pump photon energy of 3.1 eV, the excited carrier density will be more weighted

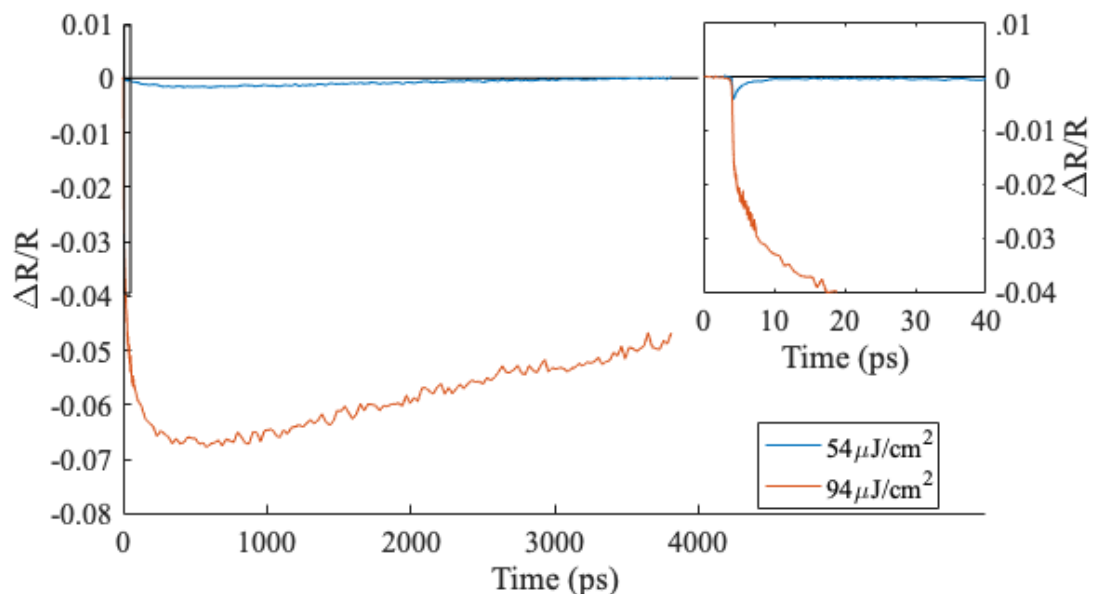


Figure 6.13: 1.55eV pump and probe on the 30nm VO₂ sample on TiO₂:Nb for low fluences. Time responses for various fluences from 0 to 4000ps are shown. The insert at top right shows times from 0 to 40ps which corresponds to the first 1% of the data and the area of the insert is represented by the small box seen at t=0. The vertical scale of the insert directly aligns with the corresponding main $\Delta R/R$ scale.

to the front of the sample, and the lower pump photon energy, 1.55 eV) will have a more “uniform” penetration of the sample throughout its thickness.

6.7 Conclusion

Our studies demonstrated that 3.1 eV ultrafast pulses can efficiently photo induce IMT in thin film samples of VO₂ grown on TiO₂ and TiO₂:Nb substrates at fluence values orders of magnitude lower (20μJ/cm² vs 10mJ/cm²) than what is typically required by an IR pump. Our pump probe measurements of the relative reflectivity $\Delta R/R$ revealed the unexpectedly rich dynamics of the film’s optical response due to the evolution of the VO₂ metallic fraction through the film thickness, indicating qualitative agreement between the experiment and a simple model based on a diffusion type transition dynamics coupled with a 4×4 optical matrix method. Due to its strong pump fluence dependence, this mechanism can provide additional tools for all-optical control of VO₂-based photonic devices. The addition of Nb dopant to the substrate improved the magnitude of the $\Delta R/R$ response of thin film VO₂, as well as increased the rate of change in both the slow growth and relaxation stages and increased sensitivity to the pump fluence. These properties illustrate the advantage of using Nb-doped TiO₂ substrates, not only for VO₂-based photodetectors, but also for ultrafast IMT applications.

Finally, when 30 nm VO₂ on TiO₂ was pumped at 1.55 eV, it showed differences when compared to the 3.1 eV pumped scans. Notably, the IMT

transition threshold was closer to three times higher than for 3.1eV pump. Another interesting effect was that 1.55 eV pump energy did not cause the zero-crossing seen at the higher pump energy, indicative of the 1.55 eV pump causing the transition more uniformly throughout the thickness of the sample so that interference affects were mitigated.

CHAPTER 7

VO₂ TiO₂:Nb Photocurrent Generation Dynamics

Study of VO₂ on TiO₂:Nb were spurred by a requirement to make more quantum efficient and compact photo detectors in the UV range. Typical neutron and gamma ray detectors utilize a scintillator material to convert radiation into UV and visible radiation and the photomultiplier tube converts the UV and visible radiation into an amplified electrical signal. Photomultiplier tubes require high voltage power supplies to operate, which are large in size, weight, and power consumption. The need for high quantum efficiency detectors stems from the need to replace bulky electronics and photomultiplier tubes in neutron and gamma radiation measurements. [123] The photodetector needs to have high quantum efficiency to efficiently detect neutron and gamma radiation with a scintillator to have a chance of detecting the scintillator output light. There is work being done in the development of UV photodetectors using semiconductors [124-127]. VO₂ on TiO₂:Nb is an ideal choice of material to study due to its reported high quantum efficiency(EQE) [79].

7.1 Measurement of Photocurrent Switching Speed with Blue Light

VO₂ on TiO₂:Nb was first reported to exhibit current generation by Muraoka in 2002 [128]. He showed that the illumination of the sample with UV light produced an electric current. The VO₂ high quantum efficiency was first measured and reported by Creeden [79] in 2019. In these measurements, 405 nm or 254 nm light was used to generate a photocurrent in the sample. Creeden showed that optimized

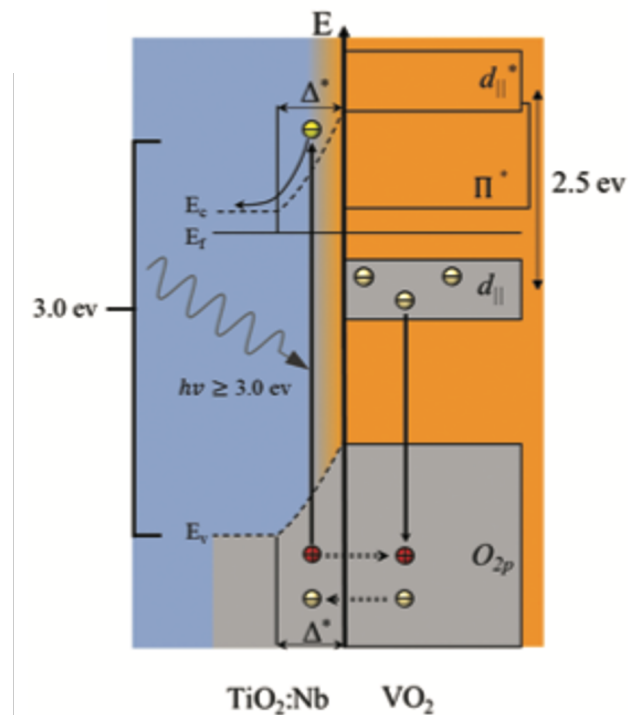


Figure 7.1: From [79] shows the modified band structure at the heterostructure region of the VO₂ on TiO₂:Nb. The generation of photocurrent process is also depicted. The Δ^* is the heterojunction region of the sample, E_f is the fermi energy of the system, E_c is the conduction band of the TiO₂. and E_v is the valence band of the TiO₂. The red spheres represent holes and the yellow are carriers.

heterostructures made with VO₂ films of different thicknesses on TiO₂:Nb reached external quantum efficiencies of 5000% at a photon energy of 3.06 eV(405 nm) and higher EQE values of 17000% at 4.88 eV (254 nm). The high EQE is attributed to a space-charge region that forms at the heterojunction between the two materials. The space-charge region also has an electric field that inhibits the photocarrier recombination that allows the carriers to be pushed deeper into the substrate which helps with the generation of the photocurrent [79].

The explanation for the high EQE was attributed to the heterostructure that forms between the TiO₂:Nb and VO₂ [79]. The presence of Nb in the TiO₂ substrate distorted the band energy, (Fig. 7.1). The generation of photocurrent in

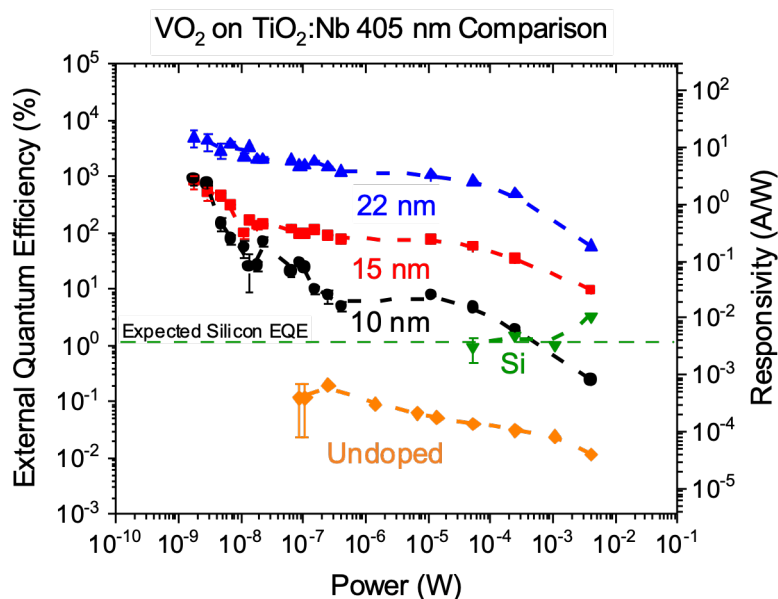


Figure 7.2: From [79] External quantum efficiency on the left vertical axis and the responsivity of the right (responsivity is defined as the current generated per of input light power) which is the gain of the system. The samples are 22nm (blue), 15nm (red), and 10nm on TiO₂:Nb. The orange line is VO₂ on plan TiO₂. The green line is Si photodiode response.

the sample as described by [79] can be thought of as a multi-step process where photons excited photoelectrons in TiO_2 along with creating holes in the conduction band of the TiO_2 . The photoelectrons excited into the $\text{TiO}_2\text{:Nb}$ conduction band can then diffuse deeper into the $\text{TiO}_2\text{:Nb}$ substrate, delaying recombination. The holes in the $\text{TiO}_2\text{:Nb}$ valence band can migrate into the VO_2 O_{2p} band, in the valence band of the VO_2 . With the hole migrating into the O_{2p} band of the VO_2 band, free carriers are formed from the $d_{||}$ band and recombine with the holes thus generating a photocurrent.

For time constant measurements of photocurrent done here, it was decided to keep the light location in the same area on the sample. No bias was applied on the sample for these measurements. The 22 nm sample was chosen because of its high external quantum efficiency according to Fig. 7.2, Creeden [79]. The high quantum efficiency could be advantageous for the generation of photocurrent coupled with the knowledge of the sample's measured photo induced IMT processes (section 6.5.2.).

Testing for photocurrent time rates involves a similar set-up to that used for the quantum efficiency measurement by Creeden [78, 79, 129], but with some changes in the detection equipment. A simple experimental setup can be seen in Figure 7.3. The photocurrent was detected using copper beryllium van der Pauw probes. The changes to the previous apparatus for detecting photocurrent

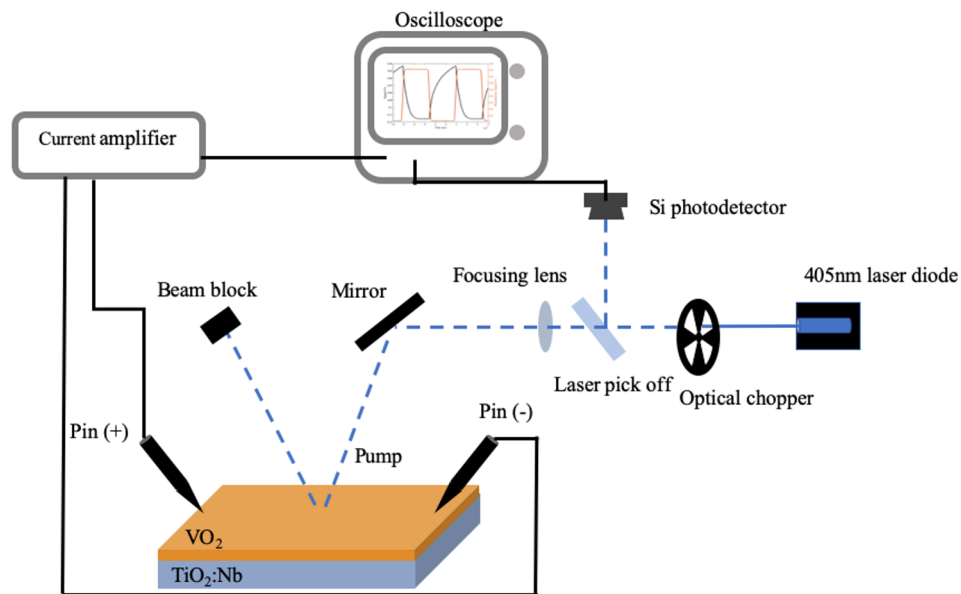


Figure 7.3: Simple figure of the modified photocurrent generation set up used to obtain the time constants. The setup is based on what Creeden used in the photocurrent efficiency measurements.

generation included the addition of an optical chopper to modulate the light pulses so that an oscilloscope could be used to detect time variation of the photocurrent generated. The chopper ran at a 50% duty factor and was run at 100Hz for testing. A 405 nm diode laser was used to illuminate the sample. The laser power was kept constant for these measurements at a power level of 6.2 mW.

A current amplifier was used to amplify the current generated in the sample. Its output was connected to the oscilloscope. The current amplifier's input was set at a low impedance to shunt the current into the amplifier and the gain was set at a low gain range. A light pickoff was used to send a fraction of the 405nm light into a Si photodiode to monitor the diodes output power

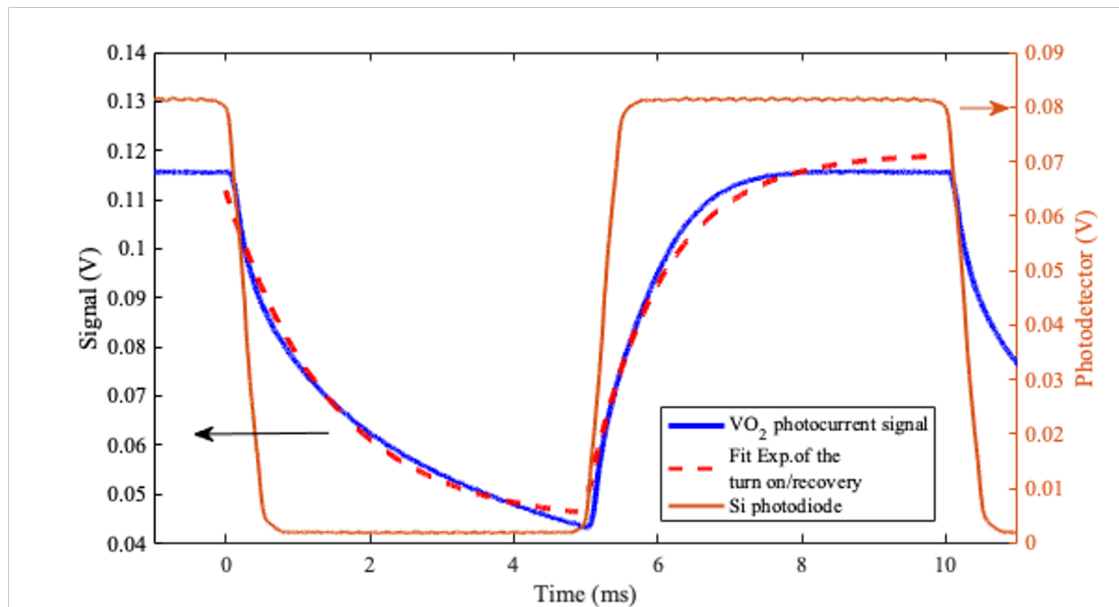


Figure 7.4: The photocurrent response of the 22nm VO_2 on $\text{TiO}_2\text{:Nb}$ sample using the pin location of 1.3mm. The blue line is the VO_2 photocurrent signal the dashed red lines are the single exp. fits of the photocurrent turn-on and recovery responses. The orange line is the Si photodiode pick off response and its axis is on the right.

The typical time response of the samples is seen in Fig. 7.4. The chopper was modulated at 100 Hz and the Si photo detector signal appears as a square wave. To find turn-on and turn-off time constants, a simple exponential curve was fitted to voltage response from the oscilloscope for both the turn-on and turn-off responses. Those fits are displayed as the red dashed lines in Fig. 7.4.

One variable that changed was the pin separation on the sample which varied from 0.65 mm to 2.2 mm. The change of the pin location had multiple effects on photocurrent generation. It changed the amplitudes of the measured voltage generated by the light. It also increased dark current generation as pin separation

was decreased. Pin location, with respect to the light beam, affected the turn-on rate and recovery rate. When pins were spaced far apart, the turn-on and turn-off time constants were slightly slower, and as the pins were brought closer together the time constants decreased slightly. The turn-on time constants for the VO₂ photocurrent were also faster than the recovery constants of the VO₂ photocurrent. The turn-on time and recovery time constants are plotted in Fig. 7.5. The turn-on time constants varied between 1.1 ms to 0.73 ms. The recovery time constants ranged from 2.13 ms to 1.41 ms

The signal had a positive voltage with the light adjacent to one of the pins, which reversed when the light was adjacent to the other pin. Midway between the

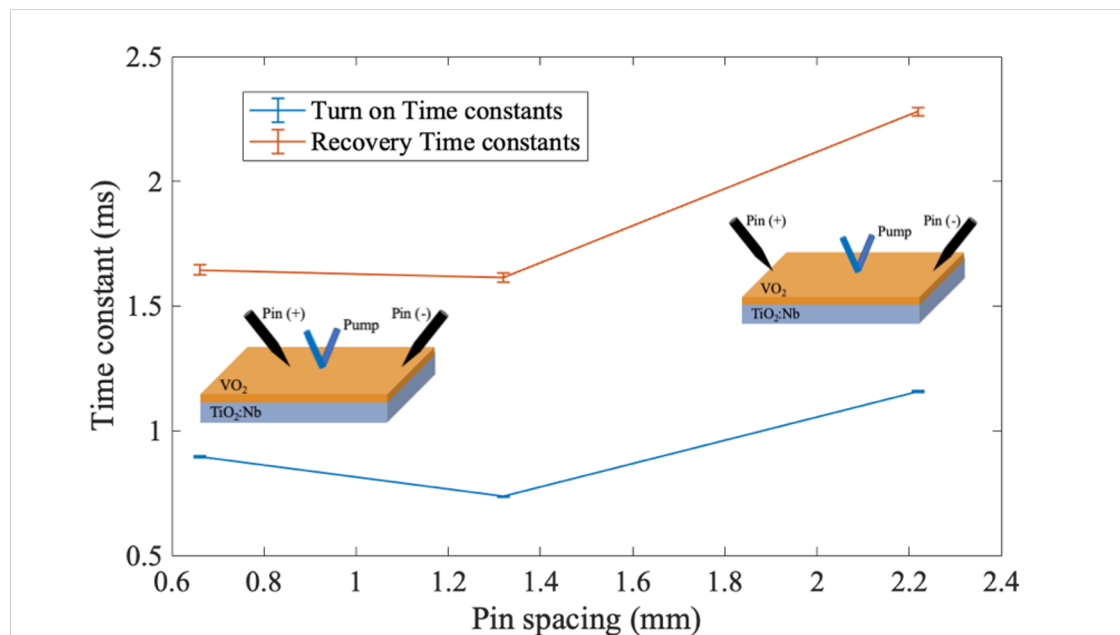


Figure 7.5: The time constant from the fitting applied to the VO₂ photocurrent response of the 22nm VO₂ on TiO₂:Nb sample for the different pin spacing. The blue line turn on response and the red line is the recovery time constant.

pins, the voltage read as zero. A possible explanation of this phenomenon was that the VO₂ on TiO₂:Nb sample's photocurrent was causing a charge separation across the sample thickness, which would be across the heterojunction. Hence with the beam's proximity to the positive pin vs. the negative pin would cause the voltage to reverse.

It is clear from the time constants measured here that the physical properties of the circuit are dominating any time constants of the photocurrent generation and recovery. The photoinduced IMT processes look at changes in the optical properties of the VO₂ over a very small region. The difference in the recovery rates of the photocurrent measurements are over six orders of magnitude slower than the VO₂ photoinduced IMT requiring tens of nanoseconds. The difference in the processes reflects that the photo induced process changes the optical properties and also changes electron bands from insulating to a metallic state. Photocurrent generation deals with electronic transport through a volume of VO₂ material. This system has resistance and capacitance that determine the times constants seen in Fig. 7.5. Creeden [38] measured high sheet resistance for the VO₂ samples. This represents a significant amount of impedance in the circuit. Furthermore, electron mobility is affected by the surface of the sample [130]; Transit and diffusion times of carriers and holes through the heterojunction depletion region are factors that are limiting the speed of the system.

A VO₂ on TiO₂:Nb sample can be engineered to be more like a photodiode by making a sample in a small package with contacts being made across the heterojunction (VO₂ to TiO₂:Nb) so that the surface resistance and capacitance effect of the system would be lower and thus could be generating a faster response.

Chapter 8

Conclusion and Outlook

8.1 Conclusion

This thesis reports on studies of the photo optical responses on the dynamics of thin films of VO₂ grown on various substrates. There were several types of optical measurements performed.

This work reports the first demonstration of the IMT in VO₂ induced by enhanced E-fields using surface plasmons. In addition, a surface plasmon resonant technique was adapted to allow the simultaneous monitoring of the IMT in VO₂ films. By using a low power laser, the IMT was shown to be not thermal, but rather electronic in nature. These observed results were supported by numerical calculations.

Further work on VO₂ IMT focused on the ultrafast photo induced process using 3.1eV photons to investigate the potential of using a heterostructure of VO₂ films grown on TiO₂ and Nb doped TiO₂ substrates for fast photodetectors in blue/UV spectral range. This work compared the IMT characteristics for VO₂ on doped substrates of TiO₂:Nb compared to VO₂ on plain undoped TiO₂. The results confirmed the advantages of using the doped substrate by improving the

temporal and reflection response rates of the samples. A model was developed to explain the complex response seen in the $\Delta R/R$ response of samples pumped at 3.1 eV. The model treated the IMT process as a stratification of insulator and metal layers diffusing the IMT process through the samples thickness capturing fundamental features of the IMT growth process. Finally, the comparison of the time responses of various thickness of VO₂ films on the doped substrates were explored.

In previous work, Creeden [79] indicated that VO₂ photocurrents exhibited high quantum efficiency. The time responses of photocurrent generation turn-on and recovery rates in the quantum efficient sample were on the order of ms.

8.2 Outlook

The benefits of utilizing surface plasmons to induce the IMT in VO₂ open up the potential for an all optical rapid switching mirror that could be the basis of advanced phased mirror array control and beam steering by modulating the VO₂'s reflectivity. Future work on this technique might be to engineer better samples with geometry parameters to try to improve signal to noise sensitivity.

Ultrafast photoinduced IMT in VO₂ on TiO₂ and TiO₂:Nb substrates when pumped by 3.1 eV photons showed areas to explore in more detail. It would be advantageous to monitor the $\Delta R/R$ response over a larger range of photon energies to obtain a more complete picture of the dynamics of the system as it is

excited throughout the IMT. Additionally, it would be useful to optimize the sensitivity response by studying additional dopants and dopant levels in the substrate.

Clearly, advances in UV and radiation detectors are strategically important to the United States. Continued efforts to improve the sensitivity and response rate of such detectors is valuable. Work to improve VO₂'s sensitivity, response and recovery rates are still needed to give engineers the tools to build better instruments for use in space and ground detector systems.

Appendix A

Ellipsometry

Ellipsometry helps obtain the optical and dielectric properties of a material over a range of wavelengths. The basics of ellipsometry are that the complex reflectance ratio called ρ of a sample is measured. ρ is defined as r_p/r_s [131, 132] where r_p is the reflectance of the p polarized light and r_s is the reflectance of the s polarized light. This complex reflectance ratio can be parametrized by the amplitude component Ψ along with the phase difference Δ .

$$\tan \Psi e^{i\Delta} \tag{A.1}$$

This complex reflectance ratio can be related to the reflection coefficients for a 3-layer system as follows:

$$\tan \Psi e^{i\Delta} = \frac{r_{p12} + r_{p23} e^{-2i\delta}}{1 + r_{p12} r_{p23} e^{-2i\delta}} \cdot \frac{1 + r_{s12} r_{s23} e^{-2i\delta}}{r_{s12} + r_{s23} e^{-2i\delta}} \tag{A.2}$$

The r_p and r_s terms represent the reflection coefficients for s and p polarizations at boundary layers 1 to 2 or 2 to 3, and the δ in the exponential is expressed in the following equation:

$$\delta = \frac{2\pi}{\lambda} n_2 d \cos \phi_2 \tag{A.3}$$

n_2 is the refractive index of the sample, d is the thickness of the film, λ is the wavelength, and ϕ_2 is the incident angle of the light on the sample.

To obtain the real and imaginary dielectric terms for the sample, the WVASE program allows the user to assume one or more of several physically realistic distribution-type equations as the user feels is appropriate to represent the imaginary part of the dielectric function [132]. In our case we used the Tauc-Lorentz oscillator (TLO) for our distributions [133]:

$$\varepsilon_2(E) = \left[\frac{AE_0C(E-E_g)^2}{(E^2-E_0^2)^2+C^2E^2} \cdot \frac{1}{E} \right], \quad E > E_g \quad (\text{A.4})$$

A is the strength (amplitude) of the Tauc-Lorentz energy peak, C is a broadening term (width), for the peak, E_0 is the peak central photon energy, and E_g is the energy of the optical gap. Finally, the equation requires the condition that:

$$\varepsilon_2(E) = 0, \quad E \leq E_g \quad (\text{A.5})$$

In principle, one can then compute an ε_2 term using the chosen TLO equation and from that equation one can compute the ε_1 term using the Kramers-Kronig relationship:

$$\varepsilon_1(E) = \varepsilon_1(\infty) + \frac{2}{\pi} P \int_{E_g}^{\infty} \frac{\xi \varepsilon_2(\xi)}{\xi^2 - E^2} d\xi, \quad (\text{A.6})$$

Here P stands for the Cauchy principal part used in the integral, $\varepsilon_1(\infty)$ is the dielectric function assumed for infinite frequency which is a fitting parameter in this equation, and the integral is taken over the range of the minimum energy E_g to infinity. The computer program uses a non-linear optimization algorithm to find the corresponding $\varepsilon_1(E)$ over the photon energy range of interest. Using these

forms for the dielectric properties, the program uses these terms to compute $\tan \Psi e^{i\Delta}$ from the reflection terms in equation (2.4). The user gives the program initial values and the computer calculates the optimum estimates for $\varepsilon_1(E)$ and $\varepsilon_2(E)$.

The TLO form for ε_1 , ε_2 , was used because the TLO bests represents the actual band structure types found in our sample section 4.2.4. A number of TLOs could be used to best represent the expected insulator case for the VO₂ band structure. Once an equation that represents the ε_2 term is found, then one has an understanding of the band structure of the system.

Appendix B

Computational methods

B.1 Finite difference time domain (FDTD)

An efficient method for computing E&M fields in structures is the FDTD simulation. An FDTD model was undertaken for simulation of the SPR system used. EM Explorer was the program used. The simple basics of the method is that

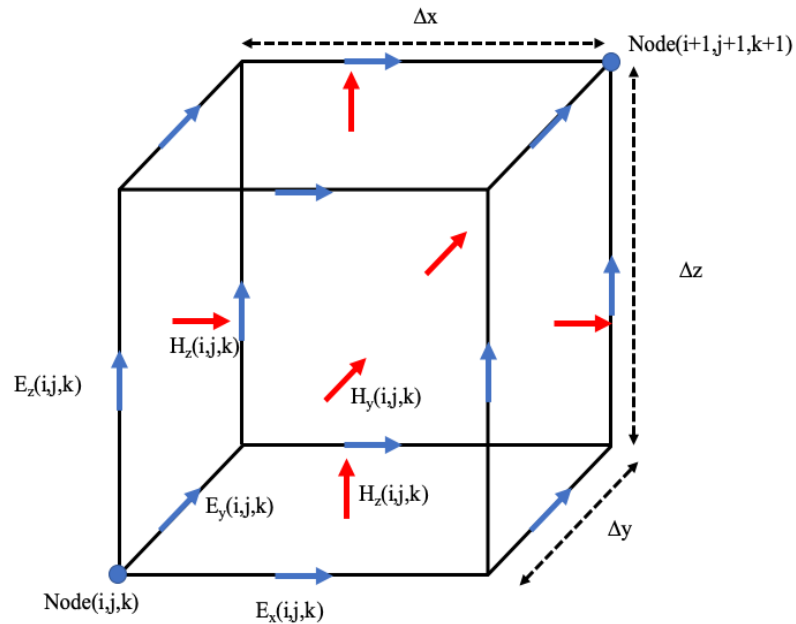


Fig B.1: The Yee Cell Figure shows field geometries that are calculated cell by cell through the mesh that represents the structure under study. This cell type lends itself to efficient finite difference computations of the Maxwell equations.

it discretizes Maxwell's equations using 3D cells of a finite volume. Typically, this cell is called the Yee cell, named after Kanen Yee (see Fig B.16). Yee cells are

known to be very computationally efficient when applied to Maxwell's equations [134].

$$\nabla \times \vec{E} = -\frac{\partial \vec{B}}{\partial t} - \vec{M} , \quad (\text{B.1})$$

and

$$\nabla \times \vec{H} = -\frac{\partial \vec{D}}{\partial t} + \vec{J} . \quad (\text{B.2})$$

Where \mathbf{E} and \mathbf{H} are the electric and magnetic field, \mathbf{D} and \mathbf{B} are the electric and magnetic flux densities and \mathbf{J} and \mathbf{M} are the volume electric and magnetic current densities. Their properties are defined as $\vec{D} = \epsilon \vec{E}$, $\vec{B} = \mu \vec{H}$, $\vec{J} = \sigma \vec{E}$, and $\vec{M} = \sigma_m \vec{H}$, where ϵ is the permittivity and μ is the permeability, σ is the electric conductivity, and σ_m magnetic conductivity.

In a lossless medium these equations can be rewritten as:

$$\frac{\partial \vec{H}}{\partial t} = -\frac{1}{\mu} \nabla \times \vec{E} \quad (\text{B.3})$$

$$\frac{\partial \vec{E}}{\partial t} = \frac{1}{\epsilon} \nabla \times \vec{H} \quad (\text{B.4})$$

The equations for the three components of the H fields are written below:

$$H_x^{n+\frac{1}{2}}(i, j, k) = H_x^{n-\frac{1}{2}}(i, j, k) + \frac{\Delta t}{\mu(i, j, k)} \left[\frac{E_y^n(i, j, k+1) - E_y^n(i, j, k)}{\Delta z} - \frac{E_z^n(i, j+1, k) - E_z^n(i, j, k)}{\Delta y} \right] \quad (\text{B.5})$$

$$H_y^{n+\frac{1}{2}}(i, j, k) = H_y^{n-\frac{1}{2}}(i, j, k) + \frac{\Delta t}{\mu(i, j, k)} \left[\frac{E_z^n(i+1, j, k) - E_z^n(i, j, k)}{\Delta x} - \frac{E_x^n(i, j, k+1) - E_x^n(i, j, k)}{\Delta z} \right] \quad (\text{B.6})$$

$$H_z^{n+\frac{1}{2}}(i, j, k) = H_z^{n-\frac{1}{2}}(i, j, k) + \frac{\Delta t}{\mu(i, j, k)} \left[\frac{E_x^n(i, j+1, k) - E_x^n(i, j, k)}{\Delta y} - \frac{E_y^n(i+1, j, k) - E_y^n(i, j, k)}{\Delta x} \right] \quad (\text{B.7})$$

The equations for the three components of the E fields are:

$$E_x^{n+\frac{1}{2}}(i, j, k) = E_x^n(i, j, k) + \frac{\Delta t}{\varepsilon(i, j, k)} \left[\frac{H_z^{n+\frac{1}{2}}(i, j, k) - H_z^{n+\frac{1}{2}}(i, j-1, k)}{\Delta y} - \frac{H_y^{n+\frac{1}{2}}(i, j, k) - H_y^{n+\frac{1}{2}}(i, j, k-1)}{\Delta z} \right] \quad (\text{B.8})$$

$$E_y^{n+\frac{1}{2}}(i, j, k) = E_y^n(i, j, k) + \frac{\Delta t}{\varepsilon(i, j, k)} \left[\frac{H_x^{n+\frac{1}{2}}(i, j, k) - H_x^{n+\frac{1}{2}}(i, j, k-1)}{\Delta z} - \frac{H_z^{n+\frac{1}{2}}(i, j, k) - H_z^{n+\frac{1}{2}}(i-1, j, k)}{\Delta x} \right] \quad (\text{B.9})$$

$$E_z^{n+\frac{1}{2}}(i, j, k) = E_z^n(i, j, k) + \frac{\Delta t}{\varepsilon(i, j, k)} \left[\frac{H_y^{n+\frac{1}{2}}(i, j, k) - H_y^{n+\frac{1}{2}}(i-1, j, k)}{\Delta x} - \frac{H_x^{n+\frac{1}{2}}(i, j, k) - H_x^{n+\frac{1}{2}}(i, j-1, k)}{\Delta y} \right] \quad (\text{B.10})$$

When computing real materials with losses one needs to include in the solutions for the electric displacement component, D , and the magnetic induction component, B of Maxwell's equations.

Computationally, this is a very efficient process for computers to perform, especially for complex structures.

In commercial FDTD packages, they include optimization for perfectly matched layers (PDL), which avoids the need to compute infinite mediums. The PDL's help handle the termination or boundary of a structure using an absorbing media rather than dealing with the concept of an infinite media, which is frequently assumed in theoretical discussions.

B.2. 4×4 optical matrix method

General theory of E&M wave propagation in layer media can normally be given by the 2×2 matrix method, which was first put forth by Abelé [135]. The 2×2 method works well for isotropic layered media but will not handle anisotropic layered media. To handle the more complex situation of anisotropic layered media one can use a 4×4 matrix method proposed by Yeh [136]. While this method is more complex than the 2x2 matrix method, it works well with monochromatic light and more advanced materials. The process starts with a dielectric permittivity tensor ε given by the following equation which represents layers with different optical properties.

$$\varepsilon = \begin{cases} \varepsilon(0), z < z_0 \\ \varepsilon(1), z_0 < z < z_1 \\ \varepsilon(2), z_1 < z < z_2 \\ \vdots \\ \varepsilon(N), z_{N-1} < z < z_N \\ \varepsilon(s), z_N < z \end{cases} \quad (\text{B.11})$$

The electric field distribution within each layer is a sum of four partial waves with the complex amplitudes of the waves becoming a column vector. The A matrix represents a coordinate rotation matrix of a unit circle in spherical coordinates. There are four solutions to the electric field equation denoted by $\sigma = 1,2,3,4$, for the four $A_\sigma(n)$'s,. The E fields are:

$$\mathbf{E} = \sum_{\sigma=1}^4 A_\sigma(n) \hat{p}_\sigma(n) e^{i[\alpha x + \beta y + \gamma_\sigma(n)(z-z_n) - \omega t]} \quad (\text{B.12})$$

The magnetic field distribution for the layer will have the following form:

$$\mathbf{H} = \sum_{\sigma=1}^4 A_\sigma(n) \hat{q}_\sigma(n) e^{i[\alpha x + \beta y + \gamma_\sigma(n)(z-z_n) - \omega t]} \quad (\text{B.13})$$

with $\hat{q}_\sigma(n) = (c\mathbf{k}_\sigma(n)/\omega\mu) \times \hat{p}_\sigma(n)$.

$\hat{q}_\sigma(n)$ are not unit vectors at this point. The wave number vector is

$$\mathbf{k}_\sigma(n) = \alpha\hat{x} + \beta\hat{y} + \gamma_\sigma(n)\hat{z} \quad (\text{B.14})$$

If continuity is applied to the E and H field on the x and y component at the $Z = Z_{n+1}$. It will lead to the following equations:

$$\sum_{\sigma=1}^4 A_\sigma(n-1)\hat{\mathbf{p}}_\sigma(n-1) \cdot \hat{x} = \sum_{\sigma=1}^4 A_\sigma(n)\hat{\mathbf{p}}_\sigma(n) \cdot \hat{x} e^{[-i\gamma_\sigma(n)t_n]} \quad (\text{B.15})$$

$$\sum_{\sigma=1}^4 A_\sigma(n-1)\hat{\mathbf{p}}_\sigma(n-1) \cdot \hat{y} = \sum_{\sigma=1}^4 A_\sigma(n)\hat{\mathbf{p}}_\sigma(n) \cdot \hat{y} e^{[-i\gamma_\sigma(n)t_n]} \quad (\text{B.16})$$

$$\sum_{\sigma=1}^4 A_\sigma(n-1)\hat{\mathbf{q}}_\sigma(n-1) \cdot \hat{x} = \sum_{\sigma=1}^4 A_\sigma(n)\hat{\mathbf{q}}_\sigma(n) \cdot \hat{x} e^{[-i\gamma_\sigma(n)t_n]} \quad (\text{B.17})$$

$$\sum_{\sigma=1}^4 A_\sigma(n-1)\hat{\mathbf{q}}_\sigma(n-1) \cdot \hat{y} = \sum_{\sigma=1}^4 A_\sigma(n)\hat{\mathbf{q}}_\sigma(n) \cdot \hat{y} e^{[-i\gamma_\sigma(n)t_n]} \quad (\text{B.18})$$

The exp can be simplify as $t_n = z_n - z_{n-1}$ $n=1,2,\dots,N$. Now these equations

can be written as a matrix

$$\begin{pmatrix} A_1(n-1) \\ A_2(n-1) \\ A_3(n-1) \\ A_4(n-1) \end{pmatrix} = \mathbf{D}^{-1}(n-1)\mathbf{D}(n)\mathbf{P}(n) \begin{pmatrix} A_1(n) \\ A_2(n) \\ A_3(n) \\ A_4(n) \end{pmatrix} \quad (\text{B.19})$$

The \mathbf{D} matrix is the following

$$\mathbf{D}(n) = \begin{pmatrix} \hat{x} \cdot \hat{\mathbf{p}}_1(n) & \hat{x} \cdot \hat{\mathbf{p}}_2(n) & \hat{x} \cdot \hat{\mathbf{p}}_3(n) & \hat{x} \cdot \hat{\mathbf{p}}_4(n) \\ \hat{y} \cdot \hat{\mathbf{q}}_1(n) & \hat{y} \cdot \hat{\mathbf{q}}_2(n) & \hat{y} \cdot \hat{\mathbf{q}}_3(n) & \hat{y} \cdot \hat{\mathbf{q}}_4(n) \\ \hat{y} \cdot \hat{\mathbf{p}}_1(n) & \hat{y} \cdot \hat{\mathbf{p}}_2(n) & \hat{y} \cdot \hat{\mathbf{p}}_3(n) & \hat{y} \cdot \hat{\mathbf{p}}_4(n) \\ \hat{x} \cdot \hat{\mathbf{q}}_1(n) & \hat{x} \cdot \hat{\mathbf{q}}_2(n) & \hat{x} \cdot \hat{\mathbf{q}}_3(n) & \hat{x} \cdot \hat{\mathbf{q}}_4(n) \end{pmatrix} \quad (\text{B.20})$$

$$\mathbf{P}(n) = \begin{pmatrix} e^{[-i\gamma_1(n)t_n]} & 0 & 0 & 0 \\ 0 & e^{[-i\gamma_2(n)t_n]} & 0 & 0 \\ 0 & 0 & e^{[-i\gamma_3(n)t_n]} & 0 \\ 0 & 0 & 0 & e^{[-i\gamma_4(n)t_n]} \end{pmatrix} \quad (\text{B.21})$$

The $\mathbf{D}(n)$ matrices are dynamical due to the fact that they will depend on the direction of polarization of the four partial waves. The $\mathbf{P}(n)$ are the propagation matrices and will depend on the phase excursion of the four waves. When the $\mathbf{D}(n)$ and $\mathbf{P}(n)$ matrices are multiplied together it will give a transfer matrix which is defined as

$$\mathbf{T}_{n-1,n} = \mathbf{D}^{-1}(n-1)\mathbf{D}(n)\mathbf{P}(n) \quad (\text{B.22})$$

These values can be seen from ref [137], which will makes the above equation.

$$\begin{pmatrix} A_1(n-1) \\ A_2(n-1) \\ A_3(n-1) \\ A_4(n-1) \end{pmatrix} = \mathbf{T}_{n-1,n} \begin{pmatrix} A_1(n) \\ A_2(n) \\ A_3(n) \\ A_4(n) \end{pmatrix} \quad (\text{B.23})$$

Therefore, the equation for a number of layers, s , goes to the following:

$$\begin{pmatrix} A_1(0) \\ A_2(0) \\ A_3(0) \\ A_4(0) \end{pmatrix} = \mathbf{T}_{0,1}\mathbf{T}_{1,2}\mathbf{T}_{2,3} \dots \mathbf{T}_{N-1,N}\mathbf{T}_{N,s} \begin{pmatrix} A_1(s) \\ A_2(s) \\ A_3(s) \\ A_4(s) \end{pmatrix} \quad (\text{B.24})$$

From the theory, what is needed is the reflectance R and transmittance T for a layered medium. To get R and T there will be 4 complex amplitudes for each component. With A_s being the s polarization of the incident light A_p being the p polarized incident light. B will be the reflected component with the same polarization subscript nomenclature as the incident light. Finally, the C terms on the right-hand side are the polarized transmission electric field amplitudes.

$$\begin{pmatrix} A_s \\ B_s \\ A_p \\ B_p \end{pmatrix} = \begin{pmatrix} M_{11} & M_{12} & M_{13} & M_{14} \\ M_{21} & M_{22} & M_{23} & M_{24} \\ M_{31} & M_{32} & M_{33} & M_{34} \\ M_{41} & M_{42} & M_{43} & M_{44} \end{pmatrix} \begin{pmatrix} C_s \\ 0 \\ C_p \\ 0 \end{pmatrix} \quad (\text{B.25})$$

The M matrix components in eq. (B.25) are the product of the transfer matrices T shown in eq. (B.24).

The reflection and transmission coefficients from the above matrix are given by the following equations:

$$r_{ss} = \left(\frac{B_s}{A_s} \right)_{A_p=0} = \frac{M_{21}M_{33} - M_{23}M_{31}}{M_{11}M_{33} - M_{13}M_{31}} \quad (\text{B.26})$$

$$r_{sp} = \left(\frac{B_p}{A_s} \right)_{A_p=0} = \frac{M_{41}M_{33} - M_{43}M_{31}}{M_{11}M_{33} - M_{13}M_{31}} \quad (\text{B.27})$$

$$r_{ps} = \left(\frac{B_s}{A_p} \right)_{A_s=0} = \frac{M_{11}M_{23} - M_{21}M_{13}}{M_{11}M_{33} - M_{13}M_{31}} \quad (\text{B.28})$$

$$r_{pp} = \left(\frac{B_p}{A_p} \right)_{A_s=0} = \frac{M_{11}M_{43} - M_{41}M_{13}}{M_{11}M_{33} - M_{13}M_{31}} \quad (\text{B.29})$$

$$t_{ss} = \left(\frac{C_s}{A_s} \right)_{A_p=0} = \frac{M_{33}}{M_{11}M_{33} - M_{13}M_{31}} \quad (\text{B.30})$$

$$t_{sp} = \left(\frac{C_p}{A_s} \right)_{A_p=0} = \frac{-M_{31}}{M_{11}M_{33} - M_{13}M_{31}} \quad (\text{B.31})$$

$$t_{ps} = \left(\frac{C_p}{A_p} \right)_{A_s=0} = \frac{-M_{13}}{M_{11}M_{33} - M_{13}M_{31}} \quad (\text{B.32})$$

$$t_{pp} = \left(\frac{C_p}{A_p} \right)_{A_s=0} = \frac{M_{11}}{M_{11}M_{33} - M_{13}M_{31}} \quad (\text{B.33})$$

Once one has the M matrices, one can compute the reflection and transmission for different polarizations of the optical system.

Although this is a lengthy process, the process is amenable to computer programming and allows for the modelling of the reflectance and transmission output of a complex layered system that can be undergoing optical property changes, plus it allows for different layer geometries to be tested.

Bibliography

1. J. B. Goodenough, "The two components of the crystallographic transition in VO₂," *Journal of Solid State Chemistry* **3**, 490-500 (1971).
2. M. Imada, A. Fujimori, and Y. Tokura, "Metal-insulator transitions," *Reviews of Modern Physics* **70**, 1039-1263 (1998).
3. F. J. Morin, "Oxides which show a metal-to-insulator transition at the neel temperature," *Physical Review Letters* **3**, 34-36 (1959).
4. H. W. Verleur, A. S. Barker, and C. N. Berglund, "Optical properties of VO₂ between 0.25 and 5 eV," *Physical Review* **172**, 788-798 (1968).
5. G. Stefanovich, A. Pergament, and D. Stefanovich, "Electrical switching and mott transition in VO₂," *Journal of Physics: Condensed Matter* **12**, 8837-8845 (2000).
6. G. Gopalakrishnan, D. Ruzmetov, and S. Ramanathan, "On the triggering mechanism for the metal-insulator transition in thin film VO₂ devices: electric field versus thermal effects," *Journal of Materials Science* **44**, 5345-5353 (2009).
7. Y. Zhou, X. Chen, C. Ko, Y. Zheng, C. Mouli, and S. Ramanathan, "Voltage-Triggered Ultrafast Phase Transition in Vanadium Dioxide Switches," *Electron Device Letters, IEEE* **34**, 220-222 (2013).
8. A. Joushaghani, B. A. Kruger, S. Paradis, D. Alain, J. S. Aitchison, and J. K. S. Poon, "Sub-volt broadband hybrid plasmonic-vanadium dioxide switches," *Applied Physics Letters* **102**, 061101 (2013).
9. A. Joushaghani, J. Jeong, S. Paradis, D. Alain, J. S. Aitchison, and J. K. S. Poon, "Voltage-controlled switching and thermal effects in VO₂ nano-gap junctions," *Applied Physics Letters* **104**, 221904 (2014).
10. L. Bai, Q. Li, S. A. Corr, Y. Meng, C. Park, S. V. Sinogeikin, C. Ko, J. Wu, and G. Shen, "Pressure-induced phase transitions and metallization in VO₂," *Physical Review B* **91**, 104110 (2015).
11. J. M. Braun, H. Schneider, M. Helm, R. Mirek, L. A. Boatner, R. E. Marvel, R. F. Haglund, and A. Pashkin, "Ultrafast response of photoexcited carriers in VO₂ at high-pressure," *New Journal of Physics* **20**, 083003 (2018).
12. J. Cao, E. Ertekin, V. Srinivasan, W. Fan, S. Huang, H. Zheng, J. W. L. Yim, D. R. Khanal, D. F. Ogletree, J. C. Grossman, and J. Wu, "Strain engineering and one-dimensional organization of metal-insulator domains in single-crystal vanadium dioxide beams," *Nature Nanotechnology* **4**, 732-737 (2009).
13. J. H. Park, J. M. Coy, T. S. Kasirga, C. Huang, Z. Fei, S. Hunter, and D. H. Cobden, "Measurement of a solid-state triple point at the metal-insulator transition in VO₂," *Nature* **500**, 431-434 (2013).
14. W. R. Roach and I. Balberg, "Optical induction and detection of fast phase transition in VO₂," *Solid State Communications* **9**, 551-555 (1971).

15. M. F. Becker, A. B. Buckman, R. M. Walser, T. Lépine, P. Georges, and A. Brun, "Femtosecond laser excitation of the semiconductor-metal phase transition in VO₂," *Applied Physics Letters* **65**, 1507-1509 (1994).
16. A. Cavalleri, M. Rini, H. H. W. Chong, S. Fourmaux, T. E. Glover, P. A. Heimann, J. C. Kieffer, and R. W. Schoenlein, "Band-Selective Measurements of Electron Dynamics in VO₂ Using Femtosecond Near-Edge X-Ray Absorption," *Physical Review Letters* **95**, 067405 (2005).
17. A. Cavalleri, T. Dekorsy, H. H. W. Chong, J. C. Kieffer, and R. W. Schoenlein, "Evidence for a structurally-driven insulator-to-metal transition in VO₂: A view from the ultrafast timescale," *Physical Review B* **70**, 161102 (2004).
18. A. Cavalleri, C. Tóth, C. W. Siders, J. A. Squier, F. Ráksi, P. Forget, and J. C. Kieffer, "Femtosecond structural dynamics in VO₂ during an ultrafast solid-solid phase transition," *Physical Review Letters* **87**, 237401 (2001).
19. D. Wegkamp, M. Herzog, L. Xian, M. Gatti, P. Cudazzo, C. L. McGahan, R. E. Marvel, R. F. Haglund, A. Rubio, M. Wolf, and J. Stähler, "Instantaneous band gap collapse in photoexcited monoclinic VO₂ due to photocarrier doping," *Physical Review Letters* **113**, 216401 (2014).
20. D. Wegkamp and J. Stähler, "Ultrafast dynamics during the photoinduced phase transition in VO₂," *Progress in Surface Science* **90**, 464-502 (2015).
21. S. Wall, S. Yang, L. Vidas, M. Chollet, J. M. Glowina, M. Kozina, T. Katayama, T. Henighan, M. Jiang, T. A. Miller, D. A. Reis, L. A. Boatner, O. Delaire, and M. Trigo, "Ultrafast disordering of vanadium dimers in photoexcited VO₂," *Science* **362**, 572-576 (2018).
22. D. L. Smith, *Thin-Film Deposition: Principles and Practice* 1st ed. (McGraw-Hill, 1995).
23. M. Ohring, "Chapter 1 - A Review of Materials Science," in *Materials Science of Thin Films (Second Edition)*, M. Ohring, ed. (Academic Press, San Diego, 2002), pp. 1-56.
24. M. Ohring, "Chapter 7 - Substrate Surfaces and Thin-Film Nucleation," in *Materials Science of Thin Films (Second Edition)*, M. Ohring, ed. (Academic Press, San Diego, 2002), pp. 357-415.
25. E. A. Casu, A. A. Müller, M. Fernández-Bolaños, A. Fumarola, A. Krammer, A. Schüller, and A. M. Ionescu, "Vanadium Oxide Bandstop Tunable Filter for Ka Frequency Bands Based on a Novel Reconfigurable Spiral Shape Defected Ground Plane CPW," *IEEE Access* **6**, 12206-12212 (2018).
26. S. Sengupta, K. Wang, K. Liu, A. K. Bhat, S. Dhara, J. Wu, and M. M. Deshmukh, "Field-effect modulation of conductance in VO₂ nanobeam transistors with HfO₂ as the gate dielectric," *Applied Physics Letters* **99**, 062114 (2011).
27. S. Savo, Y. Zhou, G. Castaldi, M. Moccia, V. Galdi, S. Ramanathan, and Y. Sato, "Reconfigurable anisotropy and functional transformations with VO₂ based metamaterial electric circuits," *Physical Review B* **91**, 134105 (2015).
28. E. A. Casu, W. A. Vitale, M. Tamagnone, M. M. Lopez, N. Oliva, A. Krammer, A. Schüller, M. Fernández-Bolaños, and A. M. Ionescu, "Shunt capacitive switches

- based on VO₂ metal insulator transition for RF phase shifter applications," in *2017 47th European Solid-State Device Research Conference (ESSDERC)*, (2017), 232-235.
29. E. Corti, B. Gotsmann, K. Moselund, A. M. Ionescu, J. Robertson, and S. Karg, "Scaled resistively-coupled VO₂ oscillators for neuromorphic computing," *Solid-State Electronics*, 107729 (2019).
 30. E. A. Casu, A. A. Muller, M. Cavalieri, A. Fumarola, A. M. Ionescu, and M. Fernandez-Bolaños, "A Reconfigurable Inductor Based on Vanadium Dioxide Insulator-to-Metal Transition," *IEEE Microwave and Wireless Components Letters* **28**, 795-797 (2018).
 31. N. I. Zheludev and Y. S. Kivshar, "From metamaterials to metadevices," *Nature Materials* **11**, 917-924 (2012).
 32. S. Chen, H. Ma, X. Yi, H. Wang, X. Tao, M. Chen, X. Li, and C. Ke, "Optical switch based on vanadium dioxide thin films," *Infrared Physics & Technology* **45**, 239-242 (2004).
 33. L. A. Sweatlock and K. Diest, "Vanadium dioxide based plasmonic modulators," *Opt. Express* **20**, 8700-8709 (2012).
 34. B. A. Kruger, A. Joushaghani, and J. K. S. Poon, "Design of electrically driven hybrid vanadium dioxide (VO₂) plasmonic switches," *Opt. Express* **20**, 23598-23609 (2012).
 35. M. A. Kats, R. Blanchard, S. Zhang, P. Genevet, C. Ko, S. Ramanathan, and F. Capasso, "Vanadium dioxide as a natural disordered metamaterial: perfect thermal emission and large broadband negative differential thermal emittance," *Physical Review X* **3**, 041004 (2013).
 36. M. Beebe, L. Wang, S. E. Madaras, J. M. Klopff, Z. Li, D. Brantley, M. Heimbürger, R. A. Wincheski, S. Kittiwatanakul, J. Lu, S. A. Wolf, and R. A. Lukaszew, "Surface plasmon resonance modulation in nanopatterned Au gratings by the insulator-metal transition in vanadium dioxide films," *Opt. Express* **23**, 13222-13229 (2015).
 37. S. E. Madaras, J. Creeden, S. Kittiwatanakul, J. Lu, I. Novikova, and R. A. Lukaszew, "Insulator to metal transition induced by surface plasmon polaritons in VO₂/Au thin films," *Opt. Express* **26**, 25657-25666 (2018).
 38. J. Creeden, "Growth Engineering and Characterization of Vanadium Dioxide Films for Ultraviolet Detection " PhD (The College of William & Mary Williamsburg 2020).
 39. N. D. M. Neil W. Ashcroft, *Solid State Physics* (Cengage Learning Delhi, 1976).
 40. N. F. Mott, "The Basis of the Electron Theory of Metals, with Special Reference to the Transition Metals," *Proceedings of the Physical Society. Section A* **62**, 416-422 (1949).
 41. N. Mott, *Metal-Insulator Transitions*, 1st ed. (CRC Press London, 1990).
 42. R. Peierls, *More Surprises in Theoretical Physics* Princeton Series in Physics (Princeton University Press Princeton, 1992).

43. R. M. Wentzcovitch, W. W. Schulz, and P. B. Allen, "VO₂: Peierls or Mott-Hubbard? A view from band theory," *Physical Review Letters* **72**, 3389-3392 (1994).
44. F. Grandi, A. Amaricci, and M. Fabrizio, "Unraveling the Mott-Peierls intrigue in vanadium dioxide," *Physical Review Research* **2**, 013298 (2020).
45. A. Zylbersztejn and N. F. Mott, "Metal-insulator transition in vanadium dioxide," *Physical Review B* **11**, 4383-4395 (1975).
46. Z. Shao, X. Cao, H. Luo, and P. Jin, "Recent progress in the phase-transition mechanism and modulation of vanadium dioxide materials," *NPG Asia Materials* **10**, 581-605 (2018).
47. S. Shin, S. Suga, M. Taniguchi, M. Fujisawa, H. Kanzaki, A. Fujimori, H. Daimon, Y. Ueda, K. Kosuge, and S. Kachi, "Vacuum-ultraviolet reflectance and photoemission study of the metal-insulator phase transitions in VO₂ V₆O₁₃ and V₂O₃," *Physical Review B* **41**, 4993-5009 (1990).
48. J. D. Budai, J. Hong, M. E. Manley, E. D. Specht, C. W. Li, J. Z. Tischler, D. L. Abernathy, A. H. Said, B. M. Leu, L. A. Boatner, R. J. McQueeney, and O. Delaire, "Metallization of vanadium dioxide driven by large phonon entropy," *Nature* **515**, 535 (2014).
49. L. Wang, I. Novikova, J. M. Klopf, S. Madaras, G. P. Williams, E. Madaras, J. Lu, S. A. Wolf, and R. A. Lukaszew, "Distinct Length Scales in the VO₂ Metal-Insulator Transition Revealed by Bi-chromatic Optical Probing," *Advanced Optical Materials* **2**, 30-33 (2014).
50. M. M. Qazilbash, M. Brehm, B.-G. Chae, P.-C. Ho, G. O. Andreev, B.-J. Kim, S. J. Yun, A. V. Balatsky, M. B. Maple, F. Keilmann, H.-T. Kim, and D. N. Basov, "Mott Transition in VO₂ Revealed by Infrared Spectroscopy and Nano-Imaging," *Science* **318**, 1750-1753 (2007).
51. M. Currie, V. D. Wheeler, B. Downey, N. Nepal, S. B. Qadri, J. A. Wollmershauser, J. Avila, and L. Nyakiti, "Asymmetric hysteresis in vanadium dioxide thin films," *Opt. Mater. Express* **9**, 3717-3728 (2019).
52. V. A. Klimov, I. O. Timofeeva, S. D. Khanin, E. B. Shadrin, A. V. Ilinskii, and F. Silva-Andrade, "Hysteresis loop construction for the metal-semiconductor phase transition in vanadium dioxide films," *Technical Physics* **47**, 1134-1139 (2002).
53. L. Kang, Y. Gao, Z. Zhang, J. Du, C. Cao, Z. Chen, and H. Luo, "Effects of Annealing Parameters on Optical Properties of Thermochromic VO₂ Films Prepared in Aqueous Solution," *The Journal of Physical Chemistry C* **114**, 1901-1911 (2010).
54. R. Lopez, T. E. Haynes, L. A. Boatner, L. C. Feldman, and R. F. Haglund, "Size effects in the structural phase transition of VO₂ nanoparticles," *Physical Review B* **65**, 224113 (2002).
55. C. Petit, J.-M. Frigerio, and M. Goldmann, "Hysteresis of the metal-insulator transition of ; evidence of the influence of microscopic texturation," *Journal of Physics: Condensed Matter* **11**, 3259-3264 (1999).

56. M. Nishikawa, T. Nakajima, T. Kumagai, T. Okutani, and T. Tsuchiya, "Adjustment of thermal hysteresis in epitaxial VO₂ films by doping metal ions," *Journal of the Ceramic Society of Japan* **119**, 577-580 (2011).
57. M. Nishikawa, T. Nakajima, T. Kumagai, T. Okutani, and T. Tsuchiya, "Ti-Doped VO₂ Films Grown on Glass Substrates by Excimer-Laser-Assisted Metal Organic Deposition Process," *Japanese Journal of Applied Physics* **50**, 01BE04 (2011).
58. M. Soltani, M. Chaker, E. Haddad, R. V. Kruzelecky, and J. Margot, "Effects of Ti-W codoping on the optical and electrical switching of vanadium dioxide thin films grown by a reactive pulsed laser deposition," *Applied Physics Letters* **85**, 1958-1960 (2004).
59. K. Shibuya, M. Kawasaki, and Y. Tokura, "Metal-insulator transition in epitaxial V_{1-x}W_xO₂ (0 ≤ x ≤ 0.33) thin films," *Applied Physics Letters* **96**, 022102 (2010).
60. J. Duchene, "Direct infrared measurements of filament transient temperature during switching in vanadium oxide film devices," *Journal of Solid State Chemistry* **12**, 303-306 (1975).
61. A. Mansingh and R. Singh, "The mechanism of electrical threshold switching in VO₂ crystals," *Journal of Physics C: Solid State Physics* **13**, 5725-5733 (1980).
62. J. K. Higgins, B. K. Temple, and J. E. Lewis, "Electrical properties of vanadate-glass threshold switches," *Journal of Non-Crystalline Solids* **23**, 187-215 (1977).
63. J. G. Zhang and P. C. Eklund, "The switching mechanism in V₂O₅ gel films," *Journal of Applied Physics* **64**, 729-733 (1988).
64. J. Bullot, O. Gallais, M. Gauthier, and J. Livage, "Threshold switching in V₂O₅ layers deposited from gels," *physica status solidi (a)* **71**, K1-K4 (1982).
65. Y. Taketa and R. Furugochi, "Switching and oscillation phenomena in SnO₂-VO_x-PdO ceramics," *Applied Physics Letters* **31**, 405-406 (1977).
66. R. L. Remke, R. M. Walser, and R. W. Bené, "The effect of interfaces on electronic switching in VO₂ thin films," *Thin Solid Films* **97**, 129-143 (1982).
67. F. Chudnovskii, "The metal-semiconductor phase transition in vanadium oxides and its technical application," *Zhurnal Tekhnicheskoi Fiziki* **45**, 1561-1583 (1975).
68. A. L. Pergament, P. P. Boriskov, A. A. Velichko, and N. A. Kuldin, "Switching effect and the metal-insulator transition in electric field," *Journal of Physics and Chemistry of Solids* **71**, 874-879 (2010).
69. A. Mansingh, R. Singh, and M. Sayer, "Dielectric behaviour of vanadium dioxide," *physica status solidi (a)* **49**, 773-779 (1978).
70. G. S. A. Pergament, and A. Velichko, "Oxide Electronics and Vanadium Dioxide Perspective: A Review " *Journal of Selected Topics in nano Electronics and Computing* **1**, 19 (2013).
71. P. Gibbon, *Short Pulse Laser interaction with Matter an Introduction* (Imperial College Press London 2005).
72. J. Shah, *Hot Carriers in Semiconductor Nanostructures: Physics and Applications*, 1st ed. (Academic Press, San Diego, CA, 1992), p. 508.

73. V. S. Vikhnin, S. Lysenko, A. Rua, F. Fernandez, and H. Liu, "The model of ultrafast light-induced insulator-metal phase transition in vanadium oxide," *Journal of Physics: Conference Series* **21**, 44-49 (2005).
74. S. Lysenko, A. J. Rua, V. Vikhnin, J. Jimenez, F. Fernandez, and H. Liu, "Light-induced ultrafast phase transitions in VO₂ thin film," *Applied Surface Science* **252**, 5512-5515 (2006).
75. M. van Veenendaal, "Ultrafast photoinduced insulator-to-metal transitions in vanadium dioxide," *Physical Review B* **87**, 235118 (2013).
76. X. Yuan, W. Zhang, and P. Zhang, "Hole-lattice coupling and photoinduced insulator-metal transition in VO₂," *Physical Review B* **88**, 035119 (2013).
77. C. Kübler, H. Ehrke, R. Huber, R. Lopez, A. Halabica, R. F. Haglund, and A. Leitenstorfer, "Coherent Structural Dynamics and Electronic Correlations during an Ultrafast Insulator-to-Metal Phase Transition in VO₂," *Physical Review Letters* **99**, 116401 (2007).
78. J. A. Creeden, S. E. Madaras, D. B. Beringer, M. R. Beebe, I. Novikova, and R. A. Lukaszew, "Structural and Photoelectric Properties of Epitaxially Grown Vanadium Dioxide Thin Films on c-Plane Sapphire and Titanium Dioxide," *Scientific Reports* **9**, 9362 (2019).
79. J. A. Creeden, S. E. Madaras, D. B. Beringer, I. Novikova, and R. A. Lukaszew, "Growth and Characterization of Vanadium Dioxide/Niobium Doped Titanium Dioxide Heterostructures for Ultraviolet Detection," *Advanced Optical Materials* **7**, 1901143 (2019).
80. H. Raether, *Surface Plasmons on Smooth and Rough Surfaces and on Gratings*, 1 ed., Springer Tracts in Modern Physics (Springer-Verlag, New York, 1988), p. 136.
81. H. J. Simon, D. E. Mitchell, and J. G. Watson, "Surface plasmons in silver films—a novel undergraduate experiment," *American Journal of Physics* **43**, 630-636 (1975).
82. J. Homola, I. Koudela, and S. S. Yee, "Surface plasmon resonance sensors based on diffraction gratings and prism couplers: sensitivity comparison," *Sensors and Actuators B: Chemical* **54**, 16-24 (1999).
83. I. Coherent, *Operator's Manual Mantis Modelocked Titanium:Sapphire Laser System* (Coherent Inc. , Santa Clara CA, 2008).
84. C. Rulliere, *Femtosecond Laser Pulses: Principles and Experiments* (Springer New York, 2007).
85. W. T. Silfvast, *Laser Fundamentals*, 2nd ed. (Cambridge University Press Cambridge UK, 2008), p. 642.
86. I. Coherent, *Legend Elite Operator's Manual Ultrafast Amplifier Laser Systems* (Coherent Santa Clara, CA 2010).
87. D. Strickland and G. Mourou, "Compression of amplified chirped optical pulses," *Optics communications* **56**, 219-221 (1985).
88. R. Paschotta, *Encyclopedia of Laser Physics and Technology*, 1st ed. (Wiley-VCH, 2008).
89. D. Nikogosyan, "Beta barium borate (BBO)," *Applied Physics A* **52**, 359-368 (1991).

90. ThorLabs, "High-Speed Fiber-Coupled Detectors " (Thorlabs, 2020), retrieved June 2020, https://www.thorlabs.com/newgrouppage9.cfm?objectgroup_id=1297.
91. G. S. Settles, "Toepler's Schlieren Technique," in *Schlieren and Shadowgraph Techniques: Visualizing Phenomena in Transparent Media* (Springer Berlin Heidelberg, Berlin, Heidelberg, 2001), pp. 39-75.
92. G. Binnig, C. F. Quate, and C. Gerber, "Atomic Force Microscope," *Physical Review Letters* **56**, 930-933 (1986).
93. W. Mal, "Fundamental Theory of Atomic Force Microscopy " (nanoscience.gatech.edu, 2011), retrieved 5/5/20, 2020, <http://www.nanoscience.gatech.edu/zlwang/research/afm.html>.
94. J. A. Creeden, S. E. Madaras, D. B. Beringer, I. Novikova, and R. A. Lukaszew, "Intrinsic anomalous scaling of epitaxial vanadium dioxide thin films on titanium dioxide," *AIP Advances* **9**, 095045 (2019).
95. M. Rodriguez-Vega, M. T. Simons, E. Radue, S. Kittiwatanakul, J. Lu, S. A. Wolf, R. A. Lukaszew, I. Novikova, and E. Rossi, "Effect of inhomogeneities and substrate on the dynamics of the metal-insulator transition in VO₂ thin films," *Physical Review B* **92**, 115420 (2015).
96. T. J. Huffman, P. Xu, A. J. Hollingshad, M. M. Qazilbash, L. Wang, R. A. Lukaszew, S. Kittiwatanakul, J. Lu, and S. A. Wolf, "Modification of electronic structure in compressively strained vanadium dioxide films," *Physical Review B* **91**, 205140 (2015).
97. E. Radue, E. Crisman, L. Wang, S. Kittiwatanakul, J. Lu, S. A. Wolf, R. Wincheski, R. A. Lukaszew, and I. Novikova, "Effect of a substrate-induced microstructure on the optical properties of the insulator-metal transition temperature in VO₂ thin films," *Journal of Applied Physics* **113**, 233104 (2013).
98. K. G. West, J. Lu, J. Yu, D. Kirkwood, W. Chen, Y. Pei, J. Claassen, and S. A. Wolf, "Growth and characterization of vanadium dioxide thin films prepared by reactive-biased target ion beam deposition," *Journal of Vacuum Science & Technology A: Vacuum, Surfaces, and Films* **26**, 133-139 (2008).
99. P. B. Johnson and R. W. Christy, "Optical constants of the noble metals," *Physical Review B* **6**, 4370-4379 (1972).
100. D. W. Berreman, "Optics in stratified and anisotropic media: 4×4-matrix formulation," *J. Opt. Soc. Am.* **62**, 502-510 (1972).
101. M. Liu, H. Y. Hwang, H. Tao, A. C. Strikwerda, K. Fan, G. R. Keiser, A. J. Sternbach, K. G. West, S. Kittiwatanakul, J. Lu, S. A. Wolf, F. G. Omenetto, X. Zhang, K. A. Nelson, and R. D. Averitt, "Terahertz-field-induced insulator-to-metal transition in vanadium dioxide metamaterial," *Nature* **487**, 345-348 (2012).
102. L. Wang, E. Radue, S. Kittiwatanakul, C. Clavero, J. Lu, S. A. Wolf, I. Novikova, and R. A. Lukaszew, "Surface plasmon polaritons in VO₂ thin films for tunable low-loss plasmonic applications," *Opt. Lett.* **37**, 4335-4337 (2012).
103. S. Kittiwatanakul, S. A. Wolf, and J. Lu, "Large epitaxial bi-axial strain induces a Mott-like phase transition in VO₂," *Applied Physics Letters* **105**, 073112 (2014).
104. E. Radue, L. Wang, S. Kittiwatanakul, J. Lu, S. A. Wolf, E. Rossi, R. A. Lukaszew, and I. Novikova, "Substrate-induced microstructure effects on the dynamics of the

- photo-induced metal-insulator transition in VO₂ thin films," *Journal of Optics* **17**, 025503 (2015).
105. B. Wu, A. Zimmers, H. Aubin, R. Ghosh, Y. Liu, and R. Lopez, "Electric-field-driven phase transition in vanadium dioxide," *Physical Review B* **84**, 241410 (2011).
 106. H. Reddy, U. Guler, A. V. Kildishev, A. Boltasseva, and V. M. Shalaev, "Temperature-dependent optical properties of gold thin films," *Opt. Mater. Express* **6**, 2776-2802 (2016).
 107. O. L. Muskens, L. Bergamini, Y. Wang, J. M. Gaskell, N. Zabala, C. H. de Groot, D. W. Sheel, and J. Aizpurua, "Antenna-assisted picosecond control of nanoscale phase transition in vanadium dioxide," *Light: Science & Applications* **5**, e16173 (2016).
 108. S. Chen, J. Liu, L. Wang, H. Luo, and Y. Gao, "Unraveling Mechanism on Reducing Thermal Hysteresis Width of VO₂ by Ti Doping: A Joint Experimental and Theoretical Study," *The Journal of Physical Chemistry C* **118**, 18938-18944 (2014).
 109. S. Lysenko, V. V., Z. Guotong, R. A., F. F. E, and L. Hau-ya, "Ultrafast optical dynamics in VO₂," in *SPIE Smart Structures and Materials + Nondestructive evaluation*, (2006).
 110. S. Lysenko, V. Vikhnin, G. Zhang, A. Rua, F. Fernandez, and H. Liu, "Insulator-to-metal phase transformation of VO₂ films upon femtosecond laser excitation," *Journal of Electronic Materials* **35**, 1866-1872 (2006).
 111. M. R. Beebe, J. M. Klopf, Y. Wang, S. Kittiwatanakul, J. Lu, S. A. Wolf, and R. A. Lukaszew, "Time-resolved light-induced insulator-metal transition in niobium dioxide and vanadium dioxide thin films," *Opt. Mater. Express* **7**, 213-223 (2017).
 112. T. L. Cocker, L. V. Titova, S. Fourmaux, G. Holloway, H. C. Bandulet, D. Brassard, J. C. Kieffer, M. A. El Khakani, and F. A. Hegmann, "Phase diagram of the ultrafast photoinduced insulator-metal transition in vanadium dioxide," *Physical Review B* **85**, 155120 (2012).
 113. S. Lysenko, V. Vikhnin, A. Rúa, F. Fernández, and H. Liu, "Critical behavior and size effects in light-induced transition of nanostructured VO₂ films," *Physical Review B* **82**, 205425 (2010).
 114. B. Lazarovits, K. Kim, K. Haule, and G. Kotliar, "Effects of strain on the electronic structure of VO₂," *Physical Review B* **81**, 115117 (2010).
 115. N. Émond, A. Ibrahim, B. Torriss, A. Hendaoui, I. Al-Naib, T. Ozaki, and M. Chaker, "Impact of tungsten doping on the dynamics of the photo-induced insulator-metal phase transition in VO₂ thin film investigated by optical pump-probe spectroscopy," *Applied Physics Letters* **111**, 092105 (2017).
 116. H. Kizuka, T. Yagi, J. Jia, Y. Yamashita, S. Nakamura, N. Taketoshi, and Y. Shigesato, "Temperature dependence of thermal conductivity of VO₂ thin films across metal-insulator transition," *Japanese Journal of Applied Physics* **54**, 053201 (2015).
 117. A. Shah, A. Mahmood, U. Aziz, R. Rashid, Q. Raza, and Z. Ali, "Influence of Nb content on the structural and optical properties of anatase TiO₂ polycrystalline

- thin film by e-beam technique," *Materials Chemistry and Physics* **180**, 383-389 (2016).
118. M. Nakajima, N. Takubo, Z. Hiroi, Y. Ueda, and T. Suemoto, "Photoinduced metallic state in VO₂ proved by the terahertz pump-probe spectroscopy," *Applied Physics Letters* **92**, 011907 (2008).
 119. M. Hada, K. Okimura, and J. Matsuo, "Photo-induced lattice softening of excited-state VO₂," *Applied Physics Letters* **99**, 051903 (2011).
 120. A. Pashkin, C. Kübler, H. Ehrke, R. Lopez, A. Halabica, R. F. Haglund, R. Huber, and A. Leitenstorfer, "Ultrafast insulator-metal phase transition in VO₂ studied by multiterahertz spectroscopy," *Physical Review B* **83**, 195120 (2011).
 121. V. R. Morrison, R. P. Chatelain, K. L. Tiwari, A. Hendaoui, A. Bruhács, M. Chaker, and B. J. Siwick, "A photoinduced metal-like phase of monoclinic VO₂ revealed by ultrafast electron diffraction," *Science* **346**, 445-448 (2014).
 122. S. Wall, L. Foglia, D. Wegkamp, K. Appavoo, J. Nag, R. F. Haglund, J. Stähler, and M. Wolf, "Tracking the evolution of electronic and structural properties of VO₂ during the ultrafast photoinduced insulator-metal transition," *Physical Review B* **87**, 115126 (2013).
 123. H. Photonics, *Photomultiplier Tubes Basics and Applications* 4th ed. (Hamamatsu Photonics 2017).
 124. M. Razeghi and A. Rogalski, "Semiconductor ultraviolet detectors," *Journal of Applied Physics* **79**, 7433-7473 (1996).
 125. E. Monroy, F. Omnis, and F. Calle, "Wide-bandgap semiconductor ultraviolet photodetectors," *Semiconductor Science and Technology* **18**, R33-R51 (2003).
 126. L. Sang, M. Liao, and M. Sumiya, "A comprehensive review of semiconductor ultraviolet photodetectors: from thin film to one-dimensional nanostructures," *Sensors (Basel)* **13**, 10482-10518 (2013).
 127. H. Chen, K. Liu, L. Hu, A. A. Al-Ghamdi, and X. Fang, "New concept ultraviolet photodetectors," *Materials Today* **18**, 493-502 (2015).
 128. Y. Muraoka, T. Yamauchi, Y. Ueda, and Z. Hiroi, "Efficient photocarrier injection in a transition metal oxide heterostructure," *Journal of Physics: Condensed Matter* **14**, 757-763 (2002).
 129. J. A. Creeden, S. E. Madaras, D. B. Beringer, I. Novikova, and R. A. Lukaszew, "Growth and Characterization of Vanadium Dioxide/Niobium Doped Titanium Dioxide Heterostructures for Ultraviolet Detection," *Advanced Optical Materials* **0**, 1901143 (2019).
 130. H. Marom and M. Eizenberg, "The effect of surface roughness on the resistivity increase in nanometric dimensions," *Journal of Applied Physics* **99**, 123705 (2006).
 131. R. J. King, "Ellipsometry," *Vacuum* **22**, 493-495 (1972).
 132. I. J.A Woollam Co., *Guide to Using WVASE Spectroscopic Ellipsometry Data Acquisition and Analysis Software* (J.A Woollam Co.,Inc., Lincoln NE, 2012).
 133. G. E. J. Jr. and F. A. Modine, "Parameterization of the optical functions of amorphous materials in the interband region," *Applied Physics Letters* **69**, 371-373 (1996).

134. V. D. Atef Z. Elsherbeni, *The Finite-Difference Time-Domain Method for Electromagnetics with Matlab Simulations* (SciTech Publishing Raleigh NC, 2009).
135. F. Abelès, "Recherches sur la propagation des ondes électromagnétiques sinusoidales dans les milieux stratifiés," *Ann. Phys.* **12**, 596-640 (1950).
136. P. Yeh, "Optics of anisotropic layered media: A new 4×4 matrix algebra," *Surface Science* **96**, 41-53 (1980).
137. M. Schubert, "Polarization-dependent optical parameters of arbitrarily anisotropic homogeneous layered systems," *Physical Review B* **53**, 4265-4274 (1996).